

University of Nebraska - Lincoln

DigitalCommons@University of Nebraska - Lincoln

Mechanical (and Materials) Engineering --
Dissertations, Theses, and Student Research

Mechanical & Materials Engineering, Department
of

5-2016

Mild Traumatic Brain Injury: Combined in Silico and in Vitro Studies

Yi Hua

University of Nebraska-Lincoln, huayixiaolu@gmail.com

Follow this and additional works at: <http://digitalcommons.unl.edu/mechengdiss>



Part of the [Biomechanical Engineering Commons](#)

Hua, Yi, "Mild Traumatic Brain Injury: Combined in Silico and in Vitro Studies" (2016). *Mechanical (and Materials) Engineering -- Dissertations, Theses, and Student Research*. 100.

<http://digitalcommons.unl.edu/mechengdiss/100>

This Article is brought to you for free and open access by the Mechanical & Materials Engineering, Department of at DigitalCommons@University of Nebraska - Lincoln. It has been accepted for inclusion in Mechanical (and Materials) Engineering -- Dissertations, Theses, and Student Research by an authorized administrator of DigitalCommons@University of Nebraska - Lincoln.

MILD TRAUMATIC BRAIN INJURY: COMBINED IN SILICO
AND IN VITRO STUDIES

by

Yi Hua

A DISSERTATION

Presented to the Faculty of
The Graduate College at the University of Nebraska
In Partial Fulfillment of Requirements
For the Degree of Doctor of Philosophy

Major: Mechanical Engineering & Applied Mechanics

Under the Supervision of Professor Linxia Gu

Lincoln, Nebraska

May, 2016

MILD TRAUMATIC BRAIN INJURY: COMBINED IN SILICO AND IN VITRO STUDIES

Yi Hua, Ph.D.

University of Nebraska, 2016

Adviser: Linxia Gu

Mild traumatic brain injury (TBI) is a significant public health concern worldwide and has attracted significant attention due to high-impact sport as well as improvised explosive devices used in military conflicts. The earliest sign of mild TBI is associated with cognitive, behavioral and physical/somatic changes, which are commonly invisible to existing medical techniques. Thus it is essential to target mechanisms of mild TBI and its associated damage measures for earlier diagnosis/treatment and enhanced protection strategies.

In this work, the mechanism of blast-induced mild TBI was inspected through integrated in silico and in vitro models. A three-dimensional (3D) human head model with anatomical details was reconstructed from high-resolution medical images, and positioned in three different directions with respect to the blast wave. The effects of head orientations as well as cerebral blood vessel network in brain mechanics were investigated. The dynamic responses of the brain were monitored by the maximum principal strain (MPS), shear strain (SS), and intracranial pressure (ICP). The developed numerical model was validated by the shock tube experiment using a surrogate head, i.e., water-filled polycarbonate shell. Results demonstrated that the ICP alternations in the brain was initially dominated by the direct blast wave propagation and the skull flexure took effect at a later time. It is worth noting that cerebral blood vessel network induced larger MPS and SS in the brain, which were influenced by vessel diameter and density. Moreover, the

contour of the head and its orientation significantly altered the flow dynamics around the head, resulting in different spatial and temporal distributions of brain mechanics. Excessive mechanical strain sensed by brain cells, especially abundant cortical astrocytes, could be a potential index factor for the brain injury.

An in vitro injury model for primary cortical astrocytes was developed to identify the injury threshold. Rat cortical astrocytes cultured on silicone membrane were subjected to equibiaxial pulse stretch. The blast pressure profile on the membrane was monitored and the membrane deformations were captured through the high-speed imaging system. The simulated membrane strain, validated by experimental measures, was used to construct an exposure-response curve. It was observed that live cells declined sharply in the strain range from 18% to 35%, which was identified as the injury threshold of cortical astrocytes.

The obtained damage threshold of rat cortical astrocytes could be inferred about the level of brain injury in a rat. A 3D rat head model was constructed with an impactor mimicking the loading conditions of contact sports. Results revealed that impact depth and impactor shape were the two leading factors affecting brain dynamics. The influence of impactor diameter was region-specific and an increase in impactor diameter could substantially increase brain strains in the region which located directly beneath the impactor. The lateral impact could induce higher strains in the brain than the central impact. Results suggested that indentation depth instead of impact depth would be appropriate to characterize the influence of a softer impactor.

Acknowledgments

I am immensely grateful to my adviser, Dr. Linxia Gu, for her support and guidance over the years. If she had not believed in me, I never would have the opportunity to study overseas and conduct the research presented in this dissertation.

I would also like to express my gratitude to Dr. Jiashi Yang, Dr. Jinsong Huang, Dr. Kamlakar Rajurkar, and Dr. Xu Li for serving as my supervisory committee members and providing valuable feedback. I would like to express my appreciation to Dr. Ruqiang Feng who taught me various experimental skills. I would also like to acknowledge Dr. Jian Wang for his insightful suggestions in the group meetings.

I am also grateful to our collaborators from the University of Nebraska Medical Center – Dr. Matthew Kelso and his graduate student, Gang Zhao – for providing experimental datasets in rats using controlled cortical impact models. I also thank Dr. Srivatsan Kidambi and his graduate student, Christina Wilson, from the Department of Chemical and Biomolecular Engineering for conducting the *in vitro* cell damage tests. I would also like to express my gratitude to Dr. Ming Li and his postdoc, Dr. Ruiyong Wu, from the Department of Psychology for providing the biological tissues and the suggestions for tissue processing and tests. I also thank Dr. Carl Nelson and his graduate student, Jeff Berg, for conducting the surrogate head tests. Thanks also to Dr. Mehrdad Negahban and his graduate student, Wenlong Li, for setting up the high-speed camera to capture the membrane deformations.

I would also like to thank all the members in the Bio-Mechanics Laboratory for their help and friendship, particularly Dr. Shijia Zhao, Praveen Akula, Shengmao Lin, and Junfei Tong. I also thank all the staff in the Department of Mechanical and Materials Engineering,

Heidi Krier, Kathie Hiatt, Cherie Crist, and Mary Ramsier for their assistance throughout my graduate career. I also thank all the friends I made here in Lincoln, since they made my life in Lincoln exciting and enjoyable.

Finally, I would like to thank my grandfather and parents for their encouragement and support of my education for the past 24 years. They push me to excel in everything I do and to always do my best in all circumstances. I also thank my wife, Lu Xiao, who has spent the best time of her life with me. Her support has been truly invaluable over the past 11 years. Thanks also to my son, George, for bringing so much joy and love into my life. You let me know that being a father is a great privilege and responsibility!

Contents

1. Introduction	1
1.1 Blast-induced traumatic brain injury (TBI).....	1
1.2 Brain injury mechanisms.....	2
1.3 In silico models of blast-induced TBI.....	3
1.4 In vitro cellular models.....	6
1.5 Specific aims.....	8
1.6 Overview.....	9
 2. Experimental & Numerical Investigation of the Mechanism of Blast Wave	
Transmission through a Surrogate Head	11
2.1 Introduction.....	11
2.2 Material and methods.....	12
2.2.1 Shock tube experiments.....	12
2.2.2 Finite element modeling.....	15
2.3 Comparison between shock tube tests and finite element results.....	17
2.4 Results.....	20
2.4.1 Interaction between blast wave and surrogate head.....	20
2.4.2 Structural response of the skull simulant.....	21
2.4.3 Pressure distributions in the brain simulant.....	23
2.5 Discussion.....	25

3. Relevance of Blood Vessel Networks in Blast-Induced Traumatic	
Brain Injury	31
3.1 Introduction.....	31
3.2 Materials and methods.....	33
3.2.1 Shock tube experiments.....	33
3.2.2 Finite element modeling.....	34
3.3 Results.....	40
3.3.1 Blast-induced pressure surge in the water.....	40
3.3.2 Effect of latex tube on the strain distribution in the gel.....	42
3.3.3 Effect of blood vessel networks.....	45
3.4 Discussion.....	49
3.5 Conclusions.....	52
4. Head Orientations Influence Brain Dynamics Subjected to Blast Loadings	53
4.1 Introduction.....	53
4.2 Finite element modeling.....	54
4.3 Results.....	58
4.4 Discussion.....	62
5. An In Vitro Injury Model for Primary Cortical Astrocytes	65
5.1 Introduction.....	65
5.2 Material and methods.....	67
5.2.1 Astrocyte culture.....	67
5.2.2 Cell damage experiment setup.....	68
5.2.3 High-speed camera for capturing membrane dynamics.....	70

5.2.4	Finite element modeling.....	71
5.2.5	Cell injury.....	71
5.2.6	Cell injury quantification.....	72
5.2.7	Statistical analysis.....	73
5.3	Results and discussion.....	73
5.3.1	Cell damage device characterization.....	73
5.3.2	Membrane strain analysis.....	76
5.3.3	Cell response to increasing membrane strain.....	78
5.3.4	Injury profiles of astrocytes.....	80
5.4	Conclusions.....	84
6.	Characterization of Closed Head Impact Injury in Rat	85
6.1	Introduction.....	85
6.2	Materials and methods.....	86
6.2.1	Finite element modeling.....	86
6.2.2	Design of computational experiments.....	89
6.3	Results.....	90
6.3.1	Model verification.....	90
6.3.2	Sensitivity studies.....	92
6.4	Discussion.....	97
7.	Conclusions and Future Work	103
7.1	Conclusions.....	103
7.2	Future work.....	105
	Reference	107

List of Figures

Figure 2.1: A 28" (711 mm) square shock tube apparatus.	13
Figure 2.2: Locations of (a) pressure sensors in the water and (b) strain gauges on the surface of the polycarbonate shell.	14
Figure 2.3: Experimentally measured Friedlander-type incident pressure history.	15
Figure 2.4: FE model of surrogate head subjected to blast loading (cut view in transverse plane).	16
Figure 2.5: Experiment and numerical comparison of pressure histories in the brain simulant, <i>i.e.</i> , water, at locations: (a) P1, (b) P2, and (c) P3.	18
Figure 2.6: Experiment and numerical comparison of surface strains on the skull simulant, <i>i.e.</i> , the polycarbonate shell, at locations: (a) S1, (b) S2, (c) S3, (d) S4, and (e) S5.	20
Figure 2.7: Reflected pressure histories measured at five locations around the surrogate head.	21
Figure 2.8: Spatial and temporal vector plots of the displacement in the transverse plane of the skull simulant (deformation scale factor of 50).	23
Figure 2.9: Typical pressure contour inside the brain simulant at $t = 0.625$ ms.	24

Figure 2.10: Pressure histories along the centerline of the brain simulant (cut view in transverse plane).	24
Figure 2.11: Pressure distribution in the vicinity of the surrogate head: (a) flow separation at $t = 0.88$ ms, and (b) flow reattachment at $t = 1.05$ ms.	26
Figure 2.12: Blast overpressure, surface strain, and intracranial pressure at five marked locations (a) M1, (b) M2, (c) M3, (d) M4, and (e) M5.	29
Figure 3.1: A schematic view of the surrogate head with dimensions in mm.	33
Figure 3.2: Finite element model of the surrogate head subjected to the blast loading (cut view in the transverse plane).	35
Figure 3.3: Finite element model.	38
Figure 3.4: Comparison of incident pressure with pressure in the water. (a) Loading-1, peak magnitude of the incident pressure was 0.15 MPa; (b) Loading-2, peak magnitude of the incident pressure was 0.19 MPa.	41
Figure 3.5: Comparison of pressure-time history in the water between the simulation and the experiment.	42
Figure 3.6: Comparison of maximum principal strain (MPS) histories in the gel which located at the front and back area of the latex tube.	43
Figure 3.7: Comparison of maximum principal strain (MPS) histories in the gel which located at the equivalent front and back area of the latex tube.	43
Figure 3.8: Distribution of maximum principal strain around the latex tube. The central white region indicates the location which previously occupied by the latex tube.	45

Figure 3.9: Comparison of maximum principal strain histories in five regions of the brain surrogate.	46
Figure 3.10: Comparison of shear strain histories in five regions of the brain surrogate.	47
Figure 3.11: Snapshots of intracranial pressure distributions.	48
Figure 3.12: Comparison of peak maximum principal strain (MPS) and peak shear strain (SS) in the core region (Regions D and E) of the brain surrogate for different vasculature diameters.	50
Figure 3.13: Comparison of peak maximum principal strain (MPS) and peak shear strain (SS) in the core region (Regions D and E) of the brain surrogate for different vasculature densities.	51
Figure 4.1: Finite element model of the human head subjected to blast loading (midsagittal view).	56
Figure 4.2: Comparison of the reflected pressure histories at four locations around the head for (a) front-on, (b) back-on, and (c) side-on cases.	59
Figure 4.3: Snapshots of intracranial pressure distributions for front-on, back-on, and side-on cases.	60
Figure 4.4: (a) Four regions in the midsagittal plane where the peak maximum principal strain was measured, and (b) comparison of the peak MPS for front-on, back-on, and side-on cases.	61
Figure 5.1: (a) A schematic view of the cell damage device, (b) a representative pulse pressure measured by the pressure transducer at nominal pressure of 5 psi and nominal pressure of 10 ms.	69

Figure 5.2: A schematic view of the astrocyte injury process.	72
Figure 5.3: CAI device characterization. High-speed camera images were utilized to measure the peak membrane displacement, w , at various nominal pressure, p_n , and time, t_n . The green highlighted line shows comparison to the numerical simulation.	75
Figure 5.4: Three-dimensional response surface plot for Eq. (5.1) simulating the peak membrane displacement as a function of nominal setting (time and pressure).	75
Figure 5.5: Relationship between the peak membrane displacement and the pulse pressure in the chamber.	76
Figure 5.6: Relationship between the average membrane strain and the peak membrane displacement.	78
Figure 5.7: Cell injury was determined by Ethd-calcein staining and quantified with flow cytometry (FC). Representative FC results (a) show the distribution of dead (Q1), injured (Q2), and live (Q4) cells based on intensity of staining with Ethd-1 and calcein immediately after injury ($t = 0$) with increasing average membrane strain from 0-90% strain. The quantification of live, injured and dead are presented as a % of the population of total stained cells (b) $n = 3$, “*” $P < 0.001$ vs the naïve cells, “**” $P < 0.05$ vs naïve cells.	80
Figure 5.8: Injury profile of astrocytes with increasing average membrane strain. % of population of live (a) and injured cells (b) after membrane stretch of 0-90% strain.	82
Figure 6.1: Finite element discretization of the adult male Sprague-Dawley rat head. ..	87
Figure 6.2: Isometric view of the closed head impact model.	99

Figure 6.3: Verification of rat head model with reference. (a) Coronal view of rat head subjected to controlled cortical impact, (b) peak MPS comparisons at four different locations of the brain.	93
Figure 6.4: Pareto chart of region-specific biomechanical responses to external impact parameters. A: impact depth; B: impact velocity; C: impact position; D: impactor diameter; E: impactor material; F: impactor shape.	95
Figure 6.5: Contour plots of MPS on a coronal plane of the rat brain.	96
Figure 6.6: A coronal view of skull deformation for (a) flat and (b) convex impactor. ..	99
Figure 6.7: Relative displacement at five mark locations along brain/skull interface. ...	100

List of Tables

Table 2.1: Material properties of skull and polycarbonate, brain and water.	14
Table 2.2: EOS parameters for both water and air.	16
Table 3.1: A summarization of material properties used in the simulation.	36
Table 3.2: Material properties of the skull, brain, blood vessels, and air.	39
Table 4.1: Material properties used in the finite element simulation.	57
Table 5.1: Nominal settings (pressure and time) used in this study with corresponding peak membrane displacement and average membrane strain.	70
Table 6.1: Material properties of the rat head components.	88
Table 6.2: Assignment of six factors and their selected levels in the orthogonal array. .	90
Table 6.3: Predicted peak maximum principal strain (MPS) in the cerebrum, hippocampus, and cerebellum.	93
Table 6.4: Range analysis for the peak maximum principal strain (MPS) in the cerebrum, hippocampus, and cerebellum.	94

Chapter 1

Introduction

1.1 Blast-Induced Traumatic Brain Injury

Traumatic brain injury (TBI) caused by improvised explosive devices has been described as the “signature wound of the war on terror” [1]. In the past decade, conflicts in Iraq (operation Iraqi freedom (OIF)) and Afghanistan (operation enduring freedom (OEF)) as well as the increasing burden of the terrorism around the world resulted in an increased number of cases with blast-induced TBI. It is reported that 68% of the OEF/OIF soldiers at Walter Reed Army Medical Center who screened positive for TBI had been injured by a blast [2], and data collected from March to September 2004 from Navy-Marine Corps medical facilities in Iraq found that IEDs were responsible for 62% of combat-related TBIs [3]. Another study of 2,898 TBI hospitalizations of U.S. Army soldiers deployed to Iraq and Afghanistan from September 2001 to September 2007 found that 62.7% of the TBIs were caused by explosions [4].

Common symptoms of TBI include a variety of cognitive, behavioral, and physical/somatic changes. For example, cognitive changes include disturbances in attention, memory, language, or executive functioning, such as poor planning, organizing,

or sequencing, and/or impaired judgment and impulse control [5-7]. Behavioral changes include mood changes, depression, anxiety, impulsiveness, emotional outbursts, irritability, or inappropriate laughter [5, 8]. Physical or somatic changes include headaches, fatigue, sleep disturbances, dizziness, problems with motor skills, and sensitivity to light and noise [5, 8]. In addition, 12-51% of TBI patients develop psychiatric disorders, such as major depression, anxiety disorders, and psychosis [7, 9], and up to 50% of TBI patients suffer from impaired neuroendocrine function, particularly growth hormone deficiency [8]. For blast-induced TBI patients in particular, depending on the severity of injury, common symptoms include headache, blurring of vision, transient deafness, and psychoneuroses [10]. Blast-injured patients are also more likely than other TBI patients to report neurological disorders such as insomnia, impaired concentration, memory loss, and hypervigilance [10, 11].

Some symptoms of TBI can be treated by pharmaceuticals. For example, stimulants such as methylphenidate or dextroamphetamine are commonly used to treat problems with attention or information processing, selective serotonin-reuptake inhibitor antidepressants are sometimes prescribed for irritability or angry outbursts, and valproate is often prescribed for migraines and behavioral symptoms [5]. However, due to its heterogeneous nature, there is still no broad-based cure for TBI.

1.2 Brain Injury Mechanisms

The mechanism by which blasts result in brain damage remains in dispute. One proposed mechanism suggests that the blast wave could directly transmit through the cranial cavity as the stress wave, which travels around the sound speed with high amplitude and can injure brain tissues through spalling, implosion, and pressure differentials. An earlier study found

that, when rhesus monkeys were exposed to air blasts, a large fraction of the pressure was transmitted into the brain through the skull, while little was transmitted from the torso to the brain [12]. Studies of rats and rabbits exposed to air blasts also demonstrated that pressures could be transmitted directly to the brain with only slight change in amplitude [10].

Alternatively, it is suggested that the central nervous system could be injured by blasts through the cerebral vasculature via a thoracic mechanism. This is deduced by the fact that ballistic pressure waves, which are generated when a projectile enters a viscous medium, can cause remote injuries. For example, shooting pigs in the thigh can result in apnea, electroencephalogram suppression, microscopic neuronal damage, and elevated pressures within the brain [13]. However, a recent rat study observed no rise in blood pressure or fall in heart rate during the first 15-30 s following blast exposure, suggesting the absence of a vascular surge leading to brain injury [14].

Finally, it is suggested that skull flexure following blast exposure can lead to brain injury [15]. For example, one rat study found that exposure to shock waves could cause deflections in the skull, and thus the intracranial pressure gradients within the brain [16]. However, another rat study observed no inward flexure of the skull, or any type of injury or weakening of the bones or sutures, following exposure to blasts with overpressures ranging from 262 to 1372 kPa [14]. Further studies are needed to better understand the mechanisms of blast-induced TBI.

1.3 In Silico Models of Blast-Induced TBI

Due to ethical considerations, numerical simulations are critical to furthering our understanding of blast-induced TBI. For example, Moss et al. conducted blast simulations

in which the human head was represented as an ellipsoid; a viscoelastic brain was surrounded by a layer of cerebrospinal fluid (CSF) and a layer of linear elastic skull [15]. Using ALE3D, an arbitrary Lagrangian-Eulerian multi-physics code, the ellipsoidal head model was subjected to a 100 kPa blast wave and a skull flexure mechanism was then established. However, the results are unreliable due to the lack of anatomical structures in the head model as well as the use of basic constitutive material properties for the brain.

More realistic head models have been used in other studies. For example, Chafi et al. developed a head model consisting of brain, CSF, pia and dura mater, skull, and scalp [17]. The brain was simulated using a hyperelastic Mooney-Rivlin model combined with a linear viscoelastic model. The CSF was represented by linear elastic elements with a fluid option. The pia and dura mater, skull, and scalp were modeled as linear elastic materials. Using LS-DYNA, an explicit, non-linear finite element code, simulations were conducted with incident overpressures of 243.18, 618.08, and 881.53 kPa. For all three blast scenarios, peak pressures in the brain exceeded a proposed concussion threshold of 235 kPa at the coup site, and peak shear stresses exceeded a proposed injury threshold of 16.5 kPa at the coup and contrecoup sites. Thus, it was suggested that blasts with overpressures ranging from 243.18 to 881.53 kPa could lead to concussion and axonal injury at various locations within the brain.

Taylor et al. constructed a head model consisting of white matter, gray matter, CSF, and skull from high-resolution images of a cryogenically frozen human female from the Visible Human Project (VHP) [18]. The skull was represented by a compressible, linear elastic, perfectly plastic constitutive model with a damage model to capture the fracture. The white and gray matter were represented by an elastic compressible equation of state

model for the volumetric response and a three-term Maxwell viscoelastic model for the deviatoric response. The CSF was modeled using a nonlinear tabular equation of state. Using the shock physics wave code CTH, the head model was subjected to a 1.3 MPa blast from front, back, and side directions. For all blast orientations, it was found that the peak pressure in the brain occurred at the coup site, and the peak volumetric tension occurred at the contrecoup site. In addition, it was found that high shear stresses occurred in the temporal lobes and cortical area for the front and back blasts. For the side blast, elevated shear stresses were diffusely distributed in the right hemisphere and concentrated in focal areas in the left hemisphere. This study thus demonstrated that blasts could lead to the development of pressure, volumetric tension, and shear stress in focal areas of the brain and that stress patterns were dependent on the orientation of the blast wave and the complex geometry of the skull, brain, and tissue interfaces.

The Wayne State University Head Injury Model, a high-resolution finite element human head model that was extensively used in impact studies, has been used in blast simulations [19]. The head model consisted of scalp, skull with outer table, diploe, and inner table, dura, falx cerebri, tentorium, sagittal sinus, transverse sinus, bridging veins, CSF, arachnoid membrane, pia mater, hemispheres with distinct white and gray matter, cerebellum, brainstem, lateral ventricles, third ventricles, facial bones, nasal cartilage, teeth, temporal mandibular joint, ligaments, flesh and skin. Using LS-DYNA, the head model was subjected to front, side, and back blasts with overpressures of 0.21-0.61 MPa and durations of 1-4 ms. The blasts were found to result in peak brain pressures of 0.7-1.8 MPa in the cortex and peak brain strains of 2-11%.

Ganpule et al. compared surface pressure measurements from shock tube experiments involving a physical surrogate based on Hybrid III dummy head with simulations conducted using a 3D human head model developed using VHP data [20]. The head model consisted of skin, skull, and subarachnoid space, which were modeled as linear, elastic, isotropic materials, and brain, which was modeled using an elastic volumetric response and a viscoelastic shear response. Good agreement was found between the surface pressure profiles from experiments and simulations at five locations on the surface of the skull. From the simulations, it was found that the intracranial pressure profiles reflected a coup-counter coup pattern, with a compressive wave front propagating from the incident blast side and a tensile wave front propagating from the opposite side. Moreover, it was found that the peak pressure at the frontal location of the brain was caused by direct transmission of the blast wave into the brain; while at other locations, pressure profiles were governed by a combination of the stress wave in the skull, pressure wave in the brain, wave reflections from tissue interfaces, and the surface pressure wave. It was also found that the flow field around the head was governed by the geometry of the head.

1.4 In Vitro Cellular Models

In vitro injury models are developed with intent to understand the effects of blast loading conditions at the cellular level. The neuron is by far the most studied cell type in this area. A number of devices are available for studying neuronal response to biaxial stretch [21-23], uniaxial stretch [24, 25], and shear [26-28]. It is reported that calcium signaling initiated from the site of primary mechanical injury was predominantly mediated by electrophysiological changes in the N-methyl-d-aspartate receptor (NMDAR) [29]. However, the NMDAR is critical only for the induction of a stretch-induced delayed

depolarization that can often accompany stretch injury [30]; the maintenance of this modestly increasing depolarization occurring hours following injury is mainly mediated by the electrogenic sodium pump in the membrane. Acute and long-term changes in cytosolic calcium are not only related to NMDAR activation [29, 31, 32], but also influenced by other glutamate receptors [33]. It should be noted that changes in the NMDAR after stretch are not universally observed across different laboratories [34]. Changes in neuronal NMDARs are also sensitive to the presence of glia in the culture [35, 36].

Although astrocytes are ubiquitous cells throughout brain tissues and make essential contributions to many homeostatic functions [37], studies regarding the response of astrocytes to a controlled mechanical loading is limited. One of the earliest studies was of primary astrocytes on both the single-cell and cell-monolayer level. For the single cell, injury was provoked by the mechanical poking of an astrocyte with the blunt end of a glass pipette tip [38]. This process can initiate a series of intercellular calcium waves that radiate from the simulated cell; however, the exact level of mechanical stimulus used to create these waves was not well quantified. Instead, the use of astrocytic monolayer allowed for a correlation between levels of mechanical deformation and cellular injury [39]. The cells on the monolayer showed cytoskeletal alterations, organelle disruption and derangement, and apparent changes in intracellular calcium ion influx. These ultrastructural changes increased in severity as the level of mechanical deformation increased. At one point, significant cell death could be produced within 24 h of the initial mechanical insult.

In a series of follow-up studies, the role of calcium in astrocytic injury [40] as well as the mechanisms responsible for calcium elevation [33, 41] were identified. Lamb et al. studied the role of membrane repair over time in injured astrocytes [42]. Ahmed et al.

studied mitochondria and ATP regulation [43]. Other researchers examined how the complex cascades regulating free radical generation and IP_3 signaling contributed to the stretch injury response in astrocytes over time [44, 45]. Recent work shows that release of proteins due to the mechanical stress can further exacerbate the initial injury [46].

1.5 Specific Aims

The goal of this work is to further our understanding of blast-induced TBI through *in silico* and *in vitro* modeling. Numerical models provide a practical means of investigating the mechanical effects of blast waves on the human head, given that blast injury experiments cannot be conducted on humans. As a complement to simulation, *in vitro* models using surrogates or cell culture system provide evidences on brain jury pathways as well as validation of the *in silico* models. Fulfillment of the goal of this work is based on the completion of four specific aims:

- Develop an experiment-validated numerical model to elucidate the wave transmission mechanisms through a surrogate head under blast loading.
- Investigate the influence of blood vessel networks on the dynamic responses of the brain under blast loading.
- Characterize the role of head orientation in the mechanics of blast wave-head interactions as well as the load transmitting to the brain.
- Develop an *in vitro* injury model for primary cortical astrocytes and apply a wide range of strain to determine the effect of these cell-stretching in TBI.
- Conduct numerical closed head impact experiments to investigate the sensitivities of intracranial responses to various impact parameters (e.g., impact depth, velocity,

and position; impactor diameter, material, and shape).

1.6 Overview

In Chapter 2, the dynamic response of a surrogate head, *i.e.*, water-filled polycarbonate shell is investigated using integrated shock tube experiments and numerical simulations. Repeated shock tube experiments were conducted on the surrogate head. The surface strain on the skull simulant and pressure inside the brain simulant at multiple locations are measured to validate the numerical model. The validated model is then used to further inspect the mechanisms of blast wave-surrogate head interactions in terms of flow field around the head, structural response of the skull simulant, and pressure distributions inside the brain simulant.

After elucidating the blast wave transmission mechanisms, the influence of blood vessel networks on the dynamic response of the brain is investigated in Chapter 3. A similar surrogate head model is developed and the Voronoi tessellations are implemented to represent the network of blood vessels embedded in the brain. Three commonly used injury measures, *i.e.*, maximum principal strain, shear strain, and intracranial pressure, are monitored at different regions of the brain to quantify the role of blood vessel networks in brain dynamics.

To capture the geometric nonlinearity of the realistic head contour, a three-dimensional human head model with anatomical details is generated from high-resolution medical imaging data, Chapter 4. The head is positioned in three different orientations with respect to the oncoming wave direction; head facing blast, head facing away from blast, and right side exposed to blast. The intensity of blast overpressures that exert at the vicinity of the

head is monitored. The brain responses in terms of intracranial pressure and maximum principal strain are also computed.

In Chapter 5, an *in vitro* injury model for primary cortical astrocytes is developed to understand the effect of blast loading at the cellular level. A modified version of the cultured axonal injury device is used to apply biaxial stretch to the silicone membrane with cultured astrocytes. Numerical simulation is used to calculate the strain on the membrane which the astrocytes sensed. By comparing the Live/Dead assay via flow cytometry, a high throughput spectroscopic analysis is introduced to evaluate the viability of astrocytes subjected to different levels of strain. The stretch-injury tolerance levels for the astrocytes with an aid of dose-response model are then established.

In Chapter 6, the sensitivities of intracranial responses to various impact parameters in the CHI model were systematically investigated. A 3D finite element rat head model with anatomical details was developed from medical images. An orthogonal experimental design was implemented for carrying out eight computational experiments to correlate the regional brain mechanics with impact controls including impact depth, velocity, and position, as well as impactor diameter, material, and shape.

Finally, the findings of this study are summarized and future work is proposed in Chapter 7.

Chapter 2

Experimental & Numerical Investigation of the Mechanism of Blast Wave Transmission through a Surrogate Head

2.1 Introduction

Blast-induced traumatic brain injury (TBI) has been identified as a “signature wound” of modern conflicts such as those in Iraq and Afghanistan [11, 47]. A recent report from the Armed Forces Health Surveillance Center (AFHSC) stated that, from 2000 to the fourth quarter of 2011, there have been 233,425 clinically confirmed TBI cases among U.S. service members [48]. Experimental studies using head surrogates, animal models, and post-mortem human specimens combined with computational methods, have been used to understand the mechanisms of blast-induced TBI and develop prevention strategies [16, 49-56]. Among these methods, head surrogates are intermediate and less expensive means to identify the detailed blast wave-head interactions as well as the impact of wave transmissions on brain mechanics. Alley et al. [54] conducted blast experiments on a head

surrogate consisting of a spherical poly(methyl methacrylate) (PMMA) shell housing synthetic gelatins as brain simulants. Pressure amplification and significant relative displacement were observed at the anterior locations near PMMA/gelatin boundaries, which were attributed to impedance mismatches. Zhu et al. [56] conducted shock tube tests on an egg-shaped head surrogate filled with gels. Static pressures within the shock tube and the surrogate were recorded and a numerical model was developed to assess the effect of elastic modulus of the shell, bulk modulus of the gel, head orientation and internal sensor location. Although these studies have quantified the mechanical response of a head surrogate under blast loading in terms of pressure profiles [54, 56] and surface strain mapping [54], characterizations of the flow field around the head and mechanisms of load transfer from the blast wave to the brain simulant remain unclear.

In this work, the dynamic response of the water-filled polycarbonate shell under blast loading was investigated using integrated shock tube experiments and numerical simulations. The surface strain on the skull simulant and pressure inside the brain simulant at multiple locations were monitored to validate the numerical model. The validated model was then used to further inspect the mechanisms of blast wave-surrogate head interactions in terms of flow field around the head, structural response of the skull simulant, and pressure distributions inside the brain simulant.

2.2 Materials and Methods

2.2.1 Shock Tube Experiments

The shock tube experiments were carried out in a 28" square shock tube with a total length of 12,319 mm, as shown in Figure 2.1. The surrogate head in the test section of the tube

was fixed onto a custom-made aluminum clamp. Polycarbonate and water served as skull and brain simulants, respectively, due to their similar material properties listed in Table 2.1. Water-proof gaskets were used to prevent leakage of water, along with a rubber lining to mitigate hard mechanical coupling between the surrogate and the aluminum clamp. To minimize wave reflections from the shock tube bottom surface, the surrogate head was elevated 65 mm above the bottom of the shock tube. Pressure histories in the water were measured at three locations using Kulite pressure sensors (Kulite, Basingstoke, U.K.; model no. LE-080-250A) as marked in Figure 2.2 (a). Five Vishay SR-4 general-purpose strain gauges (grid resistance $350 \pm 0.3\% \Omega$; gauge factor $2.09 \pm 0.5\%$) were bonded per Vishay bulletin B-129-8 onto the surface of the polycarbonate shell and connected to a Wheatstone quarter bridge to measure the longitudinal and transverse strains, as illustrated in Figure 2.2 (b). The shock wave incident pressure (Figure 2.3) was generated by rupturing a stack of 6 plies of 0.025 mm thick Mylar membranes. The shape of the incident pressure history was of the Friedlander type, with peak overpressure of 0.13 MPa and positive phase duration of 4.55 ms. Experiments were repeated five times ($N = 5$) to ensure the reliability of the measured results.

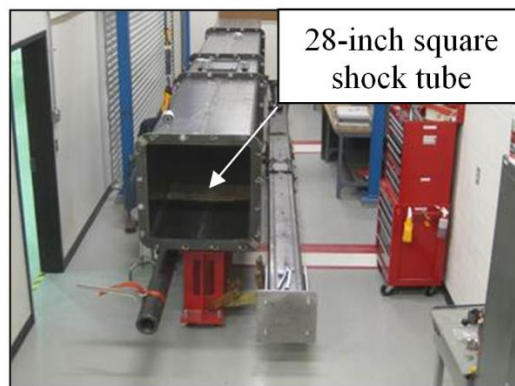


Figure 2.1: A 28" (711 mm) square shock tube apparatus.

Table 2.1: Material properties of skull and polycarbonate, brain and water [18, 57].

Material	Density ρ (kg/m ³)	Young's modulus E (MPa)	Bulk modulus K (MPa)	Acoustic impedance Z (MPa·s/m)
Skull	1710	5370	4820	2.1 – 7.8
Polycarbonate	1201	2344	6297	2.7
Brain	1040	0.123	2370	1.58
Water	996	/	2090	1.48 – 1.54

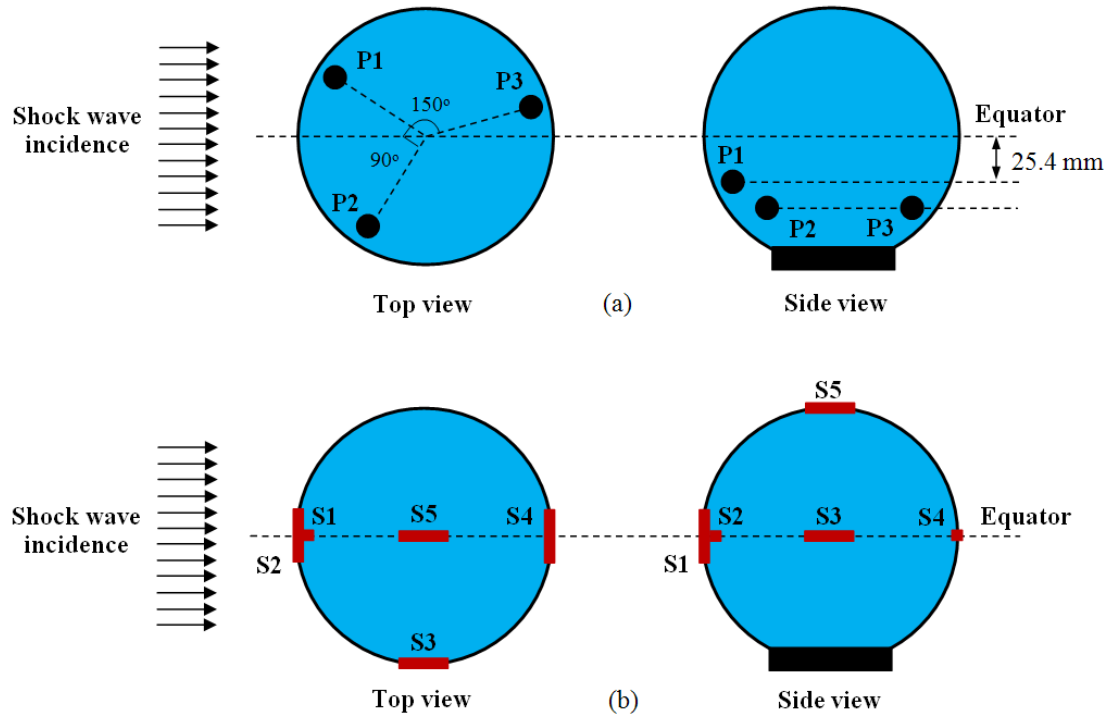


Figure 2.2: Locations of (a) pressure sensors in the water and (b) strain gauges on the surface of the polycarbonate shell.

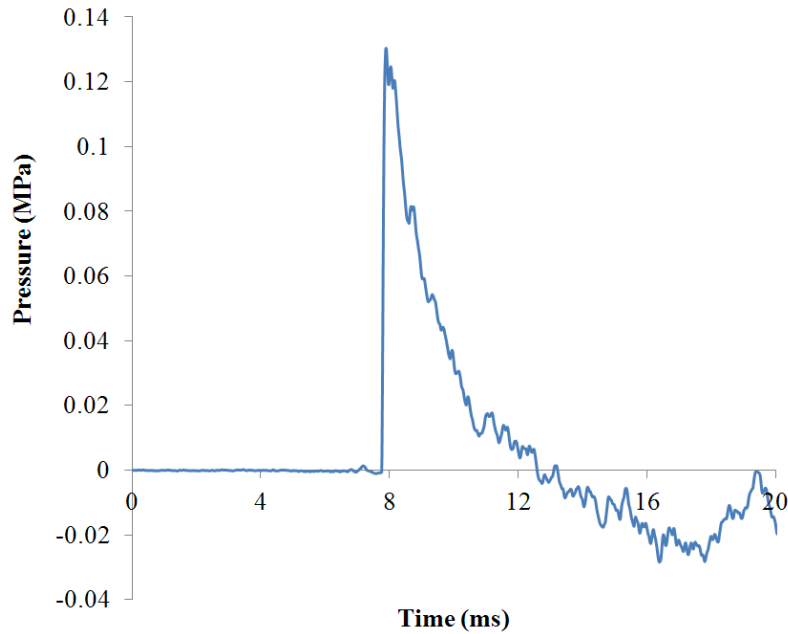


Figure 2.3: Experimentally measured Friedlander-type incident pressure history.

2.2.2 Finite Element Modeling

A 3D model of the surrogate head subjected to blast loading generated inside a shock tube was developed using ABAQUS software (Dassault Systems Simulia Corp., RI, USA), as shown in Figure 2.4. The listed homogeneous linear elastic isotropic material properties in Table 2.1 with a Poisson's ratio of 0.37 were used for the polycarbonate shell with inner diameter of 152.4 mm and thickness of 1.27 mm. The brain simulant was modeled as an incompressible fluid with the Mie-Grüneisen equation of state (EOS), which related the shock velocity and fluid particle velocity to the pressure inside the water [58]. Air was modeled using an ideal gas EOS since the Mach number of the shock front calculated from our experiments was approximately 1.4, and the ratio of specific heats did not change drastically at this Mach number. The EOS parameters for both water and air were summarized in Table 2.2. The aluminum clamp, used to stage the head surrogate inside the

shock tube, was assumed as an isotropic material with Young's modulus $E = 60 \text{ GPa}$, Poisson's ratio $\nu = 0.3$, and density $\rho = 2,700 \text{ kg/m}^3$.

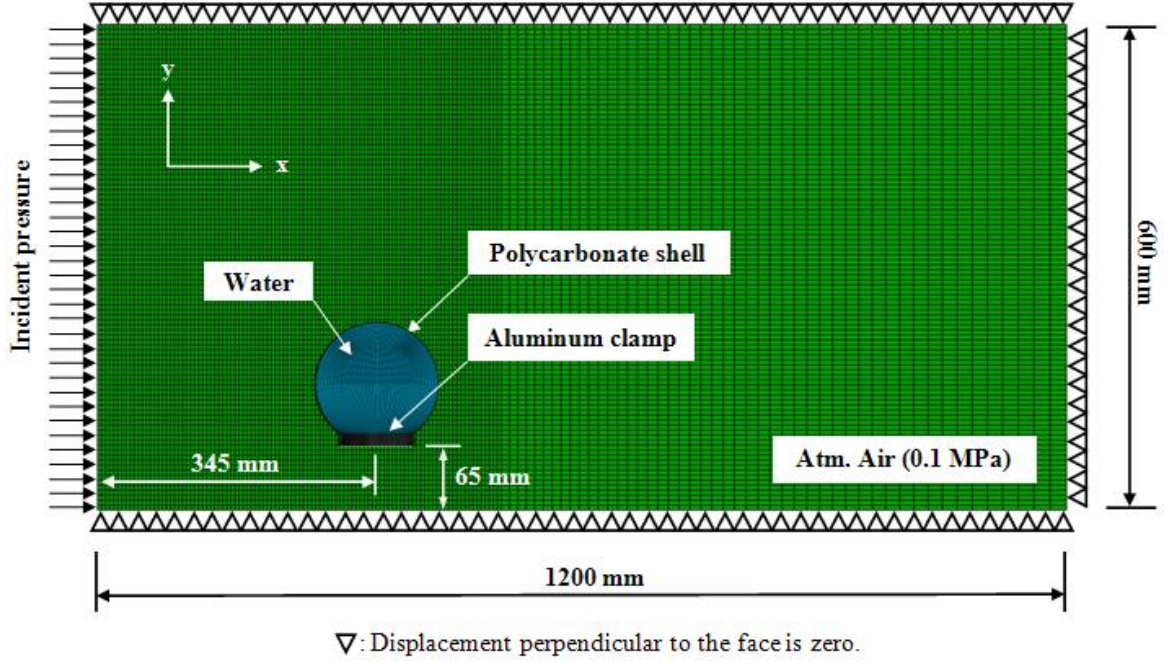


Figure 2.4: Finite element model of surrogate head subjected to blast loading (cut view in transverse plane).

Table 2.2: EOS parameters for both water and air [53, 58, 59].

Material	Parameter	Value
Water	Viscosity η (N.s/mm ²)	1×10^{-8}
	Sound speed c_0 (mm/s)	1.45×10^6
	Hugoniot slope coefficient s (/)	0
	Grüneisen's gamma Γ_0 (/)	0
Air	Density ρ (kg/m ³)	1.1607
	Gas constant R [J/(kg-K)]	287.05
	Temperature T (K)	300

The blast wave propagation and its interaction with the surrogate head is a fluid-structure interaction (FSI) problem. The air inside the shock tube was modeled with Eulerian elements and the surrogate head was modeled with Lagrangian elements. The Eulerian domain consisted of 1,378,176 brick elements with approximate mesh refinement near the region of the surrogate head to capture FSI effects. The Eulerian domain of air was chosen as $600\text{ mm} \times 600\text{ mm} \times 1200\text{ mm}$ such that the reflections from domain boundaries were negligible during the 4 ms simulation time. The polycarbonate shell, water and aluminum clamp were meshed with reduced 8-node hexahedral elements (C3D8R). A mesh convergence test was conducted, resulting in a chosen minimum mesh size of 2 mm.

The measured incident pressure history (Figure 2.3) was used as the pressure boundary condition at the inlet of the Eulerian domain. The velocity perpendicular to each face of the Eulerian domain was kept equal to zero to avoid escaping/leaking of air through these faces. This would create a pure 1D shock front traveling in the x-direction without lateral flow. The bottom face of the clamp was constrained in all six degrees of freedom. The interaction between an Eulerian domain and a Lagrangian one was enforced through a penalty contact algorithm with frictionless tangential sliding and hard contact normal behavior. A typical simulation required about 7 hours of CPU time, running on a Dell T3500 double quad-core Xeon W3550 processor for an integration time of 4 ms.

2.3 Comparison between Shock Tube Tests and Finite Element Results

The pressure histories in the brain simulant at locations P1, P2 and P3 labeled in Figure 2.2 (a) were compared between the experimental measurements and numerical results, as

shown in Figure 2.5. For easy comparison, the arrival time of the experimentally measured pressure profile was shifted to align with that of the numerical results. It was clear that the major features of the measured pressure profiles, including the peak overpressure, nonlinear decay, and small peaks and valleys were captured by the simulation. For example, considering the peak overpressure, the deviations between experiment and simulation were only 3.75%, 8.31% and 4.18% at locations P1, P2 and P3, respectively. The differences could be explained by the sensitivity of the pressure sensors. Moreover, significant low-frequency oscillation of the pressure magnitude was observed at the end of the decay period (from 2.5 ms to 4 ms) in both experiment and simulation, indicating that complicated wave interactions took place at these locations during this period.

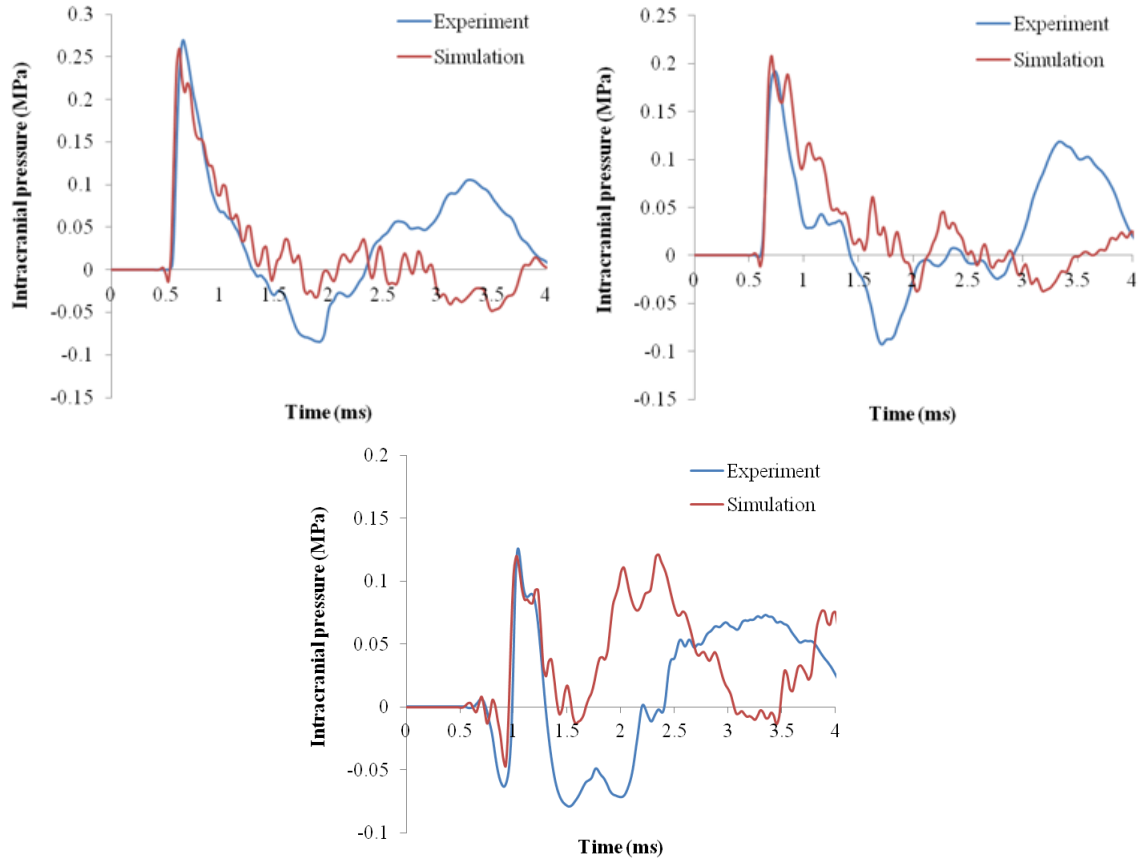
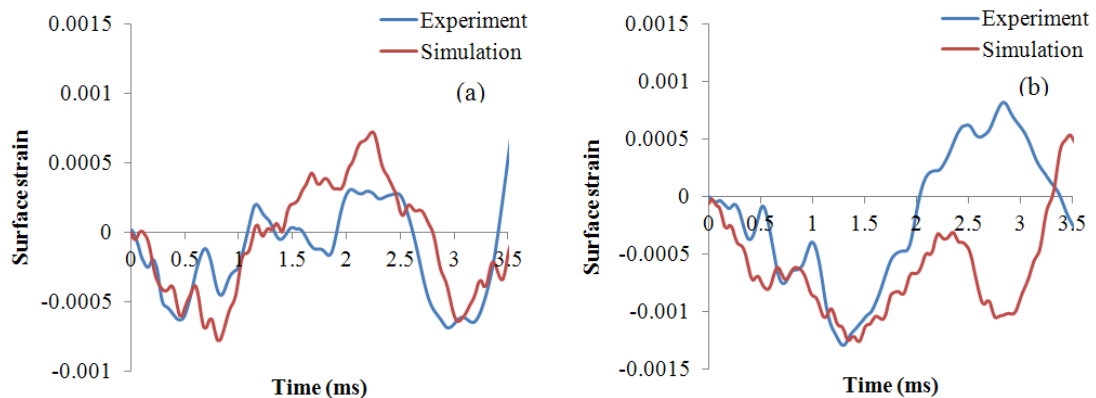


Figure 2.5: Experiment and numerical comparison of pressure histories in the brain simulant, *i.e.*, water, at locations: (a) P1, (b) P2, and (c) P3.

Strain history measurements have seldom been demonstrated in the existing literature. In this work, the surface strains on the skull simulant at five locations (S1, S2, S3, S4 and S5 marked in Figure 2.2 (b)) were compared between the experimental measurements and numerical simulation, as depicted in Figure 2.6. The surface strain histories measured at locations S1 – S4 from the simulation matched reasonably well with the experiment up to 2 ms; however, a faster decay and a quicker rise time were observed in the simulation after 2 ms. This deviation might be caused by neglecting the viscoelastic material properties of the skull simulant. The numerically obtained surface strain history at location S5 showed a relatively large discrepancy from the measured one. This could be attributed to the non-uniform thickness of the skull simulant as well as a possible air bubble accumulated at the top of the brain simulant. Considering the objective of this work, it is reasonable to state that the numerically obtained surface strains on the skull simulant and pressure histories in the brain simulant correlated well with the experimental measurements. The experiment-validated model can then be used to inspect various aspects of the mechanisms of blast wave-surrogate head interactions.



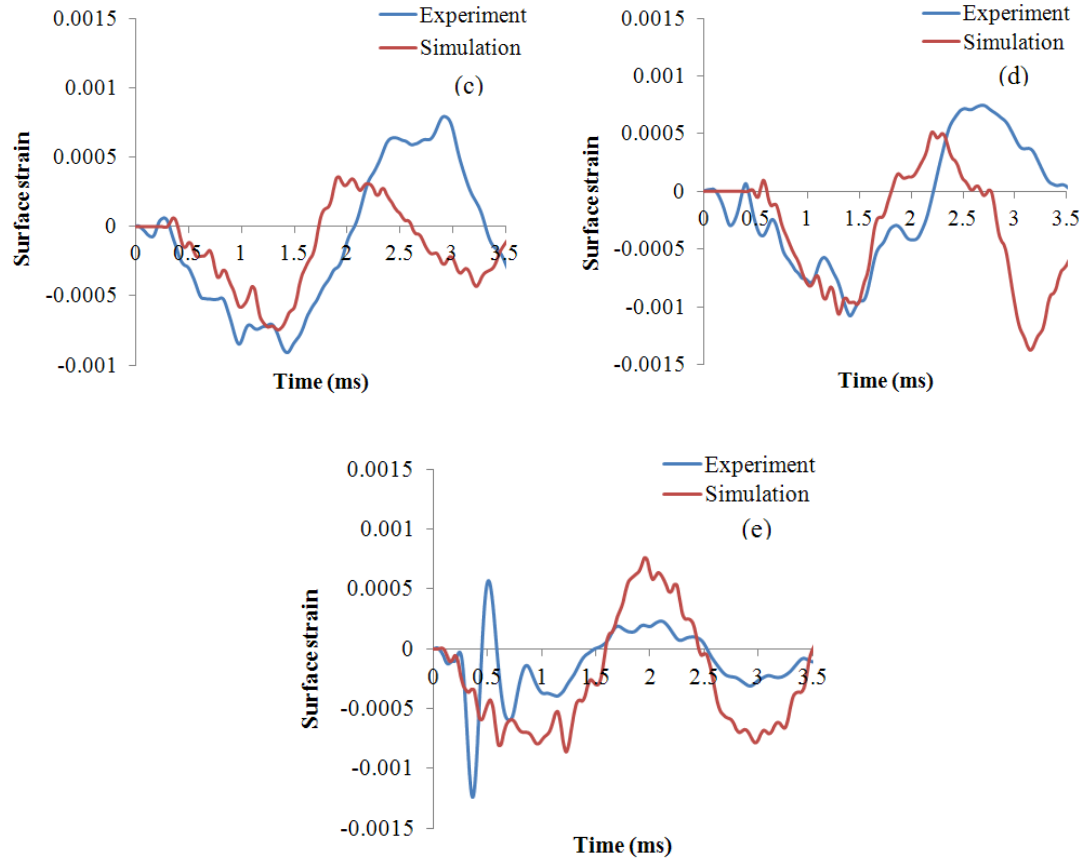


Figure 2.6: Experiment and numerical comparison of surface strains on the skull simulant, *i.e.*, the polycarbonate shell, at locations: (a) S1, (b) S2, (c) S3, (d) S4, (e) S5.

2.4 Results

2.4.1 Interaction between Blast Wave and Surrogate Head

The blast wave-surrogate head interactions can be studied by monitoring the reflected pressure histories at various locations around the head, as shown in Figure 2.7. Five locations from front to back of the head were identified and marked as R1 – R5. The incident pressure history has also been included for easy comparison. It was observed that the reflected peak overpressure at location R1 was 0.33 MPa. Compared to the incident

peak overpressure of 0.13 MPa, the reflection factor Λ , referred to as the ratio of reflected peak overpressure to incident peak overpressure, was calculated as 2.54. As the blast wave traversed the head, the reflected peak overpressure gradually decreased from locations R1 to R4 and even dropped below the incident peak overpressure at location R4 ($\Lambda = 0.30$). It should be noted that the reflected peak overpressure measured at location R5 was 0.19 MPa ($\Lambda = 1.46$), which was higher than that of 0.14 MPa ($\Lambda = 1.08$) at location R3 and 0.10 MPa ($\Lambda = 0.30$) at location R4.

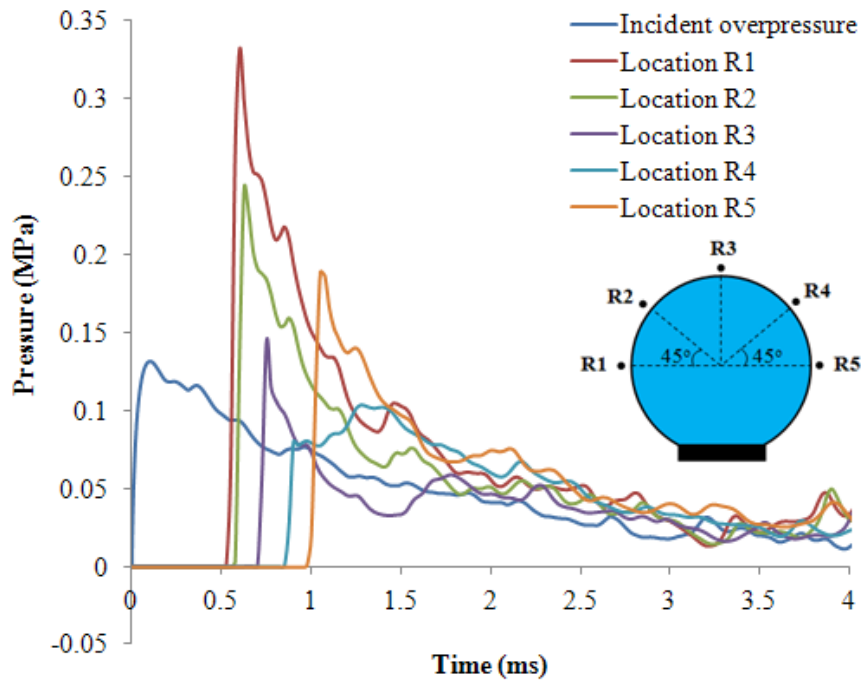
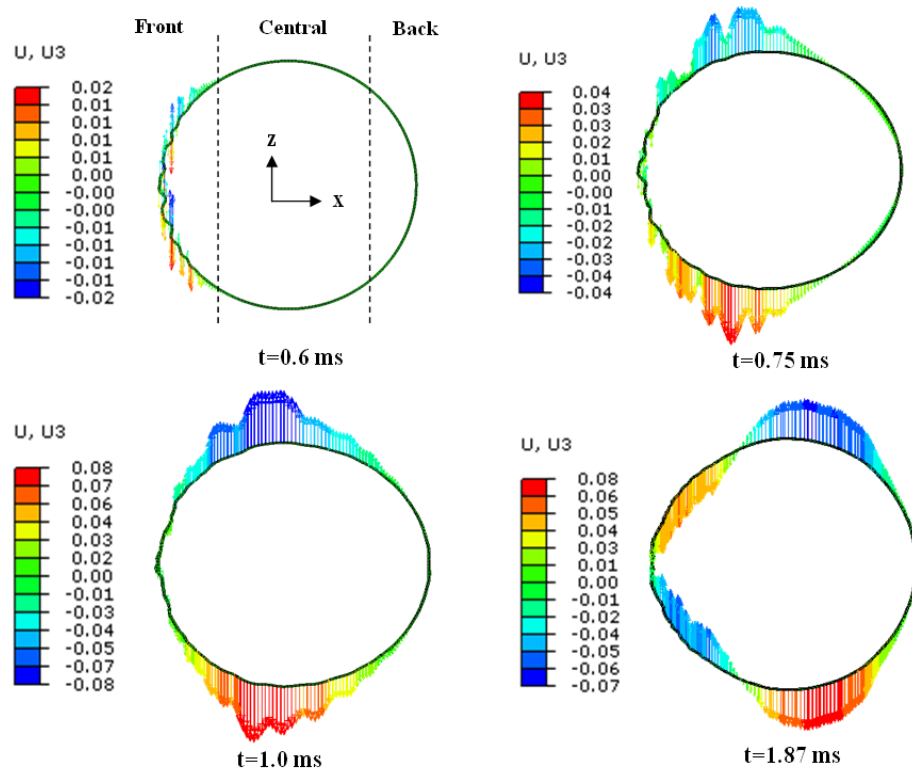


Figure 2.7: Reflected pressure histories measured at five different locations around the surrogate head.

2.4.2 Structural Response of the Skull Simulant

The structural response of the skull simulant subjected to blast loading was measured by monitoring the displacement in the transverse plane at various times, as shown in Figure 2.8. The motion of the skull simulant was considered inward or outward with respect to its

original spherical shape at $t = 0$ ms. At $t = 0.6$ ms, the wave front propagated through the ambient air and hit the front region of the skull simulant. The kinetic energy of the reflected pressure was then transmitted to the skull simulant and small localized skull flexure was observed in the front region. At $t = 0.75$ ms, the stress wave propagated into the central region of the skull simulant, causing the central region to move outward. At $t = 1.0$ ms, the localized skull flexure in the front region gradually disappeared and it started to move inward at $t = 1.87$ ms. As time progressed, the central region returned to the equilibrium position at $t = 2.0$ ms and then moved inward at $t = 2.25$ ms. At $t = 3.25$ ms, the central region moved outward again. Eventually, the entire skull simulant reestablished quasi-equilibrium at $t = 4.0$ ms.



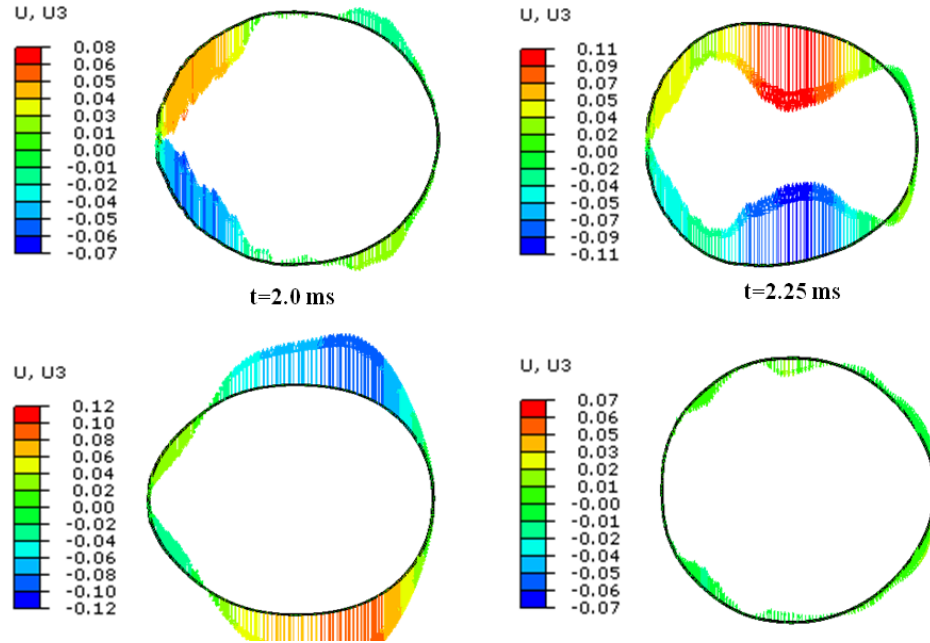


Figure 2.8: Spatial and temporal vector plots of the displacement in the transverse plane of the skull simulant (deformation scale factor of 50).

2.4.3 Pressure Distributions inside the Brain Simulant

A typical pressure contour inside the brain simulant is shown in Figure 2.9. A clear pressure gradient pattern was observed within the brain simulant, which was qualitatively consistent with the results observed in direct impact events [60]. The peak positive (compressive) pressure occurred at the anterior part (coup site) of the brain simulant and gradually decreased to a negative (tensile) pressure at the posterior part (countercoup site). Figure 2.10 shows the pressure histories along the centerline of the brain simulant with marked five locations. Pressure history profiles at locations B1 and B5 showed the typical coup-countercoup pattern. The highest peak pressure of 0.32 MPa was observed at location B1, which could be explained by the direct transmission of the blast wave into the brain simulant. The peak pressures decreased to 0.19 MPa, 0.12 MPa and 0.08 MPa at locations

B2, B3, and B4, respectively, whereas it increased to 0.13 MPa at location B5 at the posterior part of the brain. We also noticed a large negative pressure of -0.07 MPa occurring at location B5 around 1.0 ms.

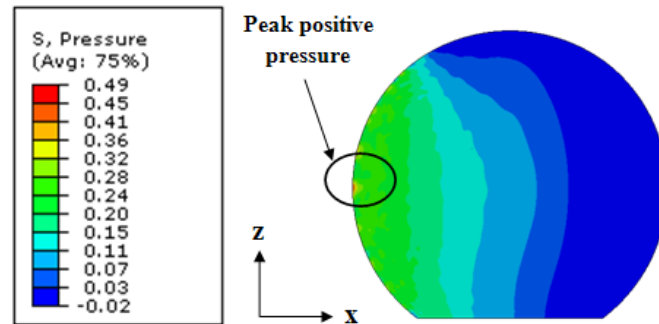


Figure 2.9: Typical pressure contour inside the brain simulant at $t = 0.625$ ms.

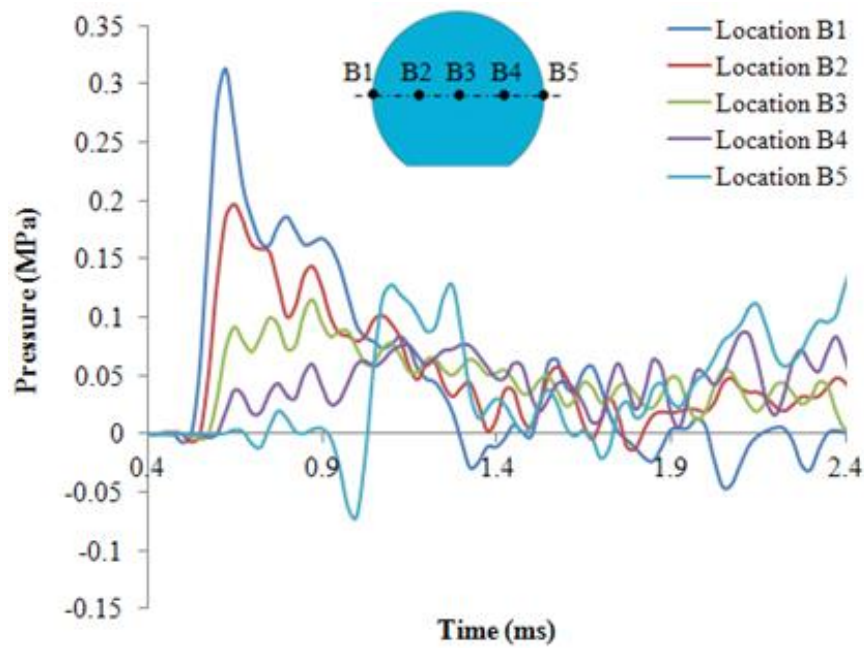


Figure 2.10: Pressure histories along the centerline of the brain simulant (cut view in transverse plane).

2.5 Discussion

Blast-induced TBI has stimulated intensive research in recent years to understand its mechanism for better prevention and treatment strategies. A few injury mechanisms have been proposed including direct cranial transmission [56, 61-64], thorax compression [65, 66], skull flexure [15, 16], rotational/translational acceleration [67-69] and brain cavitation [70, 71]. In this work, an experiment-validated numerical model was developed to elucidate the wave transmission mechanism of a head surrogate model (water-filled polycarbonate shell) subjected to blast loading. Repeated shock tube tests were conducted on the surrogate head. The surface strain on the skull simulant and pressure inside the brain simulant were recorded at multiple locations to validate the numerical model. The validated model was then used to inspect more details beyond the experimental measurements such as the flow field around the surrogate head, structural response of the skull simulant, and pressure distributions inside the brain simulant.

As the blast wave encountered the surrogate head, the incident wave pressure was amplified due to the fluid-structure interaction (Figure 2.7). This pressure amplification behavior could be attributed to the aerodynamic effects, in which the high-velocity particles of the shock front were brought to rest abruptly, leading to an amplified reflected pressure acting on the solid surface of the surrogate head. The initial reflection factor can vary from 2 to 8, depending on several factors such as the incident blast intensity, fluid medium in which blast wave travels, angle of incidence, mass and geometry of the object [59, 72]. Our results also indicated that the reflected pressure gradually decreased as the blast wave traversed the head ($\Lambda = 2.54, 1.84, 1.08, 0.30$ at locations R1, R2, R3 and R4, respectively) while it increased at the back side of the head ($\Lambda = 1.46$ at location R5). This was due to

the fluid dynamics around the surrogate head as demonstrated in Figure 2.11, which depicts the flow separation and reattachment in terms of pressure distribution in the vicinity of the surrogate head. It is clear that the reflected pressure at location R1 was substantially higher than the pressure surrounding the head at locations R2 and R3, which drove the flow of air from front to back. The head curvature caused the flow to detach from the head surface at location R3. The incident wave partially diverging away from the head surface contributed to the pressure relief near the surface between locations R3 and R4. The separated blast waves were then joined together behind the head, resulting in an instantaneous pressure increase on the back side of the head (location R5). Our numerical results elucidated the detailed fluid dynamics around the surrogate head, which could be then associated with the structural response of the skull simulant.

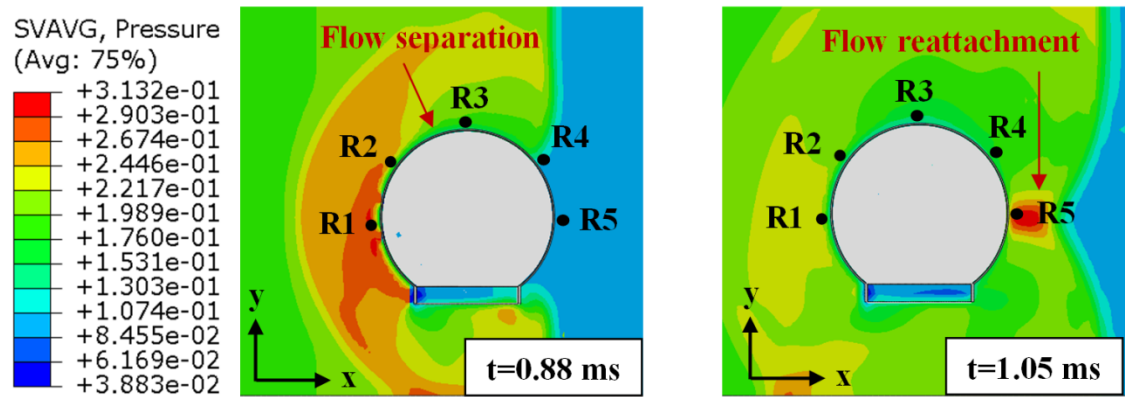


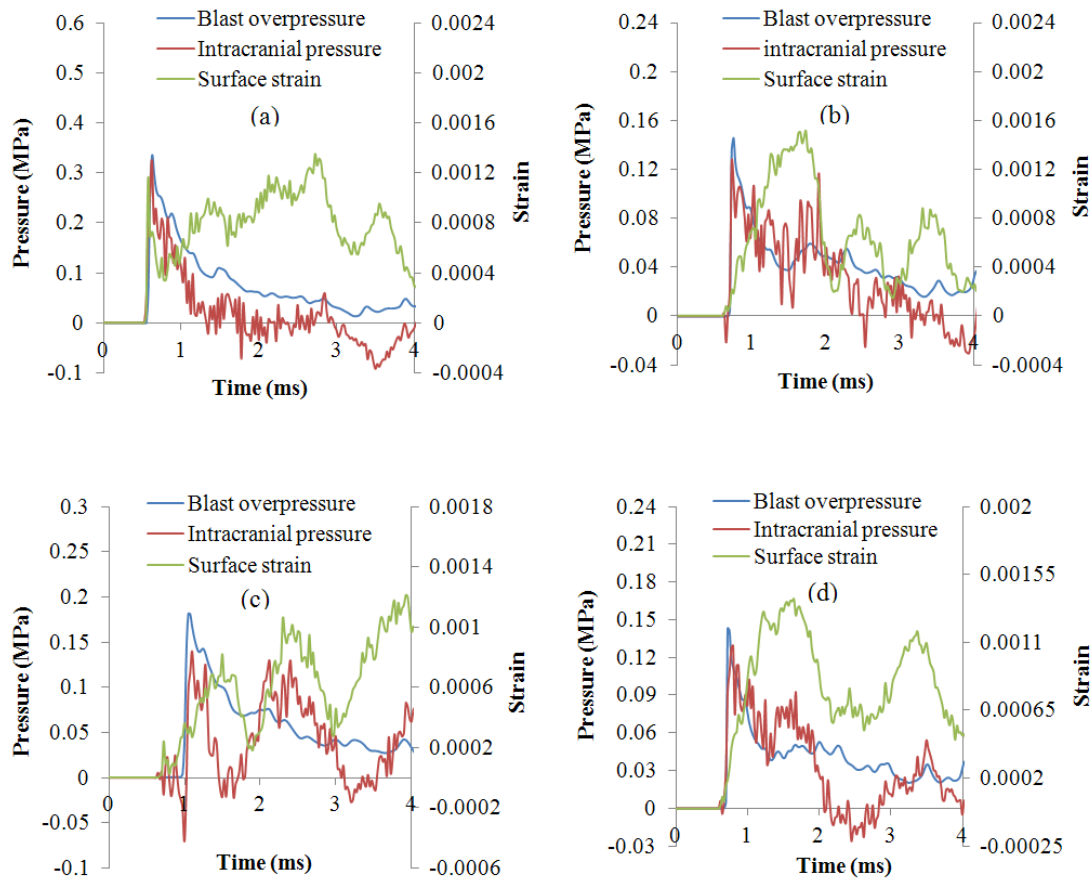
Figure 2.11: Pressure distribution in the vicinity of the surrogate head: (a) flow separation at $t = 0.88$ ms, and (b) flow reattachment at $t = 1.05$ ms.

Blast-induced shape changes of the skull simulant, referred to as skull flexure [15], were clearly illustrated in this work by the displacement vector plots in the transverse plane of the skull simulant (Figure 2.8). It clearly demonstrated that the skull simulant oscillated along its longitudinal axis (x-axis). Moss et al. [15] have pointed out that a non-lethal

pressure wave could generate flexural ripples in the skull, which could induce damaging intracranial pressure gradients within the brain [16].

To better understand the blast wave transmission mechanism, we have distinguished the stress waves imparted by the skull flexure from the direct blast wave transmission in terms of blast overpressure, surface strain of the skull simulant and intracranial pressure (Figure 2.12). Five marked locations (M1 – M5) along the skull to air and brain interfaces were used. The blast overpressure was obtained at the element of the air closest to the skull simulant, the surface strain was measured at the outermost element of the skull simulant, and the intracranial pressure was estimated at the element of the brain simulant closest to the skull simulant. Since the blast overpressure and intracranial pressure had a higher-order magnitude than the surface strain of the skull simulant, biaxial coordinates are used. At location M1, a sharp rise was observed in the intracranial pressure profile, which was in agreement with both profiles of the surface strain and blast overpressure. Following this sharp rise, the intracranial pressure profile closely followed the profile of the blast overpressure throughout the simulation time period (4 ms). Similarly at location M2, the intracranial pressure profile approximately followed the profile of the blast overpressure. Since the intracranial pressure profiles at locations M1 and M2 followed the profile of the blast overpressure rather than that of the surface strain, it can be inferred that the intracranial pressures in the anterior part of the head were dominated by the direct blast wave propagation, instead of the structural changes in the skull simulant. At locations M3, M4 and M5 of the posterior part of the head, the intracranial pressure profiles could be divided into two regimes. In the first regime (up to 1.2 ms), the intracranial pressure profiles followed the sharp rise and quick decay of the blast overpressure profiles. In the second

regime (after 1.2 ms), the intracranial pressure profiles changed to follow the oscillation of the surface strain profiles. These observations indicated that the intracranial pressure in the posterior part of the head was initiated by the direct blast wave propagation while the stress wave generated by the skull flexure would take effect at a later time. The knowledge of these detailed wave transmission physics at the skull to air and brain interfaces may facilitate developing effective strategies to reduce the occurrence of TBI.



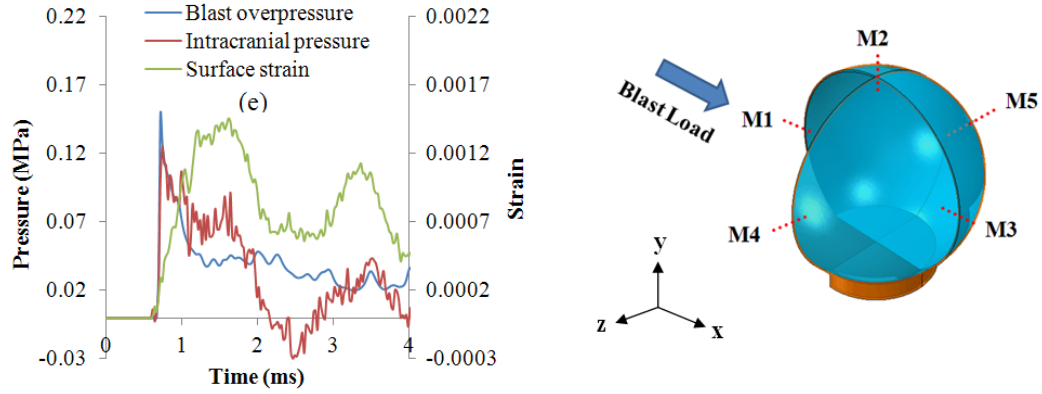


Figure 2.12: Blast overpressure, surface strain, and intracranial pressure at five marked locations (a) M1, (b) M2, (c) M3, (d) M4, and (e) M5.

Our results also showed a clear pressure gradient pattern within the brain simulant (Figure 2.9). The highest peak pressure occurred at the anterior location B1 (0.32 MPa), followed by that at location B2 (0.19 MPa), location B3 (0.12 MPa) and location B4 (0.08 MPa), while it increased at the posterior location B5 (0.13 MPa). This order was also observed by Zhu et al. [56]. Moreover, we also observed that a large negative pressure of -0.07 MPa occurred at the posterior location B5 around 1.0 ms, which was smaller than the reported cavitation pressure criterion of -0.1 MPa [73]. This indicated that no cavitation existed in our testing conditions. It should be mentioned though that the vulnerable cavitation area located at the posterior part of the head is consistent with the existing publications related to impact- or blast-induced brain injury [71, 74, 75].

It should be noted that the surrogate design in this study do not reflect all the attributes of the human head. The geometries and material properties of the head and brain were simplified. Although anatomically detailed human head models [76, 77] could provide better predictions of brain dynamics, these models have been rarely validated by experiments under blast scenarios. Even though human brain is 70 – 80% percent of water,

however, the neuronal cells, glial cells, axons, vessels, etc. all together made the brain tissue demonstrate viscoelastic, nonlinear, anisotropic properties, which need to be considered in the future head model for evaluating the injury threshold. More realistic models considering patient specific geometry and hyperplastic and viscoelastic properties of head will change the spatial and temporal pressure profiles within the brain. Despite these simplifications, the present work demonstrated the detailed physics of blast-head interaction. We have developed an experiment-validated numerical model to understand the wave transmission physics, including the flow field around the head, structural response of the skull simulant and pressure distributions inside the brain simulant. The computational tool validated in this work could be extended to more realistic geometry and material characterizations, which may have significant clinical implications for TBI by providing guidance for optimizing protective armors, and illuminating the possibilities for exploiting their potential to prevent TBI.

Chapter 3

Relevance of Blood Vessel Networks in Blast-Induced Traumatic Brain Injury

3.1 Introduction

Blast-induced traumatic brain injury (TBI) has been considered the signature injury of the wars in Iraq and Afghanistan [78]. It is estimated that more than 200,000 veterans returning from Iraq and Afghanistan have suffered TBIs, 69% as a result of blasts [11, 79]. Numerous studies looked into the brain injury mechanisms and remedies through *in vitro* experiments [80, 81] and modeling [82-84]. The brain is generally modeled as incompressible material without considering its integration with a complex network of blood vessels. As blood vessels are three to five orders of magnitude stiffer than the brain [85], its network is likely to impact the structural responses of the brain while the blast wave transmits into the brain. However, the role of vasculature in dynamic responses of the brain under blast loading has never been reported.

A few studies [86-88] did consider the role of vasculature in the brain responses under the impact loading (i.e., linear/rotational acceleration), however, their conclusions are contradictory. Zhang et al. developed a 2D human head finite element (FE) model with

several idealized branches of cerebral arteries, and observed that the inclusion of arteries in the brain led to a decrease in the peak maximum principal strain (MPS), shear strain (SS), and intracranial pressure (ICP) by 46%, 57%, and 42%, respectively [86]. It is speculated that the idealized artery branches are overestimated. On the contrary, Ho et al. [87] observed the minimal role of vasculature in the brain response with 2% alteration in peak MPS. Their study was based on a 3D human head FE model with image-based major branches of cerebral arteries. However, the networking between small branches of blood vessels was neglected. Along the same line, an experimental study by Parnaik et al. [88] reached the same conclusion. They constructed a 2D aluminum cylinder to represent the coronal section of the head, and used silicone gel as the brain. Isolated arteries made by silicone tubes were radially inserted into the brain. The artery-induced increases in peak SS and MPS were only 4% and 6%, respectively. We speculate that the networking of cerebral vasculature leads to the significant alternation of brain dynamics.

In this work, shock tube experiments were conducted to investigate the influence of single blood vessel on the dynamic responses of the brain under blast loading. The effect of blood vessel networks was then examined using the FE method. A spherical head and brain were developed within a shock tube. Voronoi tessellations were implemented to represent the network of blood vessels embedded in the brain. The blast wave-head interaction was simulated. Three commonly used injury measures, MPS, SS, and ICP, were monitored at different regions of the brain to quantify the role of blood vessel networks in brain dynamics.

3.2 Material and Methods

3.2.1 Shock Tube Experiments

The shock tube experiments were carried out in a 22.9 cm (9 in.) square shock tube with a total length of 6.1 m (20 ft). The surrogate head of rectangular shape (Figure 3.1) was positioned in the test section of the shock tube. A window was installed on the side of the tests section, which allowed visualization and measurement of the head response during a blast event via the high-speed camera. Polycarbonate and ballistic gel, i.e., prepared by mixing the gelatin powder and water in a 1:9 weight ratio and cured for 24 hours, were served as skull and brain simulants, respectively, due to their similar material properties [80, 89]. A latex tube filled with water was embedded into the gel to represent the blood vessel within the brain.

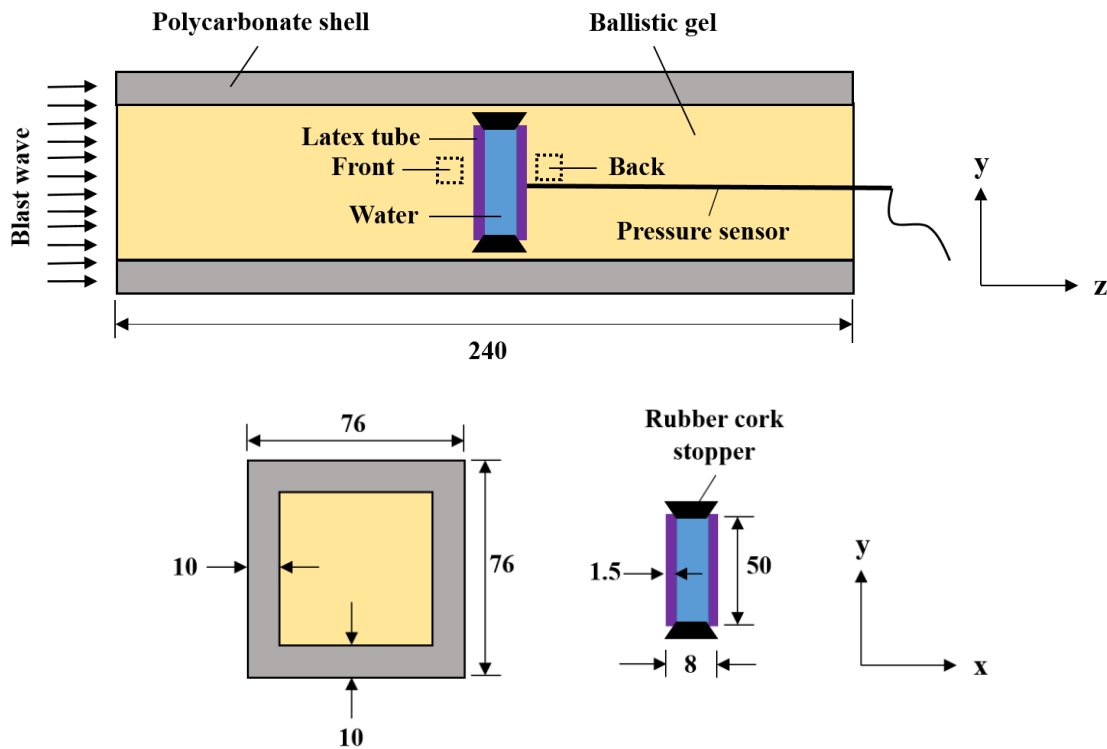


Figure 3.1: A schematic view of the surrogate head with dimensions in mm.

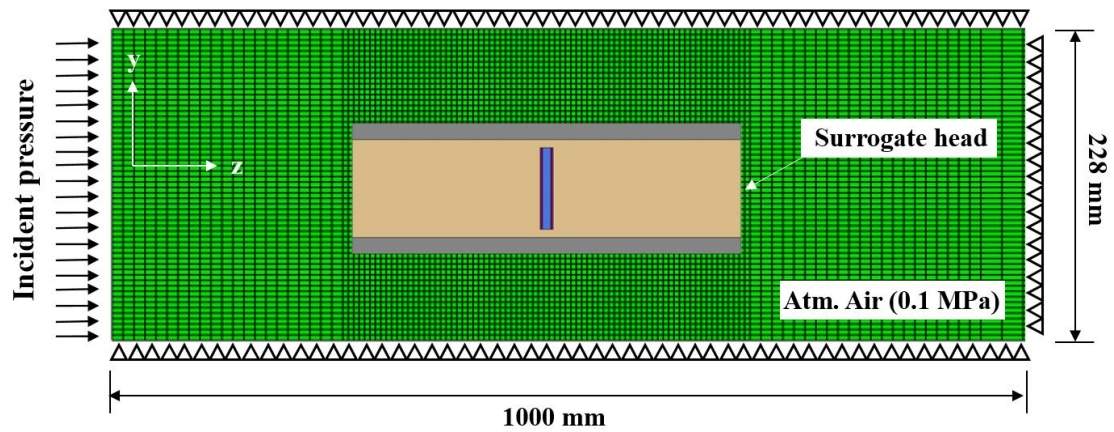
The pressure history in the water was measured using the Kulite pressure sensor (Kulite, Basingstoke, U.; model no. LE-080-250 A). The gel dynamics were monitored using a Photron FASTCAM SA1.1 high-speed camera (Photron USA Inc., San Diego, CA) equipped with a Nikon f/2.8 105mm macro lens. The deformation response of the gel subjected to the compressed air was captured with a resolution of 768×528 pixels at 14,400 frames per second. The maximum principal strain was then calculated using the ARAMIS system (GOM, Braunschweig, Germany).

The shock wave incident pressure was generated by rupturing a stack of 0.254-mm-thick Mylar membranes. The shape of the incident pressure history was of the Friedlander type. Two different blast intensities were implemented, with peak overpressures of 0.15 MPa and 0.19 MPa, respectively, which corresponding to the quantity of the membranes of 3 and 6. Experiments were repeated three times ($N = 3$) for each intensity to ensure the reliability of the measured results.

3.2.2 Finite Element Modeling

A 3D model of the surrogate head subjected to the blast loading generated inside the shock tube was developed using ABAQSU software (Dassault Systems Simulia Corp., RI), as shown in Figure 3.2. The polycarbonate shell was assumed as an isotropic linear elastic material with Young's modulus $E = 2,344$ MPa, Poisson's ratio $\nu = 0.37$, and density $\rho = 1,201$ kg/m³ [89]. The volumetric response of the ballistic gel was characterized as isotropic, linear elastic, and incompressible with $E = 1.314$ MPa, $\nu = 0.4999$, and $\rho = 1,040$ kg/m³ [90]. The latex tube was simulated as hyperelastic material with density $\rho = 966.12$ kg/m³ and hyperelastic parameters of $C10 = 0.32588$, $C20 = -0.04572$, $C30 = 0.01174$ [91]. Water was modeled as an incompressible fluid with the Mie-Grüneisen equation of state

(EOS), which related the shock velocity and fluid particle velocity to the pressure inside the water [92]. Air was modeled using an ideal gas EOS since the Mach number of the shock front calculated from our experiments was approximately 1.4, and the ratio of specific heats did not change drastically at this Mach number. A summarization of the material properties is described in Table 3.1.



∇ : Displacement perpendicular to the face is zero.

Figure 3.2: Finite element model of the surrogate head subjected to the blast loading (cut view in the transverse plane).

The blast wave propagation and its interaction with the surrogate head is a fluid-structure interaction (FSI) problem. The air inside the shock tube was modeled with Eulerian elements and the surrogate head was modeled with Lagrangian elements. The Eulerian domain consisted of 484,101 brick elements with approximate mesh refinement near the region of the surrogate head to capture FSI effects. The Eulerian domain of the air was chosen as $228 \text{ mm} \times 228 \text{ mm} \times 1,000 \text{ mm}$ such that the reflections from domain boundaries were negligible during the 3 ms simulation time. The polycarbonate shell,

ballistic gel, latex tube, and water were meshed with reduced eight-node hexahedral elements (C3D8R).

Table 3.1: A summarization of material properties used in the simulation.

(a) Elastic material properties				
Material	Density (kg/m ³)	Young’s modulus (MPa)	Poisson’s ratio (/)	
Polycarbonate	1,201	2,344	0.37	
Ballistic gel	1,040	1.314	0.4999	
(b) Hyperelastic material properties				
Material	C10 (MPa)	C20 (MPa)	C30 (MPa)	
Latex tube	0.32588	-0.04572	0.01174	
(c) Mie-Grüneisen equation of state (EOS) parameters				
Material	Viscosity (N·s/mm ²)	Sound speed (mm/s)	Hugoniot slope coefficient (/)	Grüneisen’s gamma (/)
Water	1 × 10 ⁻⁸	1.45 × 10 ⁶	0	0
(d) Ideal gas EOS parameters				
Material	Density (kg/m ³)	Gas constant (J/kg·K)	Temperature (K)	
Air	1.1607	287.05	300	

The measured incident pressure history was used as the pressure boundary condition at the inlet of the Eulerian domain. The velocity perpendicular to each face of the Eulerian domain was kept equal to zero to avoid escaping/leaking of the air through these faces.

This would create a pure 1D shock front traveling in the x-direction without lateral flow. The bottom of the polycarbonate shell was constrained in all six degrees of freedom. The constraint was used for the interactions between the latex tube and the ballistic gel as well as between the water and the latex tube. The interaction between an Eulerian domain and a Lagrangian one was enforced through a penalty contact algorithm with frictionless tangential sliding and hard contact normal behavior.

The spherical head with a brain diameter of 138 mm and skull thickness of 8 mm (Figure 3.3) was developed to delineate the impact of the blood vessel networks [93]. Within a radius of 48 mm away from the center of the brain, 30 tessellation nodes were randomly seeded using Delaunay triangulation (MATLAB, Mathworks Corporation). Then 161 Voronoi edges were generated to represent the vasculature network. Each blood vessel has a mean diameter of 2.72 mm, which is in the range of the reported diameter of human cerebral arteries, from 3.74 mm at the middle cerebral artery to 1.28 mm at the peripheral arteries [85]. The vasculature density, defined as the total length of the vasculature over the volume of the brain, was calculated as 0.0047 mm/mm^3 . This is comparable to the density quantification of 0.0037 mm/mm^3 from 3D computed tomography (CT) angiographies of the human brain [87]. We used a relatively larger density to take into account the small branches of the vasculature.

The skull was modeled as an homogeneous linear elastic isotropic material with the Young's modulus and Poisson's ratio of 5.37 GPa and 0.19, respectively [94]. The brain was assumed to be linear viscoelastic with a short-term shear modulus of 41 kPa and a long-term shear modulus of 7.8 kPa [90]. Young's modulus of 15 MPa and Poisson's ratio of 0.48 were adopted for the linear elastic blood vessels [86]. Air was modeled using an

ideal gas EOS since the Mach number of the blast front measured in our previous experiment [89] was approximately 1.4, and the ratio of specific heats did not change drastically at this Mach number. The material properties are summarized in Table 3.2.

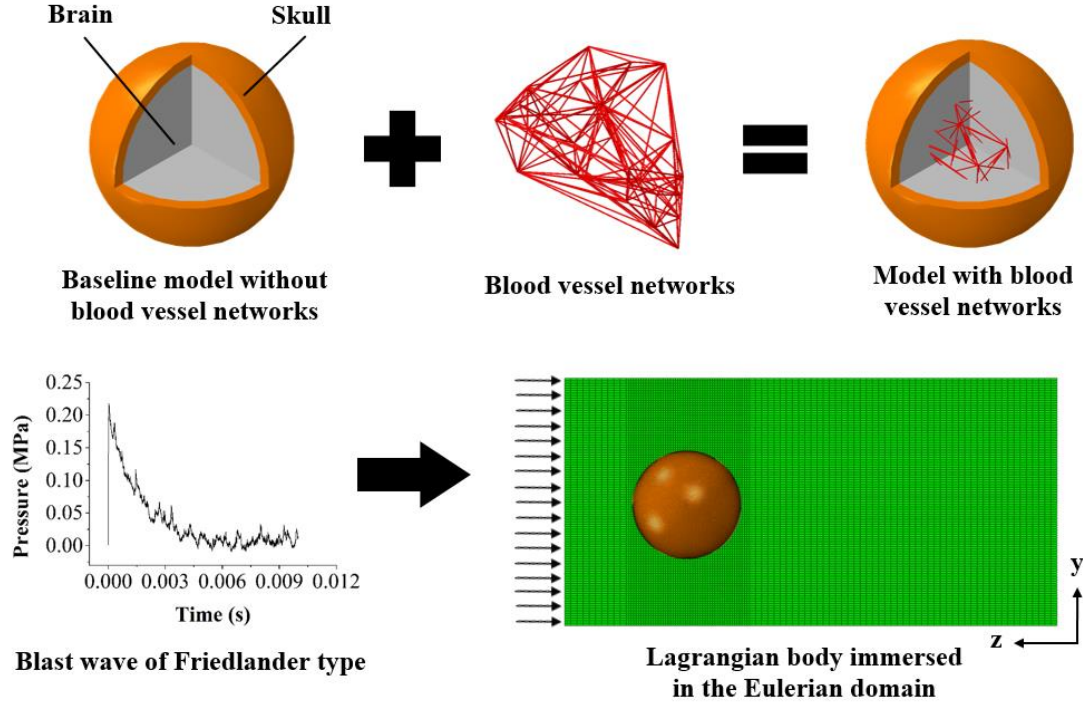


Figure 3.3: Finite element model.

The blast wave propagation and its interaction with the surrogate head is essentially a fluid-structure interaction (FSI) problem [59]. The air inside the shock tube was modeled with Eulerian elements, which could mimic the highly dynamic blast events. The surrogate head was modeled with Lagrangian elements. The coupling between an Eulerian domain and a Lagrangian one was enforced through a penalty contact algorithm with frictionless tangential sliding and hard contact normal behavior. The Eulerian domain consisted of 1,100,000 brick elements with approximate mesh refinement near the region of the surrogate head to capture the FSI effects. The Eulerian domain of air was chosen as $400 \times$

$400 \times 800 \text{ mm}^3$ such that the reflections from the main boundaries were negligible during the 2 ms simulation time. The skull and brain were meshed with reduced eight-node hexahedral elements (C3D8R). A mesh convergence study was conducted and the mesh size of 2 mm was chosen. The blood vessels were meshed with two-node beam elements (B31) that can sustain tensile and bending loads.

Table 3.2: Material properties of the skull, brain, blood vessels, and air.

(a) Elastic material properties:			
Material	Density (kg/m^3)	Young's modulus (MPa)	Poisson's ratio (/)
Skull	1,710	5,370	0.19
Brain	1,040	0.123	0.499989
Blood vessels	1,040	15	0.48
(b) Viscoelastic material properties:			
Material	Short-term shear modulus (kPa)	Long-term shear modulus (kPa)	Decay constant (s)
Brain	41.0	7.8	0.00142857
(c) Ideal gas material parameters:			
Material	Density (kg/m^3)	Gas constant (J/(kg-K))	Temperature (K)
Air	1.1607	287.05	300

The previously measured incident pressure history of a planar Friedlander waveform [89] was used as the pressure boundary condition at the inlet of the Eulerian domain (Figure 3.3). The velocity perpendicular to each face of the Eulerian domain was kept equal to zero

to avoid escaping/leaking of air through these faces. This would create a pure 1D shock front traveling in the z-direction without lateral flow. The bottom of the skull was constrained in all six degrees of freedom to avoid rigid body translation. The tied constraint was used between the skull and brain. To incorporate the blood vessel networks into the surrogate head, the nodes of the vessels were merged with neighboring nodes of the brain.

3.3 Results

The computational framework has been validated against the experimental data in our previous work [89]. Briefly, repeated shock tube tests were conducted on a surrogate head, i.e., a water-filled polycarbonate shell located inside the shock tube. The intracranial pressure histories at three different locations were measured. Results show that the major features of the measured pressure profiles, including the peak pressure, nonlinear decay, and small peaks and valleys were captured by the simulation. The maximum deviation of the peak pressure in the brain was only 8.31%.

3.3.1 Blast-induced Pressure Surge in the Water

The pressure in the water was monitored (Figure 3.4) under two different blast intensities with the peak incident pressure at 0.15 MPa and 0.19 MPa, respectively. The peak water pressure increased from 0.25 MPa to 0.38 MPa with the increased incident pressure from 0.15 MPa to 0.19 MPa. It was observed that the peak water pressure was larger than that of the incident pressure. This was related to the observation of blood pressure surge and its resulted breakdown of the blood-brain barrier following the blast exposure [95, 96]. In addition, we have demonstrated that the largest reflected pressure occurred in the eye socket when the head was positioned facing the blast wave (to be described later). This

reflected pressure could cause a substantial increase in the pressure within the central retinal artery, which led to the vision impairment and even blindness [97, 98].

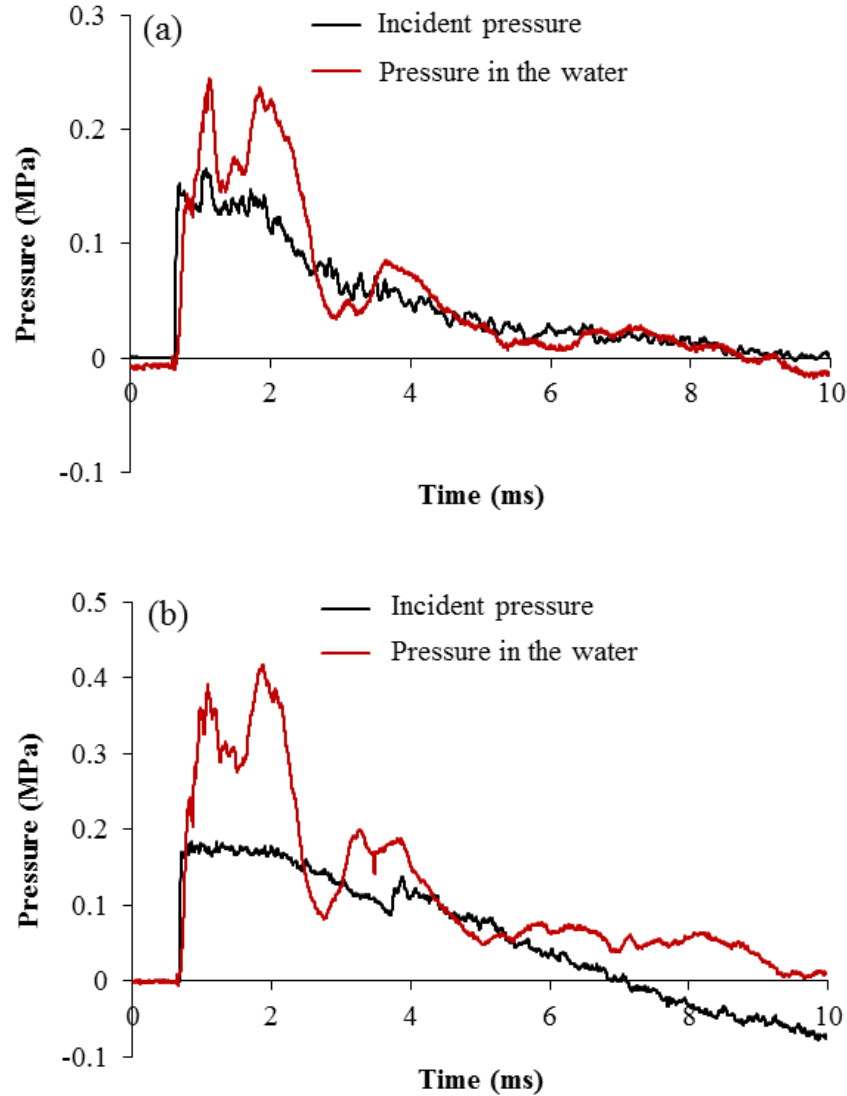


Figure 3.4: Comparison of incident pressure with pressure in the water. (a) Loading-1, peak magnitude of the incident pressure was 0.15 MPa; (b) Loading-2, peak magnitude of the incident pressure was 0.19 MPa.

The simulation predicted pressure-time history in the water for an incident pressure of 0.15 MPa was shown in Figure 3.5. Reasonable match between the simulation and the

experiment was observed. The first peak pressure was both observed around 0.5 ms, when the shock wave hit the gel and squeezed the inner latex tube. A second peak in the water pressure occurred around 1.3 ms, which could be attributed to the wave reflection at the latex tube. As time progressed, the pressure decayed gradually to zero. The overestimation of the pressure by the simulation could be due to the adopted material properties of gel and water from the literature.

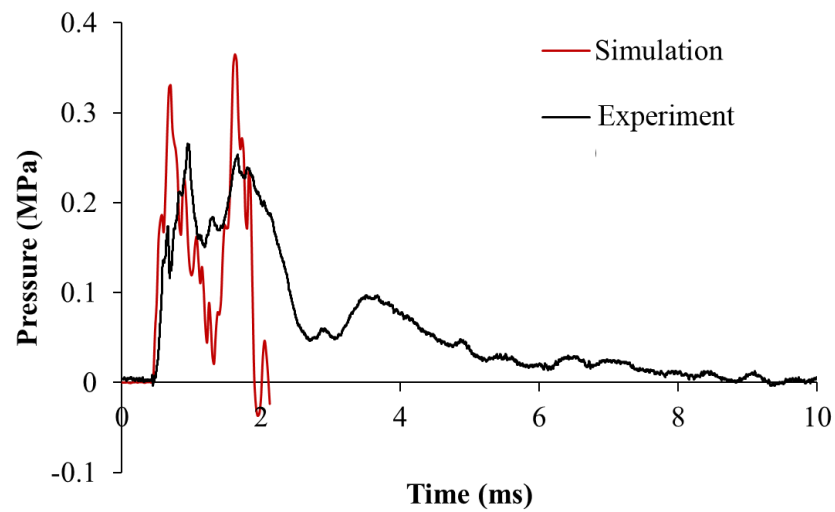


Figure 3.5: Comparison of pressure-time history in the water between the simulation and the experiment.

3.3.2 Effect of Latex Tube on the Strain Distribution in the Gel

Figure 3.6 has compared the maximum principal strain (MPS) averaged in the front area of the latex tube with the one at the back. It is observed that, without inserting the latex tube, the peak MPS in the front region was almost the same with that in the back region for both experiment and simulation (Figure 3.7). This indicates a homogeneous strain field in the gel under blast loading. However, after inserting the latex tube, this homogeneity was not maintained. Both experiment and simulation found that the peak MPS in the back

region was larger than that in the front region (Figure 3.6). Since the latex tube cannot take any effect on the gel response in its front side, only the variation occurred in its back side could be regarded as the role played by the latex tube. Thus, our results demonstrate that inserting a single latex tube will cause an increase of the strain in the gel. This provides support for our further hypothesis that blood vessel networks will weaken the structural responses of the brain under blast loading.

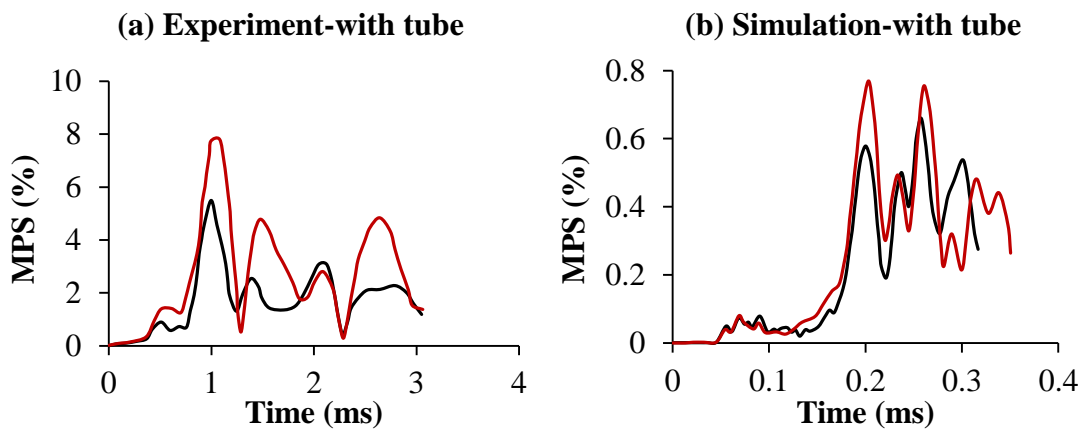


Figure 3.6: Comparison of maximum principal strain (MPS) histories in the gel which located at the front and back area of the latex tube.

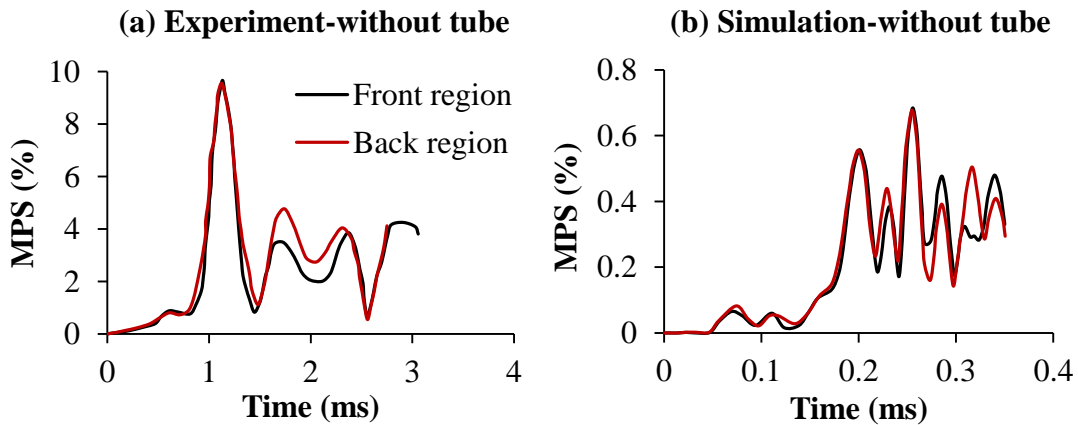


Figure 3.7: Comparison of maximum principal strain (MPS) histories in the gel which located at the equivalent front and back area of the latex tube.

It is observed that the peak MPS predicted by the simulation was about one order of magnitude smaller than that measured by the experiment. For example, without inserting the latex tube, the peak MPS in the front region was 0.7% by the simulation, compared to 10% by the experiment (Figure 3.7). This could be attributed to the approximation of material properties for the gel. In the simulation, the gel was assumed as an elastic material with its properties adopted from the brain [89]. Although gel has been proved as an acceptable surrogate for the brain [99, 100], the frequency-dependent viscoelastic properties between them could differ substantially. To minimize the deviation between the experiment and the simulation, it is necessary to measure the viscoelastic properties of the gel at the specific frequency of the blast loading.

Experimental results show that there was a significant decrease in the peak MPS after inserting the latex tube, regardless of the region considered (Figures 3.6 (a) & 3.7 (a)). However, such a variation was not observed in the simulation (Figures 3.6 (b) and 3.7 (b)). The deviation in experimental results could be explained by the difference in gel preparation for two cases, *i.e.*, with/without the latex tube. In the experiment, the gel was prepared separately for each case. It is difficult, if not impossible, to guarantee the mixing proportion and the curing time are exactly the same for two cases. The gel which prepared for the with-tube case might be stiffer, making the strain response of the gel to be smaller. However, such uncertainty of gel property does not exist in the simulation, and thus the strain response of the gel is more consistent.

The distribution of the MPS in the gel around the latex tube is shown in Figure 3.8. It is observed that high strains mainly occurred close to the latex tube. For the gel which located far away from the latex tube, the influence of the latex tube on the gel response was

minimal. The observation of the single latex tube is consistent with that of blood vessel networks. We found that blood vessel networks could only induce high strains in the brain which located close to the blood vessels (to be described later).

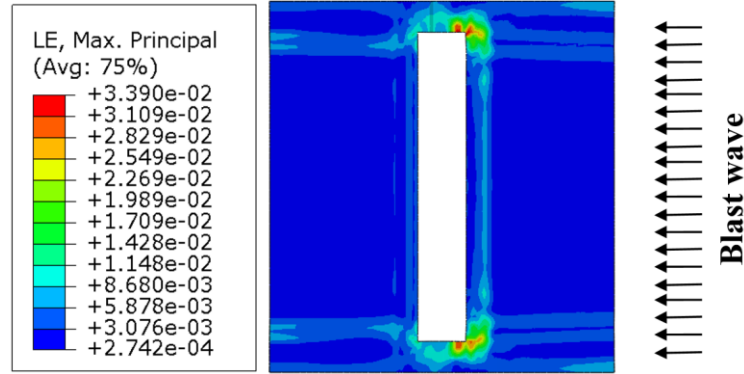


Figure 3.8: Distribution of maximum principal strain around the latex tube. The central white region indicates the location which previously occupied by the latex tube.

3.3.3 Effects of Blood Vessel Networks

In this work, three commonly used injury measures, MPS, SS, and ICP, were monitored at different regions of the brain to quantify the role of blood vessel networks in brain dynamics. The MPS responses at five locations in the mid-coronal plane of the brain were compared between two models (Figure 3.9). Locations represent the superior cortex (Region A), frontal cortex (Region B), occipital cortex (Region C), corpus callosum (Region D), and brainstem (Region E). The MPS magnitudes were averaged over four elements. The peak MPS predicted by the model with and without blood vessels did not differ much in Regions A, B, and C, with the maximum deviation less than 3.89%. However, in Regions D and E, the peak MPS within the model considering blood vessel networks was increased by 180.27% and 282.25%, respectively, compared to the one without blood vessel networks.

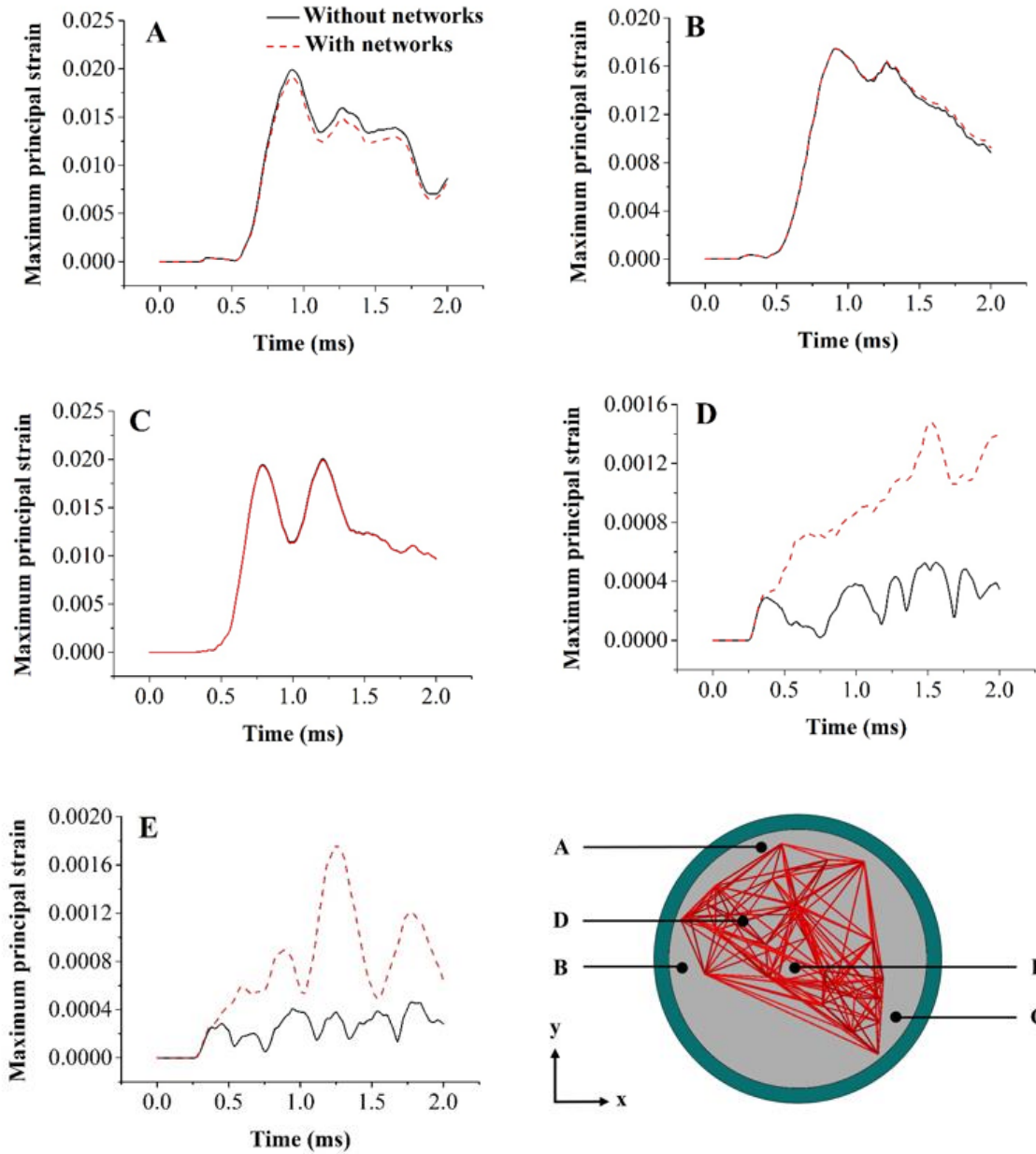


Figure 3.9: Comparison of maximum principal strain histories in five regions of the brain surrogate.

The Green-Lagrangian SS with respect to the y-z plane is used to compare the model responses. Figure 3.10 depicts the SS histories predicted by both models for the five regions described in the previous section. The predicted peak SS was as high as 3.68% and 3.53%

in Region A for both models. Except in Regions A and D, all regions exhibited peak SS in the positive direction. Similar to the MPS responses, the peak SS predicted by the model with blood vessels did not differ much from the model without blood vessels in Regions A, B, and C, with the maximum deviation less than 3.94%. However, the peak SS increased by 245.28% and 612.56% in Regions D and E, respectively, for the model with blood vessel networks.

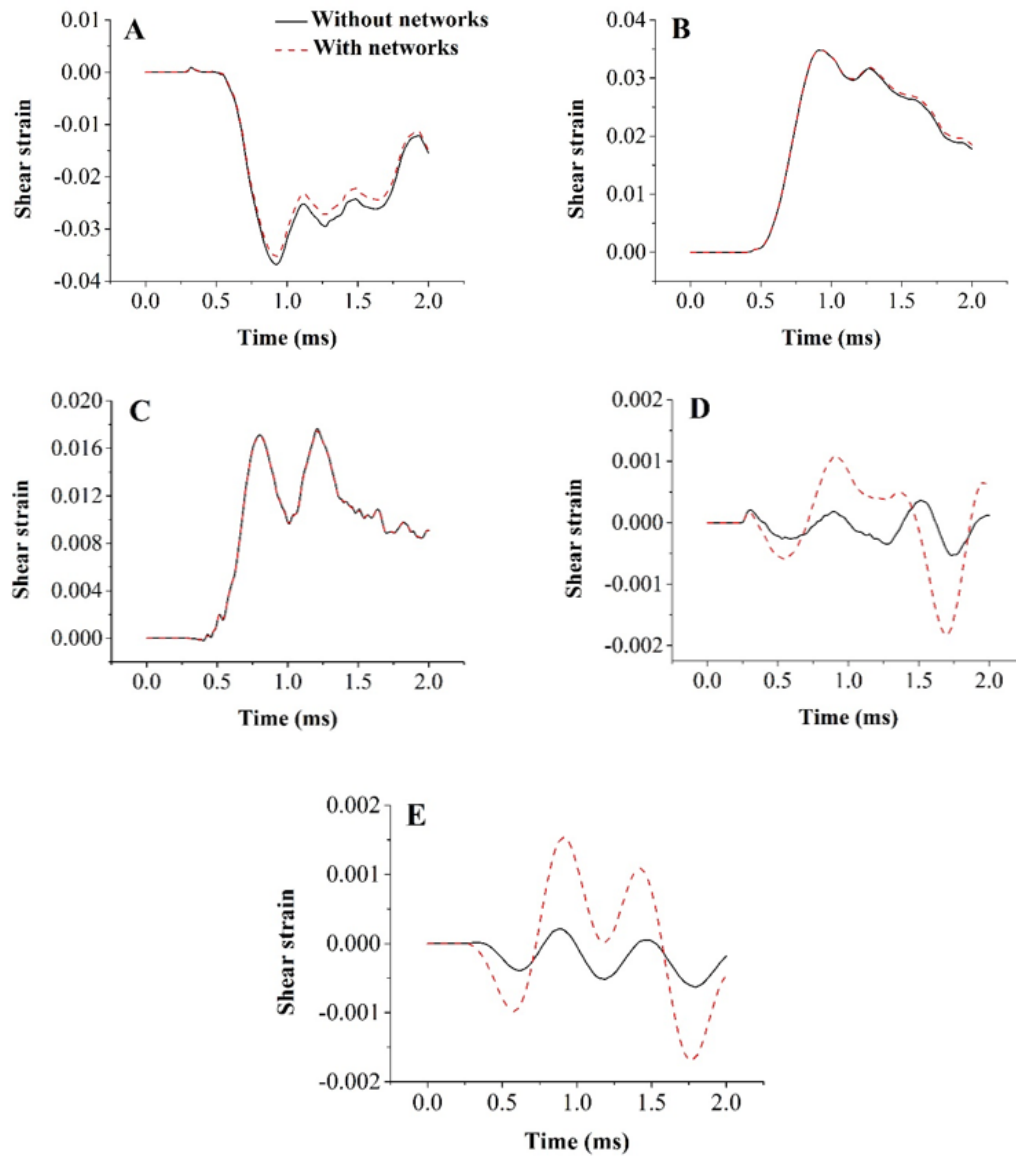


Figure 3.10: Comparison of shear strain histories in five regions of the brain surrogate.

The calculated ICP is also compared between the two models to determine the effect of modeling the blood vessel networks. Figure 3.11 illustrates the ICP contours in the mid-coronal plane of the brain at different times. It is observed that the inclusion of blood vessel networks did not have a significant effect on the ICP responses during the 2 ms time span. The complex wave pattern which generated within the brain was very similar in both models. This could be attributed to the reflection of waves from finite boundaries of the head, the presence of the skull which possesses significant shear strength, and the wave mode conversion at material boundaries and interfaces. Both models exhibited typical coup and countercoup pressure patterns throughout the brain on the early time scale (time = 0.28 and 0.35 ms). Once the early waves passed through the brain, mixed ICP patterns developed at the later time scale (time > 0.35 ms). The peak coup pressures were 0.518 and 0.520 MPa and the peak countercoup pressures were -0.062 and -0.067 MPa for the models without and with blood vessels, respectively. This coup-countercoup mechanism can cause contusion at early times and can widely spread throughout the brain at later times when mixed ICP patterns are dominant.

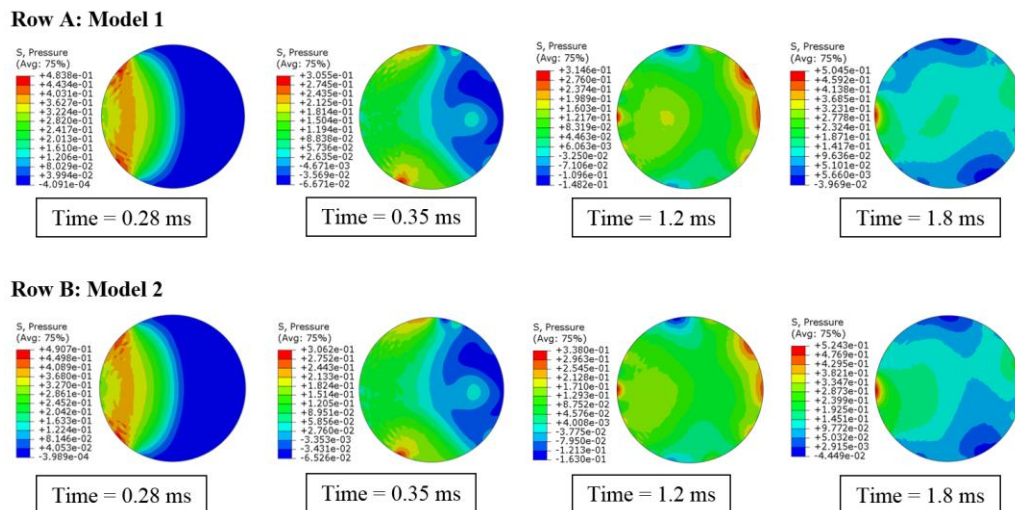


Figure 3.11: Snapshots of intracranial pressure distributions.

3.4 Discussion

Two simplified head models, with and without the inclusion of blood vessel networks, were developed to quantify the effects of cerebral vasculature on the dynamic responses of the brain under blast loading. Results show that explicit modeling of the blood vessel networks could induce higher strains within the brain, specifically within the denser network region (Regions D and E) as shown in Figures 3.9 and 3.10. This is consistent with the clinical observation that the axonal bulbs were located near the blood vessels for the patients who suffered blast-induced TBI [101]. In the periphery region (Regions A, B, and C) without many blood vessel networks, the alternations in brain responses are minimal. This could be explained by the stiffening effect of blood vessel networks inside the brain. It is also interesting to observe that the ICP responses of the brain are unchanged (Figure 3.11), indicating that the impedance of the brain was not affected by the addition of blood vessel networks.

We have assumed the blood vessel has the uniform diameter of 2.72 mm, which is approximately the averaged intracranial vessel dimension. A parametric study was performed by using two limiting intracranial vessel diameters (3.74 and 1.28 mm) measured by Monson [102] for understanding the influence of the vasculature diameter on brain dynamics. Results in terms of the peak MPS and peak SS within the embedded vessel network region (Regions D and E) of the brain is shown in Figure 3.12. It is clear that the peak MPS increased with the larger blood vessel size. As the blood vessel diameter increased from 1.28 to 2.72 mm, there were 57.66% and 60.38% increases in the peak MPS in Regions D and E, respectively (Figure 3.12 (a)). When the blood vessel diameter increased from the baseline case of 2.72 mm to 3.74 mm, the peak MPS in Regions D and

E increased by 63.36% and 40.83%, respectively. A similar trend is observed for the peak SS in regions D and E of the brain (Figure 3.12 (b)). This suggests that blood vessel diameter is an influential parameter on brain dynamics. The fine vascular network with varied diameters might alter the magnitude of brain responses, but the observations on the role of blood vessel networks in brain dynamics will be the same.

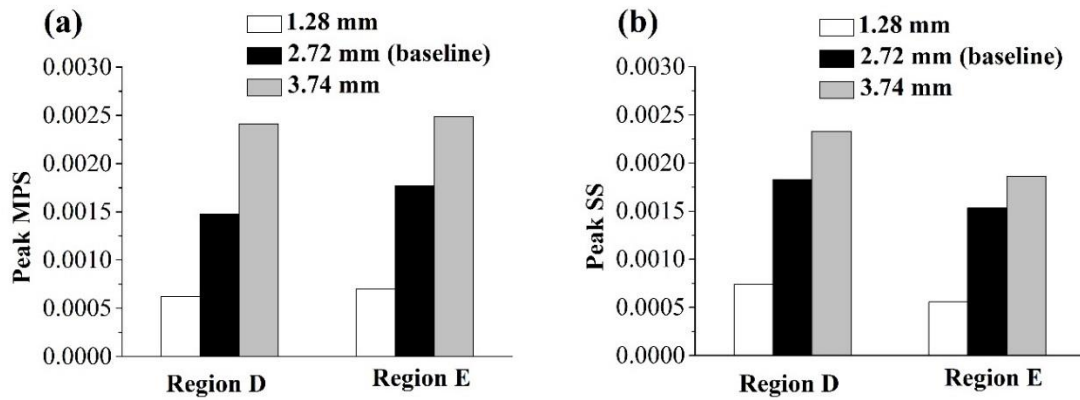


Figure 3.12: Comparison of peak maximum principal strain (MPS) and peak shear strain (SS) in the core region (Regions D and E) of the brain surrogate for different vasculature diameters.

The vasculature density also varied from person to person. For example, Ho et al. has quantified the intracranial vasculature density as 0.0037 mm/mm^3 based on the CT angiographies of the human brain [87]. Parnaik et al. calculated a much higher vasculature density of 0.0093 mm/mm^3 based on the magnetic resonance imaging [88]. We have intentionally adopted an intracranial vasculature density of 0.0047 mm/mm^3 in our baseline model. To understand the sensitivity of brain dynamics to the vasculature density, we created a denser blood vessel network of 0.0093 mm/mm^3 by increasing the number of tessellation nodes to 55 and the number of Voronoi edges to 342. The peak MPS and SS in regions D and E of the brain is compared between two different vasculature densities and

illustrated in Figure 3.13. When the vasculature density increased from 0.0047 to 0.0093 mm/mm³, the peak MPS in Regions D and E increased by 98.19% and 176.38%, respectively (Figure 3.13 (a)). In contrast, there were 39.09% and 76.40% decreases in the peak SS in Regions D and E, respectively (Figure 3.13 (b)). This opposite trend in the alternation of the peak MPS and SS might be explained by the configurations of the vascular network. Since the MPS is a predictor of diffuse axonal injuries as well as mechanical injuries to the blood-brain barrier [103, 104], this indicates that a higher density of blood vessel networks might lead to more severe brain injury. More clinical evidence could be used to examine this hypothesis.

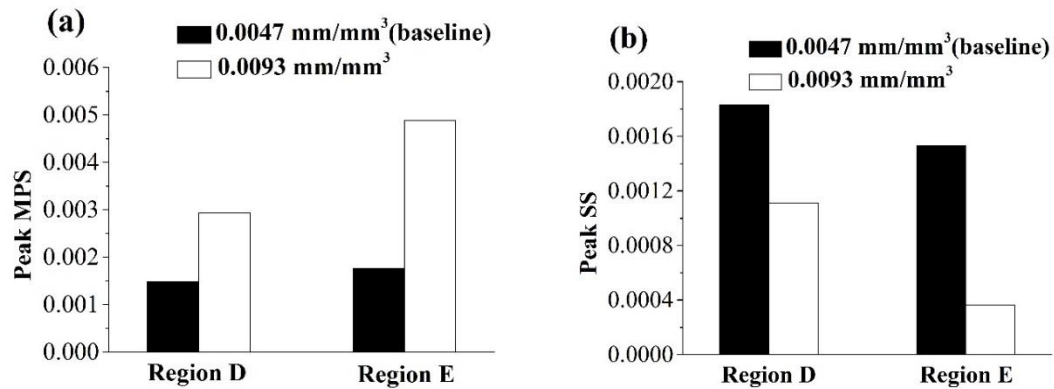


Figure 3.13: Comparison of peak maximum principal strain (MPS) and peak shear strain (SS) in the core region (Regions D and E) of the brain surrogate for different vasculature densities.

In the present model, the human head was simplified as a spherical head. An image-based human head model incorporating layers of head materials and various brain components might lead to different stress/strain magnitudes. In addition, constitutive models for both the brain and arteries were adopted from impact loading conditions due to a lack of testing data under higher frequency blast loading conditions, especially for the

artery. Our previous work has demonstrated that brain responses dramatically decreased in terms of peak ICP, maximum shear stress, and MPS under high-frequency blast loading conditions [105]. However, considering the comparative nature of this work, the role of vessel networks in brain responses might still hold true regardless of the frequency response. Moreover, the blood vessel networks were also assumed to be Voronoi tessellations with uniform diameter located in the central region of the brain mimicking its major branches. More realistic blood vessel networks will change the peak stress and strain histories in the brain. Despite these simplifications, the present work demonstrates the importance of blood vessel networks on brain dynamics, which may have significant clinical implications for TBI.

3.5 Conclusions

The effect of blood vessel networks on the dynamic responses of the brain under blast loading was investigated using two simplified head models with and without blood vessel networks. Results have shown that blood vessel networks could influence brain responses in complex patterns. Brain dynamics are also sensitive to the dimension and density of vasculature networks. This work can be used to provide a fundamental understanding of the behavior and impact of blood vessel networks on brain responses, to provide guidance for optimizing the performance of protective equipment, and to illuminate the possibilities for exploiting the potential to minimize TBI.

Chapter 4

Head Orientations Influence Brain Dynamics Subjected to Blast Loadings

4.1 Introduction

Blast-induced traumatic brain injury (TBI) has been gaining increased attentions for designing better diagnostic and protection measures [106]. Current protective armors have demonstrated its efficacy against blunt impacts, shrapnel or projectiles, but they are not designed for protection against blast waves, leading to an increased incidence of blast-induced TBI [84, 107]. Specifically, the head orientations could affect the level of TBI subjected to impact or inertial loading [90, 108, 109]. However, little is known about the directional dependence of head responses under blast loading conditions. Taylor et al. [18] simulated three different human head orientations with respect to the oncoming blast wave, i.e., head facing blast, head facing away from blast, and right side of the head exposed to blast. They found that the head orientation had negligible impact on the orbitofrontal regions and the posterior fossa (cerebellum and brain stem). From the numerical study by Zhang et al. [110], the peak coup pressure was found when the right side of the head was exposed to the blast, and the peak contrecoup pressure was observed when the head faced

the blast. This contradicted the findings of Taylor et al. [18]. Rat models [63, 111] were also utilized to investigate the role of head orientation in brain dynamics. Both studies stated that the peak intracranial pressure (ICP) was measured when the head faced the blast. In addition, for all these studies regarding the role of head orientation, the detailed characterizations of the blast wave-head interactions and load transfer mechanism into the brain were less characterized.

In this work, we delineated the effect of head orientation on the mechanics of the blast wave-head interactions as well as the load transfer to the brain through the finite element (FE) method. A three-dimensional (3D) human head model with anatomical details was reconstructed from computed tomography (CT) data. It was then positioned in three different orientations with respect to the oncoming wave direction; head facing blast, head facing away from blast, and right side exposed to blast. The intensity of blast overpressures that exerted at the vicinity of the head was monitored. The brain responses in terms of ICP and maximum principal strain (MPS) were also computed.

4.2 Finite Element Modeling

A human head model was reconstructed from CT data, which consisted of 73 axial scans of 512^2 pixels taken at 3 mm intervals in an adult male head. The image data were segmented into three different tissue types of the head, i.e., skull, cerebrospinal fluid (CSF), and brain (Figure 4.1). The segmentation was realized using the 3D image analysis algorithm implemented in Mimics[®] (Materialise, Inc., Leuven, Belgium). The skull included most of the anatomical structures such as the frontal, occipital, and temporal bones as well as the eye sockets. Followed by segmentation, the head model was imported into

HyperMesh[®] (Altair Engineering, Inc., MI, USA) through an STL file and discretized into 159,621 10-noded modified quadratic tetrahedron elements (C3D10M). It was then subjected to a planar blast loading mimicking the in-house shock tube as described in our previous work [89]. Briefly, the measured incident pressure history with peak value of 0.22 MPa was used as the pressure boundary condition at the inlet of the Eulerian domain ($400 \times 400 \times 1000$ mm) filled with air. It consisted of 1,300,000 brick elements with appropriate mesh refinement near the region of the human head to capture the effect of fluid-structure interaction. The velocity perpendicular to each face of the Eulerian domain was kept equal to zero to avoid escaping/leaking of air through these faces. This would create a planar blast front traveling along the incident direction without lateral flow. The head model with a fixed bottom was immersed in the Eulerian domain and their interaction was enforced through a penalty contact algorithm with frictionless tangential sliding and hard contact normal behavior. The blast wave-head interaction model, governed by partial differential equations of conservation of mass, momentum and energy along with the material constitutive equations and boundary conditions, was solved in ABAQUS/Explicit analysis software (Simulia, Inc.).

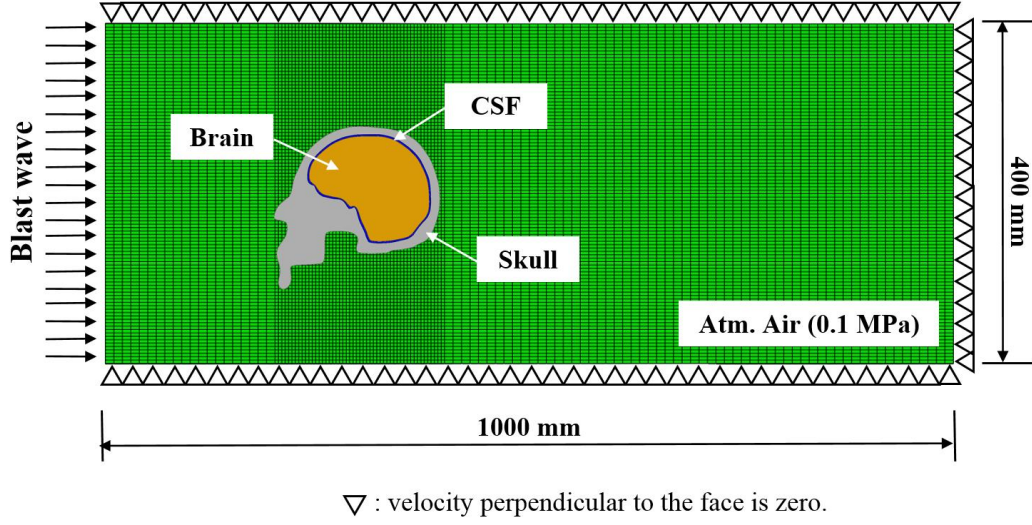


Figure 4.1: Finite element model of the human head subjected to blast loading (midsagittal view).

The skull was modeled as a homogeneous linear elastic isotropic material and the Young's modulus and Poisson's ratio were assumed as 5.37 GPa and 0.19, respectively [90]. The brain was assumed to be linear viscoelastic with a short-term shear modulus of 41 kPa and a long-term shear modulus of 7.8 kPa [112]. The CSF was modeled as an incompressible fluid using the linear Mie-Grüneisen equation of state, which related the blast velocity and fluid particle velocity to the pressure inside the CSF [113]. The air was modeled as an ideal gas equation given by

$$P = (\gamma - 1) \frac{\rho}{\rho_0} e$$

where P was the pressure, γ was the constant pressure to constant volume specific heat ratio (1.4 for air), ρ_0 was the initial air mass density, ρ was the current mass density, and e was the internal volumetric energy. The Mach number of the blast front measured in our previous experiment was approximately 1.4. Hence, ideal gas equation of state assumption

is valid, as the ratio of specific heats do not change drastically for this Mach number. A summarization of the material properties is illustrated in Table 4.1.

Table 4.1: Material properties used in the finite element simulation.

(a) Elastic material properties:				
Material	Density (kg/m ³)	Young's modulus (MPa)	Poisson's ratio (/)	
Skull	1710	5370	0.19	
Brain	1040	1.314	0.4999	
(b) Viscoelastic material properties:				
Material	Short-term shear modulus (kPa)	Long-term shear modulus (kPa)	Decay constant (ms)	
Brain	41	7.8	700	
(c) Incompressible fluid EOS parameters:				
Material	Viscosity (N·s/mm ²)	Sound speed (mm/s)	Hugoniot slope coefficient (/)	Grüneisen's gamma (/)
CSF	1 × 10 ⁻⁸	1.48 × 10 ⁶	0	0
(d) Ideal gas material parameters for air:				
Material	Density (kg/m ³)	Gas constant (J/kg·K)	Temperature (K)	
Air	1.1607	287.05	300	

4.3 Results

The computational framework has been validated against our experimental work [89]. Briefly, repeated shock tube tests were conducted on a surrogate head, i.e., a water-filled polycarbonate shell located inside the shock tube. The ICP histories at three different locations were measured. Results show that the major features of the measured pressure profiles, including the peak pressure, nonlinear decay, and small peaks and valleys were captured by the simulation. The maximum deviation of the peak pressure in the brain was only 8.31%.

To examine the influence of head orientation on the mechanics of blast wave-head interactions, we monitored the reflected pressure histories at four different locations around the head (Figure 4.2). Locations R1 – R4 represent the frontal bone, eye socket, occipital bone, and temporal bone, respectively. In the front-on (head facing blast) case, the maximum reflected pressure of 0.67 MPa was observed at location R2 (eye socket). Compared to the incident pressure of 0.22 MPa, the reflection factor Λ (ratio of the reflected pressure to the incident pressure) was calculated as 3.0. As the blast wave traversed the head, the reflected pressure decreased from locations R1 ($\Lambda = 1.8$) to R3 ($\Lambda = 1.6$), and the minimum reflected pressure was observed at location R4 ($\Lambda = 1.1$). In the back-on (head facing away from blast) and side-on (right side exposed to blast) cases, the maximum reflected pressures were observed at locations R3 ($\Lambda = 2.0$) and R4 ($\Lambda = 2.1$), respectively. However, both of them were smaller compared to the reflected pressure measured at location R2 ($\Lambda = 3.0$) in the front-on case.

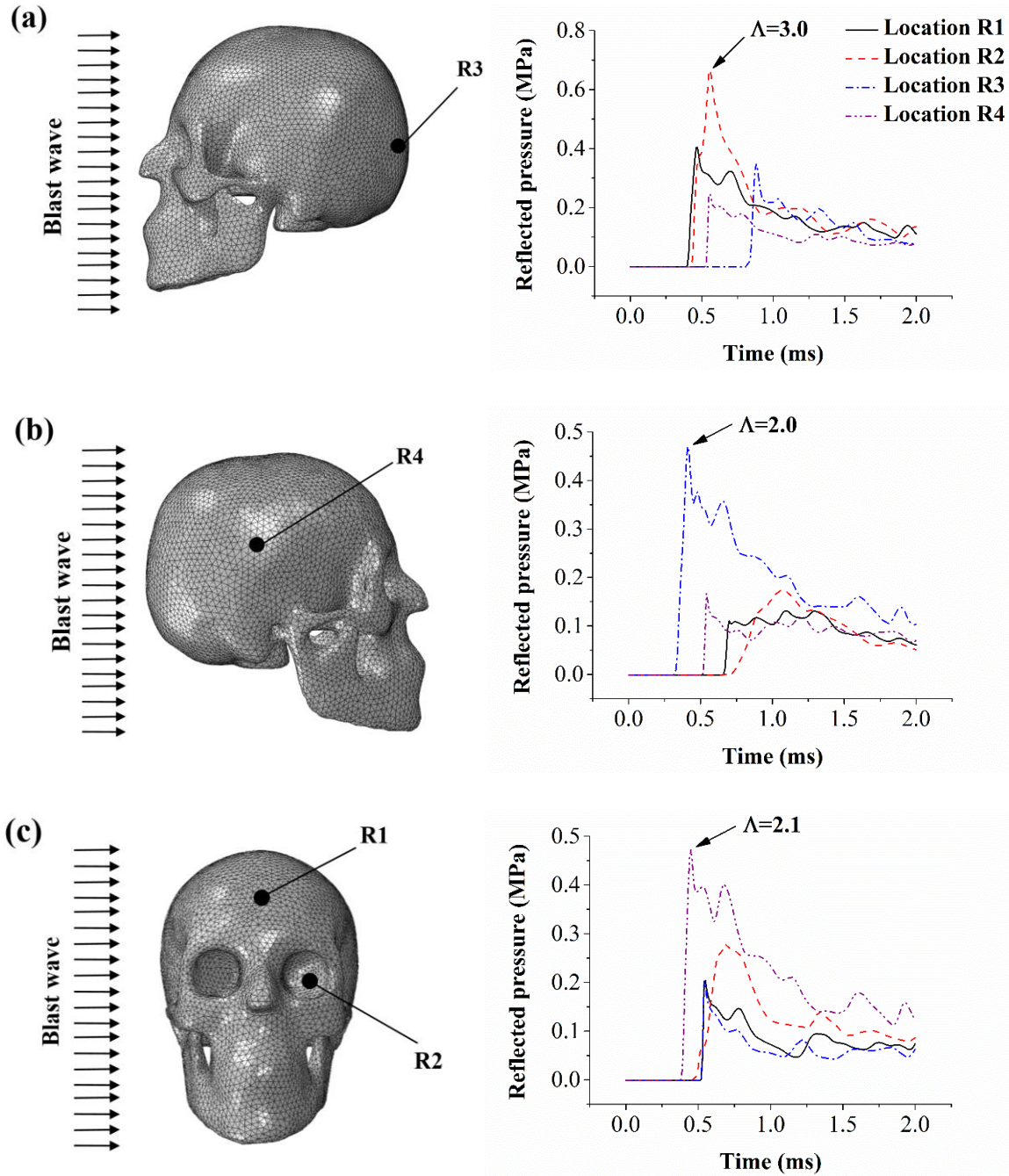
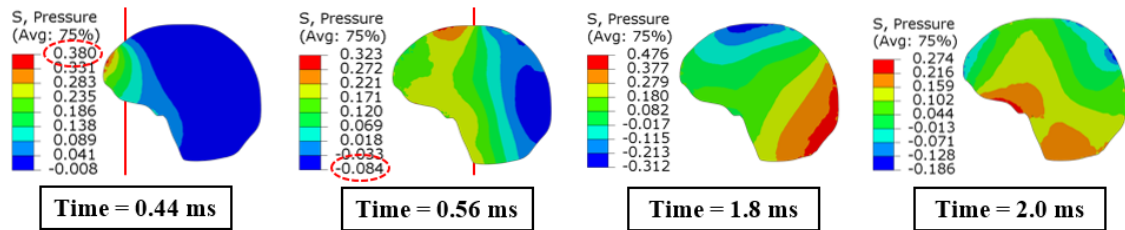


Figure 4.2: Comparison of the reflected pressure histories at four locations around the head for (a) front-on, (b) back-on, and (c) side-on cases.

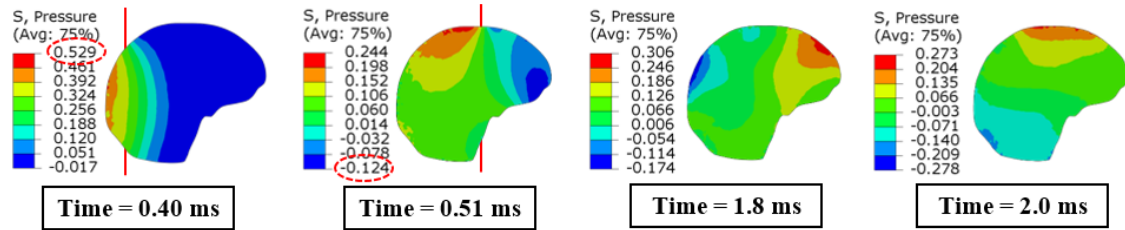
The intracranial wave propagations under different head orientations are illustrated in Figure 4.3. All three head orientations exhibited typical coup and contrecoup pressure

patterns throughout the brain while the blast wave front passed through the head as shown in the first two snapshots of the ICP distributions. Once the blast wave front passed over the head, complex ICP pattern developed due to the wave reflection and skull flexure as depicted in the last two snapshots. The peak coup pressures were 0.380, 0.529, and 1.031 MPa and the peak contrecoup pressures were -0.084, -0.124, and -0.069 MPa in the front-on, back-on, and side-on cases, respectively (indicated by the dashed circle).

Row A: front-on case (midsagittal view)



Row B: back-on case (midsagittal view)



Row C: side-on case (midcoronal view)

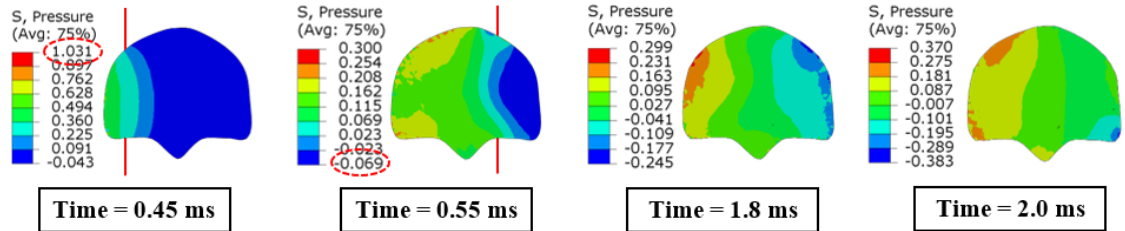


Figure 4.3: Snapshots of intracranial pressure distributions for front-on, back-on, and side-on cases.

The role of head orientation in the peak MPS was also obtained at four critical regions of the brain (i.e., frontal cortex, superior cortex, occipital cortex, and brainstem) as shown

in Figure 4.4. In the frontal cortex region, the peak MPS subjected to the front-on or side-on orientation were 37.4% and 34.8% higher than the one in the back-on case. In the superior cortex region, the peak MPS occurred in the case of side-on ordination (0.017). In the occipital cortex region, the peak MPS was observed in the cases of back-on or side-on orientations (~ 0.014). In the brainstem region, the peak MPS (0.003) was observed in the front-on case.

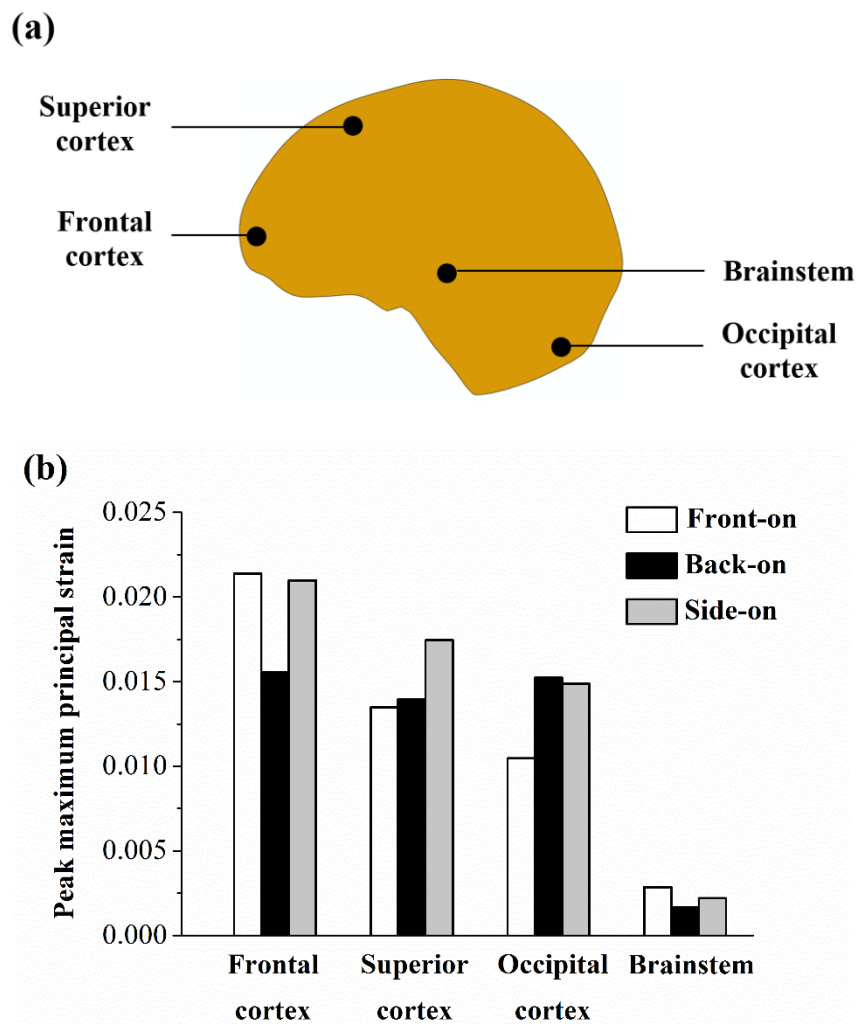


Figure 4.4: (a) Four regions in the midsagittal plane where the peak maximum principal strain was measured, and (b) comparison of the peak MPS for front-on, back-on, and side-on cases.

4.4 Discussion

A 3D FE human head model was developed to investigate the role of head orientation in transmitting blast waves to the brain. The detailed blast wave-head interactions as well as the ICP and MPS responses in the brain were characterized. As the blast wave front hit the head, the incident wave pressure was amplified due to the local fluid-structure interaction (Figure 4.2). This pressure amplification behavior can be attributed to the aerodynamic effects in which the high-velocity particles of the wave front are brought to rest abruptly, leading to an amplified reflected pressure acting on the solid surface of the head. The reflection factor can vary from 2 to 8, depending on several factors such as the incident blast intensity, fluid medium in which blast wave travels, angle of incidence, mass and geometry of the object [89, 114]. Our results show that the maximum reflected pressure occurred at the eye socket (location R1, $\Lambda = 3.0$) in the front-on case due to the concave shape of the eye socket. In contrast, the peak reflected pressures in the back-on and side-on cases were located at the occipital bone (location R3, $\Lambda = 2.0$) and temporal bone (location R4, $\Lambda = 2.1$), respectively. This is expected since the curvature of the skull surface impacted by the wave front was positively correlated with the reflected pressure [59].

The reflected pressure exerted on the skull resulted in different ICP patterns within the brain under various head orientations. In all three head orientations, the peak positive pressure (compression) was observed at the coup site and the peak negative pressure (tension) was at the contrecoup site (Figure 4.3). The maximum coup pressure of 1.031 MPa was found in the side-on case while the minimum one of 0.380 MPa was in the front-on case. This is consistent with the reflected pressure pattern on the skull, i.e., the maximum reflected pressure was at the temporal bone (location R4, $\Lambda = 2.1$) in the side-on case and

the minimum one was at the frontal bone (location R1, $\Lambda = 1.8$) in the front-on case. All these observations could be attributed to the skull geometry. Compared to the frontal bone, the temporal bone has a relatively flat contact surface and a relatively larger span. As a result, the skull will experience more loading in the side-on case, leading to a larger coup pressure in the brain. Although the maximum reflected pressure occurred at the eye socket in the front-on case, the relatively small area interacted with the blast wave resulted in minimal ICP in this case. Our results also showed that the back-on case led to the maximum contrecoup pressure. This is consistent with the clinical observation that the patients who suffered from a back impact usually have contusions in the frontal lobe [115]. It should be also noted that our observations were totally different with the published computational work [110].

The peak MPS at four functional regions of the brain were extracted from our numerical results (Figure 4.4) since the brain MPS was speculated to be correlated with the diffuse brain injury [116-118]. It was observed that, regardless of the head orientation, the peak MPS was generally larger in the frontal cortex region than in other regions. This is attributed to the relatively rough features of the frontal skull. Moreover, the local peak MPS within each individual function region of the brain depended on the head orientation. Specifically, in the frontal cortex region, the peak MPS was observed in front-on and side-on cases, while in the occipital cortex region, the peak MPS was obtained in the back-on case. These could indicate that the frontal cortex were prone to TBI especially in the front-on and side-on cases, while the occipital cortex was the vulnerable one in the back-on case. This clearly shows that head orientation results in different brain dynamics, which is also region-specific. This observation is contradictory to Taylor's work [7], which observed

that no difference among three head orientations. This could be attributed to the adopted boundary conditions at the head. Specifically in their work, the head was free from any constraints, which resulted in a 1 mm displacement of the head during the 2 ms simulation. This could explain why they didn't observe the difference between head orientations.

Even in this work, only the head bottom was constrained and the head-neck junction was not considered [119]. The skull was also simplified as homogeneous and isotropic material. More realistic models considering heterogeneous skull properties could alter the brain dynamics. Despite these simplifications, the present work demonstrated the importance of head orientations on estimating the blast-induced TBI.

Chapter 5

An In Vitro Injury Model for Primary Cortical Astrocytes

5.1 Introduction

Traumatic brain injury (TBI) is the leading cause of disability in people under 40 years of age and severely disables 150-200 per million people annually resulting in heavy psychological and financial burden on society [120-122]. Severe TBI has received the most concern considering the gravity of the immediate symptoms and the high fatality risk. However, a majority of TBI cases are mild or moderate which can result in wide spread tissue damage without any other symptoms resulting in ignorance for the need of treatment [123]. Furthermore, the immediate and long-term effects of mild TBI are variable and largely unknown, hindering diagnosis, treatment, and recovery [124]. Research efforts make slow but steady progress as the complexity of the brain and the heterogeneous nature of traumatic injuries have proven a formidable challenge requiring an array of physical and computational models [125-127].

In the past decade, researchers have shifted focus from preventative measures to diagnosis and treatment which has required sophisticated animal and cellular investigations

to discern biochemical pathways deviated by specific physical input (acceleration, force, blast, etc.) [123] To date, most studies have focused on pathophysiology of neurons as neurodegeneration is a key concern in the long-term behavioral effects of TBI. However, recent advances highlight the formation of glial scarring, disturbance in ion homeostasis and energy metabolism as well as excessive extracellular glutamate playing a key role in neurodegeneration [126, 128]. As these functions fall primarily in the domain of glial cells, specifically astrocytes, this brings to light the question regarding the role of astrocytes in TBI progression and healing [129].

Astrocytes are the most abundant cell type in the brain which perform a number of roles for healthy tissue function [130]. In the event of injury astrocytes take on a reactive phenotype which has been seen in animal models of mild to moderate TBI [128, 131]. Studies of astrogliosis provide insight into the potential toward healing or injury progression that glial scarring may provide. However, the isolation of specific molecular changes in TBI induced astrogliosis cannot be determined with the current models due to the complexity of TBI and the brain tissue microenvironment [132]. A few *in vitro* models have been developed which imposed certain characteristics of TBI (compression, shear, stretch, etc.) on mono-cultured cells to isolate astrocyte specific reactions; however, most injury models struggle with verification of substrate deformity or reproducible injury [127]. Assurance of reproducible injury requires the development of an *in vitro* model with an accurate quantification of substrate strain for determining the tolerance criteria and dose response. Finite element analysis can provide a physically based framework for quantifying the spatial and temporal distributions of strain as well as integrating discrete experimental measurements.

In this work, we describe the characterization of an *in vitro*, biaxial Controlled Cellular Injury (CCI) device to study traumatic injury in primary cortical astrocytes. Finite element

models, calibrated by high-speed imaging and a theoretical model, were developed to determine the membrane strain based on the controlled nominal pressure and nominal time in the CCI device. The effect of membrane strain on the primary cortical astrocyte viability and morphology was also identified.

5.2 Material and Methods

5.2.1 Astrocyte Culture

This study was carried out in strict accordance with the Committee on the Ethics of Animal Experiments at the University of Nebraska-Lincoln (Project ID: 1046). Primary cortical astrocytes were prepared from 1-3 day-old Sprague-Dawley rat pups (Charles River CD strain) according to previously established protocols with slight modifications [133, 134]. The tissue was dissociated with 0.25% Trypsin (Life Technologies) and 0.016% DNase (Roche). The trypsin was quenched by “astrocyte media” (DMEM (MP Biomedicals), 10% fetal bovine serum (Atlanta Biologicals), and 1% penicillin-streptomycin (Life Technologies)). The dissociated tissue was pelleted by centrifugation at 1800 rpm for 5 min, suspended in astrocyte media and gently homogenized with glass pipette. The homogenate was passed through a 70 μ m cell filter, centrifuged, and suspended in media. The cells were seeded on tissue culture dish (TCD) and day *in vitro* (DIV) two was vigorously shaken to remove loosely attached cells. The media was exchanged for fresh media and astrocytes allowed to grow until confluent. When confluent, cells were passaged by removal from the culture dish via TrypLE (Thermo Fisher Scientific) and split to accommodate continued expansion. Cultures were characterized by fluorescent microscopy using anti-GFAP antibody (Dako) and 4',6-diamidino-2-phenylindole (DAPI)

nuclear stain (Thermo Scientific) yielding cultures of > 90% GFAP positive cells as outlined previously [134].

5.2.2 Cell Damage Experiment Setup

The cell damage device was originally designed to study axonal injury [135] and then modified to achieve a wide range of strains and strain rates [136]. The device consists of an aluminum cover block, a custom-made stainless steel culture plate, an aluminum supporting base, and an air pulse-generating system (Figure 5.1 (a)). The stainless steel plate has a central circular hole with a radius of 11 mm. The culture surface consists of a silicone membrane (Specialty Manufacturing Inc., Saginaw, MI) positioned underneath the stainless steel plate and held in place using an O-ring. The stainless steel plate is attached to the cover block, creating a sealed chamber. The cover block consists of a quartz viewing window in the center, an inlet for compressed air, and a dynamic pressure transducer (Entran model EPX-V01-25P-/16F-RF, Fairfield, NJ) to monitor the pulse pressure in the chamber. The introduction of compressed air into the chamber is gated by a solenoid (Parker General Valve, Elyria, OH), in which the nominal pressure (i.e., pressure of the compressed air) and the nominal time (i.e., duration of the compressed air) can be regulated independently. The nominal settings (pressure and time) used in this study are listed in Table 1. The pressure transducer are monitored by an analog-to-digital board (Keithley Metrabyte, Cleveland, OH) integrated with a computer data acquisition system (Capital Equipment Corporation, Billerica, MA). A representative pulse pressure is illustrated in Figure 5.1 (b). The data are acquired at a sampling rate of 10 kHz. This pulse pressure then induced the membrane deformation, leading to cell damage.

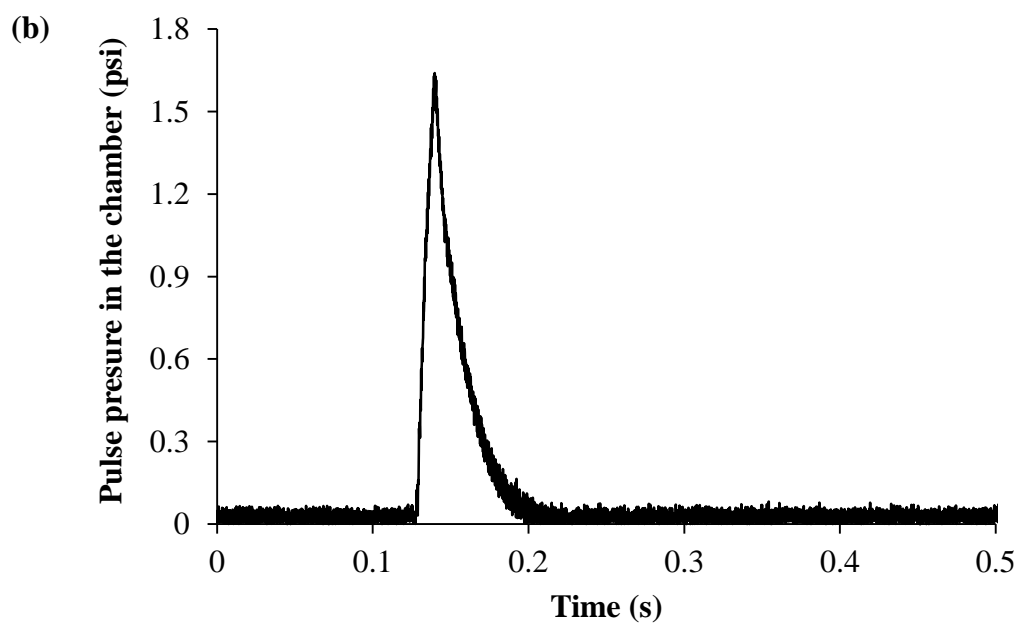
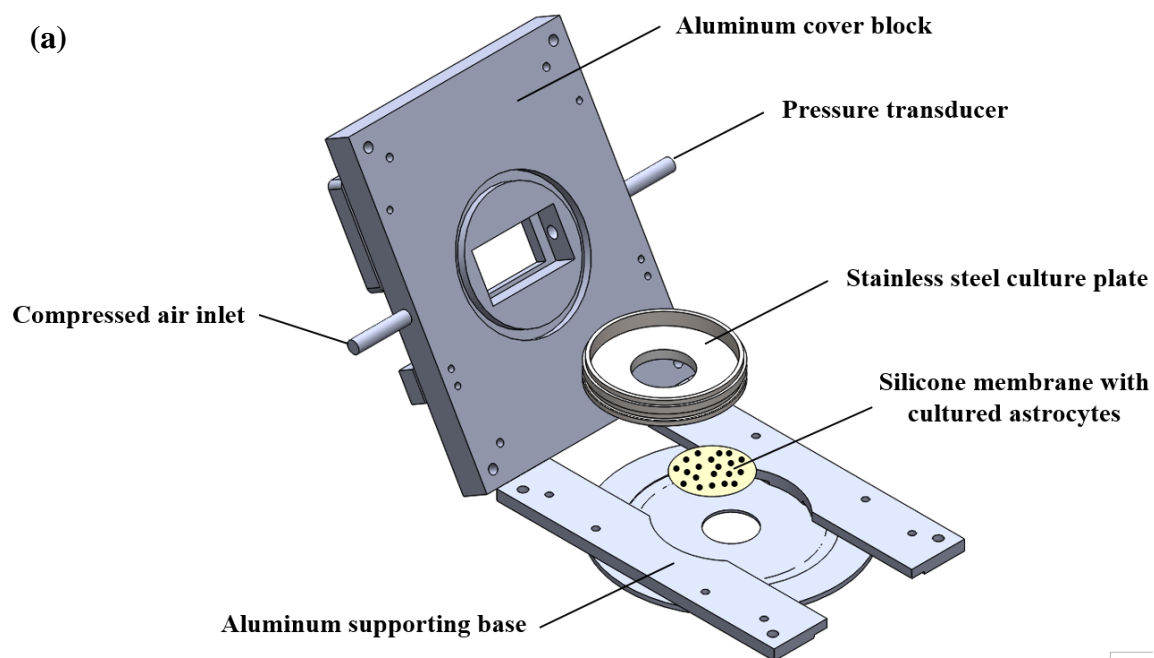


Figure 5.1: (a) A schematic view of the cell damage device, (b) a representative pulse pressure measured by the pressure transducer at nominal pressure of 5 psi and nominal pressure of 10 ms.

5.2.3 High-Speed Camera for Capturing Membrane Dynamics

The membrane dynamics were monitored using a Photron FASTCAM SA1.1 high-speed camera (Photron USA Inc., San Diego, CA) equipped with a Nikon f/2.8 105 mm macro lens. The cell damage device was positioned in front of the camera and illuminated by a MI-150 fiber optic illuminator (Edmund Optics, Barrington, NJ). The displacement history of the membrane subjected to the compressed air was captured with resolution of $1,024 \times 1,024$ pixels at 5,000 frames per second (corresponding to 0.2 ms per frame). The peak membrane displacement for each nominal setting (Table 5.1) was obtained using ImageJ software (National Institutes of Health, Bethesda, MD).

Table 5.1: Nominal settings (pressure and time) used in this study with corresponding peak membrane displacement and average membrane strain.

Test No. (/)	Nominal pressure (psi)	Nominal time (ms)	Peak membrane displacement (mm)	Average membrane strain (%)
1	5	10	3.47 ± 0.44	8.25
2	5	15	5.63 ± 0.23	16.51
3	5	20	6.66 ± 0.05	21.69
4	15	10	7.43 ± 0.50	25.86
5	10	15	8.87 ± 0.47	33.65
6	20	10	9.51 ± 0.29	37.09
7	25	10	11.17 ± 0.17	45.19
8	15	20	12.78 ± 0.26	55.18*
9	25	15	15.33 ± 0.27	71.56*
10	20	20	15.66 ± 0.22	73.77*
11	25	20	17.38 ± 0.33	85.75*

* The data were extracted by curve fitting using Eq. (5.4), not by the simulation.

5.2.4 Finite Element Modeling

Pulse pressure-induced membrane deformation was simulated using commercial finite element software ABAQUS (Dassault Systems Simulia Corp., RI). The radius of the membrane was set as 11 mm, the same as the radius of the central circular hole in the stainless steel plate. The thickness of the membrane was measured as 0.127 ± 0.006 mm. The translational degrees of freedom at the membrane edge were constrained to mimic the setup of the cell damage device. The Young's modulus of the membrane was determined as 1.1 MPa from in-house uniaxial tensile tests. The membrane was assumed as isotropic, linear elastic, and nearly incompressible material with a Poisson's ratio of 0.47. The mass density of the membrane was adopted as $1,100 \text{ kg/m}^3$ [137]. The model was meshed with 4-node doubly curved general-purpose shell elements with finite membrane strains (S4). Five section integration points with Simpson's integration rule were used in each shell element. A mesh convergence test was conducted and the minimum mesh size was chosen as 0.3 mm. There were a total of 3,955 nodes and 3,884 elements.

5.2.5 Cell Injury

Passage 2-3 astrocytes were seeded on poly-L-lysine (PLL), a standard tissue culture dish coating utilized for neuronal cells to promote cell attachment, coated PDMS membranes attached to steel culture dish as previously described. Astrocytes were injured by the following method utilizing the nominal pressure and pulses determined to initiate membrane strain between 0-85%, a range which has been seen in animal models of TBI [22, 138] via biaxial strain. A schematic view of the injury process is shown in Figure 5.2. Briefly, the injury culture dish with astrocytes was removed from the incubator, culture

media aspirated and the dish mounted in the device and the membrane stretched to the calibrated strain corresponding to inlet pressure and time duration in Table 5.1. Immediately after injury cells were immersed in DMEM or 1 X PBS and phase images used to confirm cell injury by Axiovert 40 CFL (Zeiss).

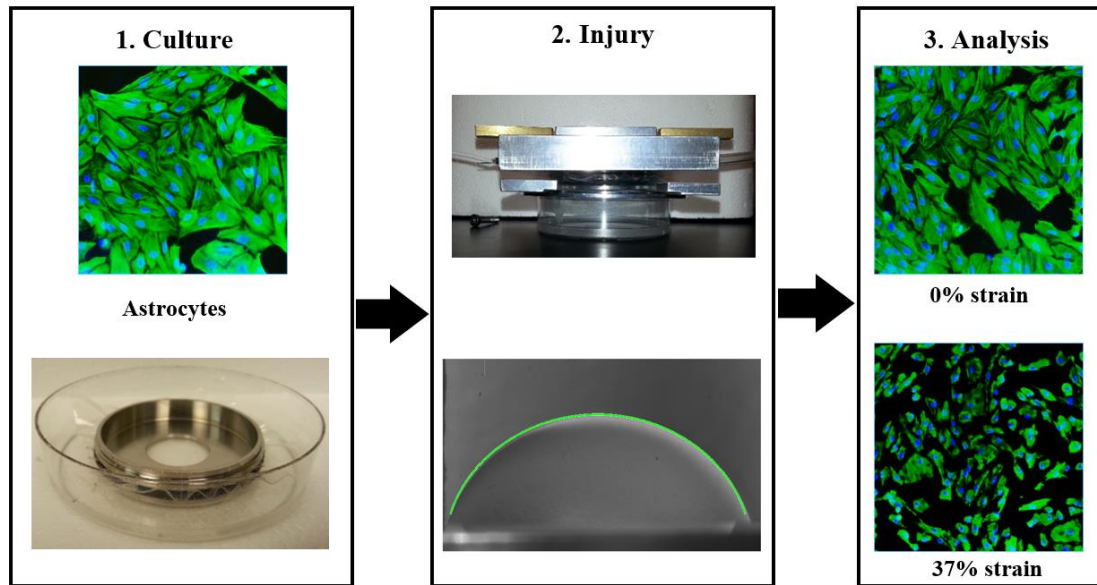


Figure 5.2: A schematic view of the astrocyte injury process.

5.2.6 Cell Injury Quantification

Cell injury was assessed via Live/Dead assay (Thermo Fisher Scientific) as a per cell analysis via flow cytometry. Live/Dead cell viability assay utilizes ethidium bromide homodimer (Ethd-1, red) and calcein-AM (green) to determine viability based on plasma membrane integrity and esterase activity. Following injury astrocytes were removed from the silicone membrane via TrypLE. The cell suspension was centrifuged, supernatant removed and the pellet suspended in DMEM containing Ethd-1 and calcein AM, according to manufacturer instruction, and incubated at RT for 20 min protected from light. The dye was removed by centrifugation, cells washed with 1 X PBS and suspended in DMEM for

flow analysis (FITC ex 488 em 530/30 and PE ex 488 em 585/42, 10,000 events/read) against cells not treated with dye. Cells were determined “live” or “healthy” by staining with only calcein, “dead” by staining with only Ethd-1 and “injured” by staining with both dyes.

5.2.7 Statistical Analysis

All cell data is presented as the mean \pm standard deviation. Statistical comparisons between treatments utilized SigmaPlot one-way ANOVA (Student-Newman-Keuls) and pool size as indicated.

5.3 Results and Discussion

5.3.1 Cell Damage Device Characterization

The nominal pressure and nominal time are two independent inputs determining the peak membrane displacement, as measured by the high-speed camera (Figure 5.3). A 3D surface response plot of the peak membrane displacement as a function of nominal pressure/time is depicted in Figure 5.4 and could be expressed by a linear regression equation:

$$w = 0.46p_n + 0.52t_n - 4.63, R^2 = 0.97 \quad (5.1)$$

where w is the peak membrane displacement, p_n is the nominal pressure (range up to 25 psi), and t_n is the nominal time (range up to 20 ms). The time coefficient shows that the nominal time has a little more impact than the nominal pressure on the peak membrane displacement. This correlation between cell damage device inputs and the resulted membrane displacement could be used for pre-test planning and post-test analysis, as described later.

The measured pulse pressure is also related to the displacement of the membrane, which is typically demonstrated as a linear correlation in literature [136]. The correlation between the peak membrane displacement and the pulse pressure in this work is depicted in Figure 5.5. As expected, the peak membrane displacement increased linearly with increasing pulse pressure which could be represented by:

$$w = 3.09p_c - 0.93, R^2 = 0.97 \quad (5.2)$$

where p_c is the pulse pressure in the chamber. Our measurements led to a correlation coefficient at 3.09, compared to the reported 3.84 in our colleague's work [136]. This difference is due to the previous use of silicone cylindrical insert which reduced the internal chamber volume to accelerate the membrane displacement in the former report which was not utilized in the internal chamber during our tests.

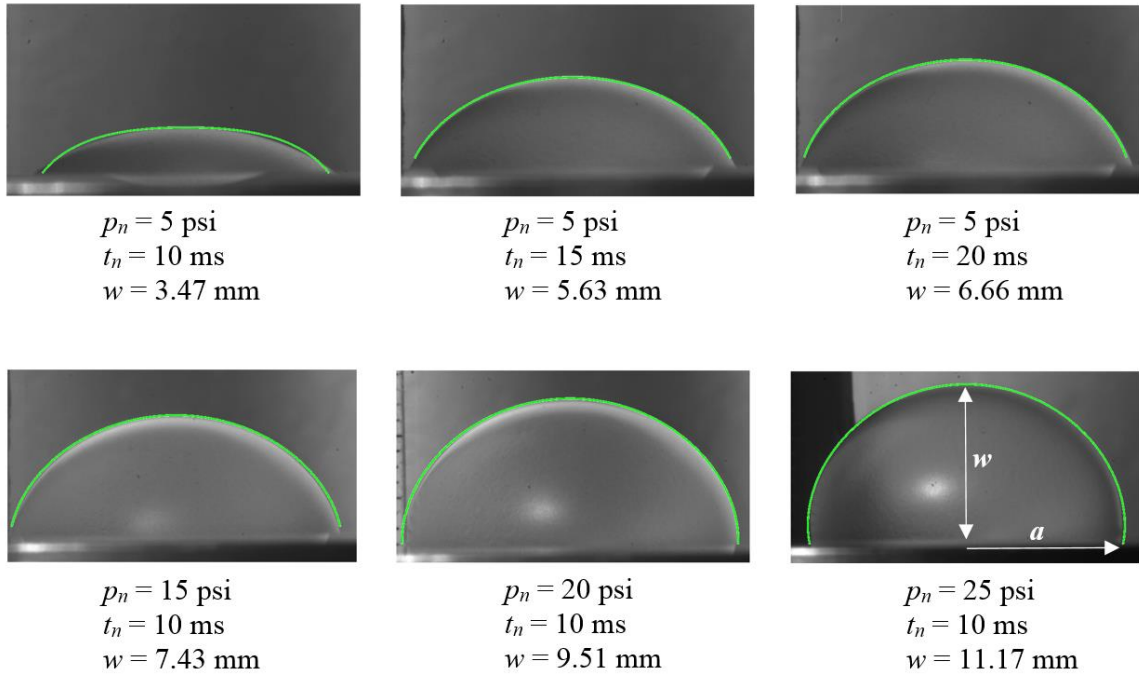


Figure 5.3: CAI device characterization. High-speed camera images were utilized to measure the peak membrane displacement, w , at various nominal pressure, p_n , and time, t_n . The green highlighted line shows comparison to the numerical simulation.

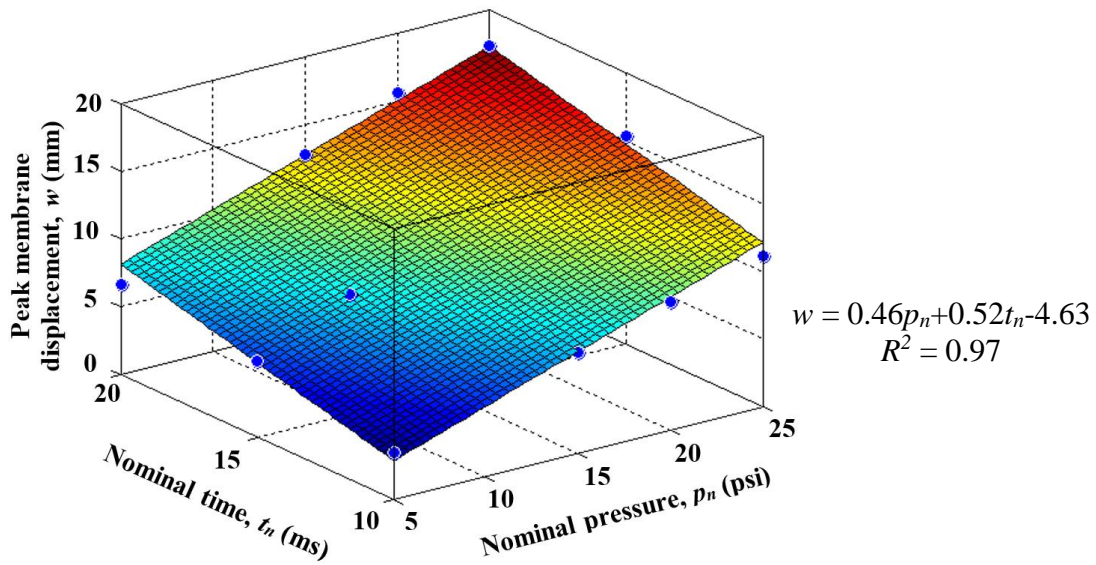


Figure 5.4: Three-dimensional response surface plot for Eq. (5.1) simulating the peak membrane displacement as a function of nominal setting (time and pressure).

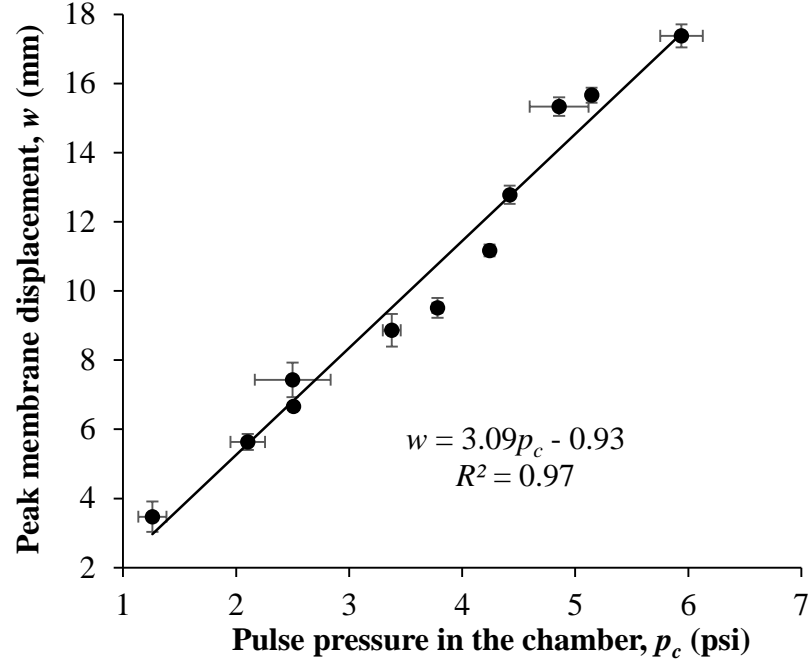


Figure 5.5: Relationship between the peak membrane displacement and the pulse pressure in the chamber.

5.3.2 Membrane Strain Analysis

Cell injury threshold is generally indexed as a function of membrane strain which has been calculated via a variety of methods usually correlating membrane displacement to percentage strain via theoretical or experimental models [21, 136, 139]. For this study we utilized a numerical simulation to calculate the strain on the membrane. The model was calibrated by the measured membrane contour at various nominal settings as shown in Figure 5.3, where the highlighted solid line represents the stretched membrane obtained from our simulation. It is clear that the simulated membrane profiles matched well with the high-speed camera images. This verified the robustness of our numerical framework, which could then be used to predict the membrane strain for each nominal setting, as listed in

Table 5.1. Figure 5.6 shows the comparison of our simulation predicted average membrane strain vs. results obtained from a frequently used theoretical equation [140]:

$$\varepsilon = \frac{2}{3} \left(\frac{w}{a} \right)^2 - \frac{2}{15} \left(\frac{w}{a} \right)^4 + \frac{2}{35} \left(\frac{w}{a} \right)^6 \quad (5.3)$$

where a is the radius of the membrane or the radius of the central circular hole in the stainless steel plate. It is observed that the membrane strain between theoretical derivation and our simulation matched very well as the peak membrane displacement is less than 7.43 mm. However, for large membrane deformations ($w > 7.43$ mm) the theoretical equation did not fit well with both simulation and experimental results (Figure 5.6) resulting in much larger membrane strain predictions from the theoretical equation calculated compared to the simulation. This could be a result of simplifications in the theoretical derivation as it did not consider the bending moment of the membrane, which was captured in our simulation as well as experiments. Therefore, an empirical displacement-strain relationship was developed to calculate membrane strain at large membrane displacements:

$$\varepsilon = 0.11w^2 + 3.24w - 4.67, \quad R^2 = 0.99 \quad (5.4)$$

Hereafter, we utilize a combination of Eqs. (4) & (1) to report the results in terms of average membrane strain. The calibrations we have just described provide CAI device users with a more accurate method of computing the strain in the membrane to which the astrocytes are subjected.

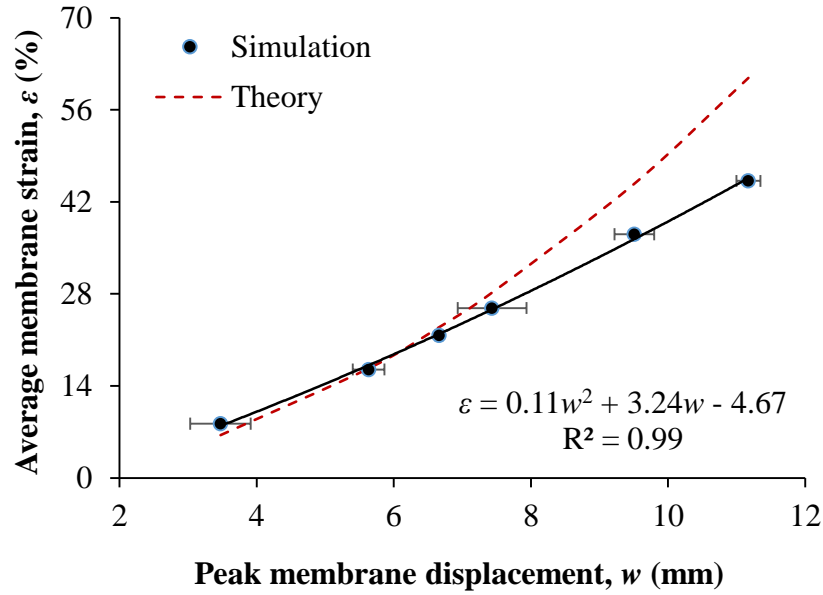
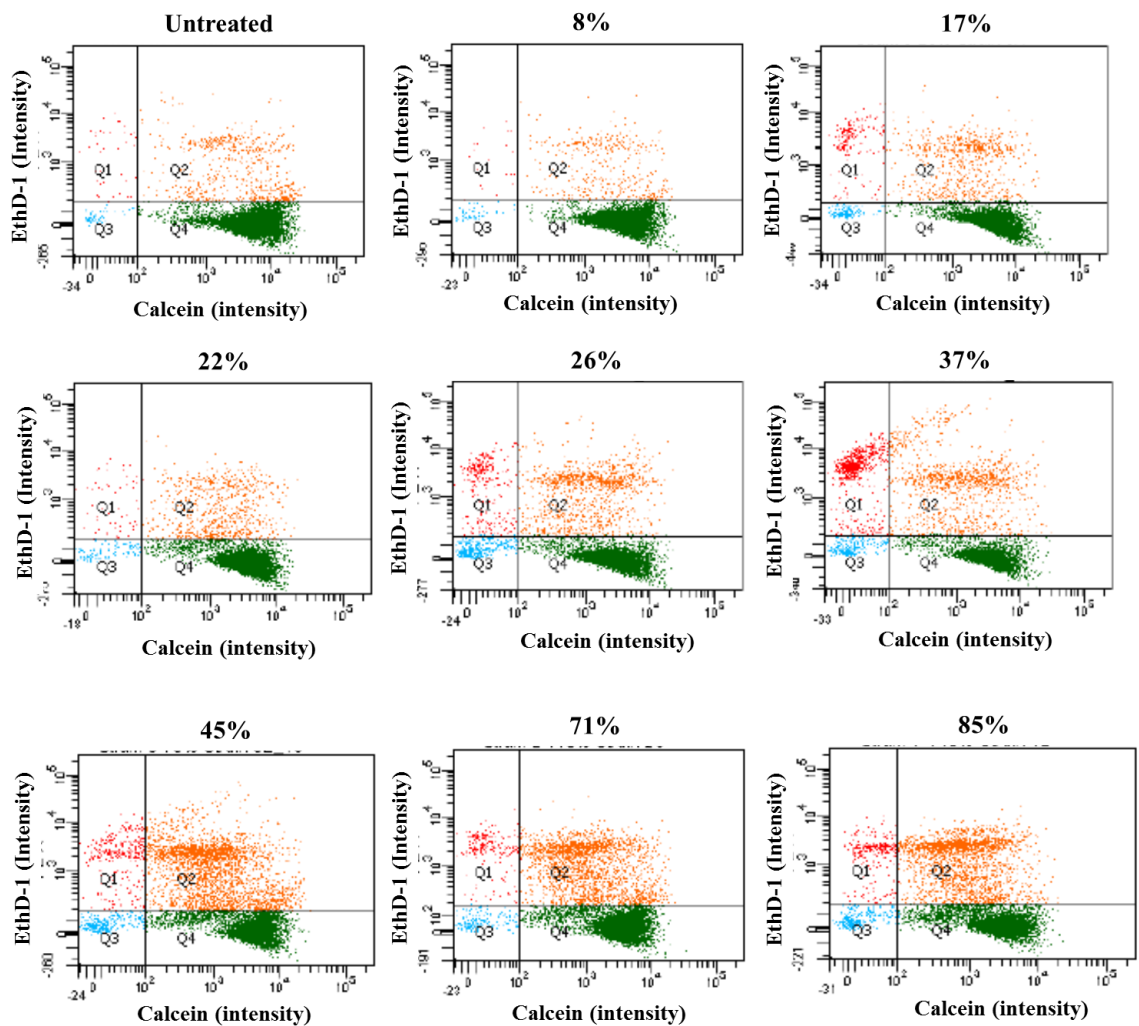


Figure 5.6: Relationship between the average membrane strain and the peak membrane displacement.

5.3.3 Cell Response to Increasing Membrane Strain

The injury initiated by membrane strain was determined by Live/Dead assay and flow cytometry (Figure 5.7). Astrocytes were subjected to increasing levels of membrane strain resulting in each population containing live, dead and “injured cells”. Injured cells are defined as cells being stained with both Ethd-1 and calcein indicative of membrane injury which did not result in cell death. Astrocytes were found to be resilient at strains $< 22\%$ as the viability and percentage of injured population remained relatively stable and there was insignificant deviation from naïve astrocytes. At strains $> 26\%$ there was a strain-dependent decrease in the live population (81, 68, and 69% of the population at 26, 37 and 45% strain ($p < 0.001$), respectively) as well as increase in injured (14, 19, 28% of population for 26, 37 ($p < 0.05$) and 45% strain ($p < 0.001$), respectively) and dead populations (12% of population for 37 % membrane strain, respectively ($p < 0.05$)). Although the range of strains

utilized for cell injury never resulted in a larger population of injured astrocytes than healthy astrocytes the cell populations appeared to trend toward a plateau with live cells approximately 65% of the population and injured cells approximately 28% of the population indicating that larger membrane strain would be required for further descent in viability; however, due to instrument constraints we were unable to achieve higher membrane strains.



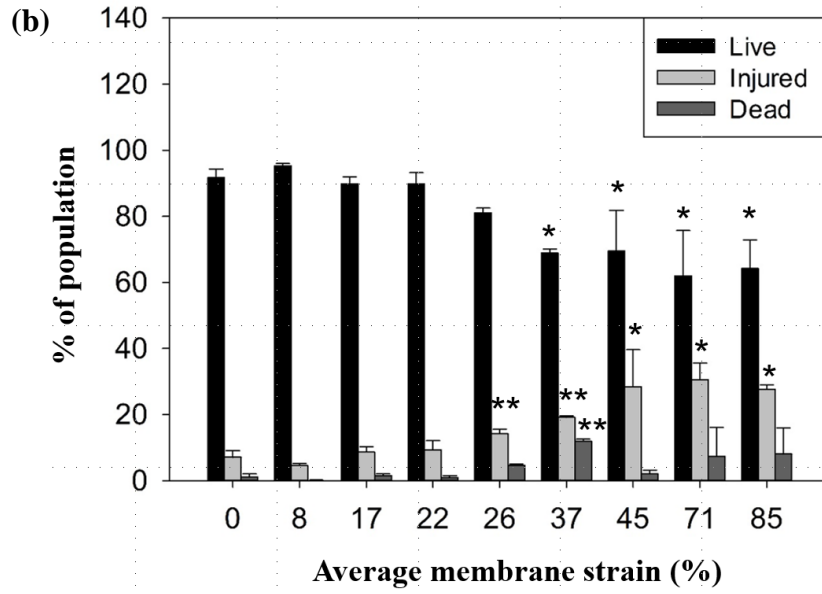


Figure 5.7: Cell injury was determined by Ethd-calcein staining and quantified with flow cytometry (FC). Representative FC results (a) show the distribution of dead (Q1), injured (Q2), and live (Q4) cells based on intensity of staining with Ethd-1 and calcein immediately after injury ($t = 0$) with increasing average membrane strain from 0-90% strain. The quantification of live, injured and dead are presented as a % of the population of total stained cells (b) $n = 3$, “**” $P < 0.001$ vs the naïve cells, “***” $P < 0.05$ vs naïve cells.

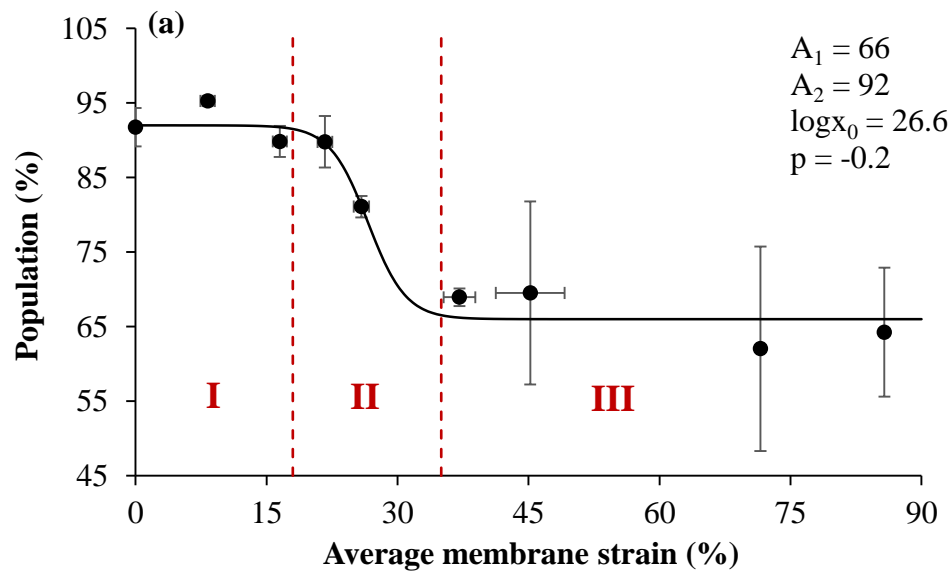
5.3.4 Injury Profiles of Astrocytes

The cell response, i.e., live and injured populations were related to average membrane strain (Figure 5.8) using an exposure-response curve [136]:

$$y = A_1 + \frac{A_2 - A_1}{1 + 10^{(\log x_0 - x)p}} \quad (5)$$

where $\log(x_0)$ is the center of the curve, p is the hill slope, and A_1 and A_2 are the bottom and top asymptotes, respectively. The resulting exposure-response curves fitted to

experimental data for membrane strain up to 85% are depicted in Figure 5.8. Both plots present complementary data in that the population of live astrocytes decreased sharply in the narrow strain range ($\epsilon = 18\text{-}35\%$) with corresponding increase in injured astrocyte numbers. From these results, we identified three regions with different modes of injury: (I) a mild injury region, with predominantly live astrocytes ($\epsilon = 0\text{-}18\%$), (II) a moderate injury region transitioning from predominantly live astrocytes to significantly increased population of injured astrocytes with a steep increase in injury resulting from slight increase in strain ($\epsilon = 18\text{-}35\%$), and (III) a severe injury region which resulted in constant significant injury in astrocytes ($\epsilon > 35\%$). Observing the response curves allows the identification of the injury threshold for astrocytes, or the range of membrane strain during which small increases in membrane strain result in substantial cell injury, at 18-35% membrane strain.



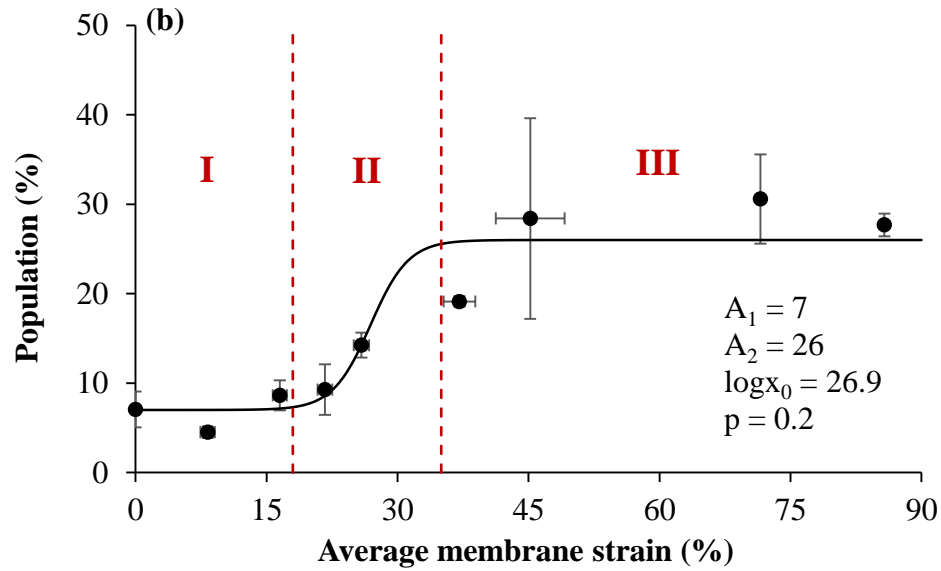


Figure 5.8: Injury profile of astrocytes with increasing average membrane strain. % of population of live (a) and injured cells (b) after membrane stretch of 0-90% strain.

The identified astrocyte injury threshold at strain levels of 18-35% (corresponding peak membrane displacement of approximately 5.82-9.26 mm) agreed well with the injury threshold identified by Ellis et al. [21]. They developed a similar *in vitro* device to examine the morphologic consequences of stretch-induced injury on rat cortical astrocytes. The membrane strain of 31% in our study (peak membrane displacement of approximately 8.50 mm) was considered as the upper limit of astrocyte injury threshold. Although Ellis et al did not calculate an astrocyte injury threshold they similarly saw that just after cell injury (within 10 minutes) lactate dehydrogenase (LDH) release in the media, considered a standard assay of membrane integrity and viability, is severely increased with a peak membrane displacement of 8.6 mm (72% membrane strain by their calculations) compared to naïve cells whereas there was not a significant difference in LDH release after 5.7 mm peak displacement (31% membrane strain by their calculations). This indicates a region of rapid increase in injury between these peak displacements to our astrocyte threshold while

the percentage membrane strain range is different. This difference could be attributed to both the setup of devices and the strain estimation equation. Their device delivered a pulse pressure directly towards the center of the membrane, and ours had a side opening. This difference might cause a relatively smaller peak membrane displacement from our device. In addition, we have demonstrated earlier that the membrane strain calculated from Eq. (3) might be overestimated at large membrane displacements.

It should be noted that the obtained astrocyte injury threshold at 18-35% strain is less than the reported threshold for human neuroblastoma SH-SY5Y cells, at 30-55% strain (peak membrane displacement approximately 7.1-10.7 mm) [136]. This implies that neurons are much less vulnerable to biaxial stretch than astrocytes which could have origins in fundamental differences in cell shape and attachment tendencies. Traditionally neurons are asymmetric with a body, dendrites and neurites resulting in a long cell which predominantly spreads in one direction where astrocytes are star-like and largely symmetric in shape therefore neurons may experience biaxial stretch primarily as unidirectional. This appears an unlikely scenario as Geddes-Klein et al compared neuronal cell damage after uniaxial and biaxial membrane strain noting that for stretch magnitudes of 10, 30, and 50% there were significant differences in intercellular calcium reaction between the uniaxial and biaxial stretch events suggesting that neurons are sensitive to biaxial stretch despite the directionality of their shape [141]. Another more likely explanation for greater astrocyte sensitivity to stretch injury is the degree to which the cell types attach to the culture membrane. Neurons are traditionally difficult to culture *in vitro* without culture plate coatings, such as PLL or Laminin, and typically have superior growth on a layer of glial cells [133, 142]. Astrocytes, on the other hand, with their increased cell

body size and number of processes do not require such precautions. This difference in attachment ability has previously been speculated to increase astrocyte sensitivity to the mechanical properties of culture surface which could also explain the robustness of the neurons in this scenario [143].

5.4 Conclusions

In this study we characterized a previously developed CCI device with finite element modeling combined with high-speed imaging to correlate the peak membrane displacement with the average membrane strain. We were able to account for three dimensional membrane deformation not considered in previous theoretical and experimental models, which resulted in lower membrane strains at large membrane deformation. Furthermore, we utilized the CCI device to profile astrocyte injury observing an injury threshold between 18-35% corresponding to mild strains observed in animal TBI models. Astrocytes show a decreasing level of actin organization with increasing average membrane strain suggesting that traumatic injury may disrupt cytoskeletal filaments which could have implications toward astrogliosis initiation and sustainability. Further study is needed to characterize the molecular pathways of the astrogliotic phenotype initiated by TBI. The observations of this work show that our CCI device would be a useful model for furthering knowledge of astrocyte role in TBI detection, progression and treatment.

Chapter 6

Characterization of Closed Head Impact Injury in Rat

6.1 Introduction

Traumatic brain injury (TBI) is the leading cause of mortality and morbidity in the United States, which affects over 1.7 million Americans each year [144]. It leads to long-term disability in cognition, sensorimotor function, and personality [84, 145]. To study the mechanisms of TBI, the rat closed head impact (CHI) is commonly used for replicating the trauma events [146-152]. In a typical CHI procedure, the rat is fully anesthetized and secured in a stereotactic frame. An impact load is delivered directly to the intact skull through a pneumatically-driven impactor. Compared with other animal models such as fluid percussion [153] and controlled cortical impact (CCI) [154], the CHI model avoided performing the craniotomy and thus the risk of operation-induced inflammation. The CHI model has been used for investigating the cortical tissue loss [146, 147], acute subarachnoid hemorrhage [148], diffuse axonal injury [149], blood-brain barrier dysfunction [150, 151], and concussion [152]. Nevertheless, various control parameters (e.g., impact depth, velocity, and position; impactor diameter, material, and shape) were employed by different

research groups, making it hard to compare these results. In addition, the internal brain response variables could be documented in more detail. To address these shortcomings, it is crucial to establish the linkage between external impact parameters and intracranial responses.

In this work, the sensitivities of intracranial responses to various impact parameters in the CHI model were systematically investigated. A three-dimensional (3D) finite element (FE) rat head model with anatomical details was developed from medical images. An orthogonal experimental design was implemented for carrying out eight computational experiments to correlate the regional brain mechanics with impact controls including impact depth, velocity, and position, as well as impactor diameter, material, and shape.

6.2 Materials and Methods

6.2.1 Finite Element Modeling

A 3D FE rat head model was generated from the high-resolution magnetic resonance imaging (MRI) datasets of an adult male Sprague-Dawley rat weighing about 360 g, as shown in Figure 6.1. The brain MRI has an isotropic resolution of $256 \times 256 \times 256$ pixels, for a field view of 30 mm in all three directions. The image data were segmented into three main brain regions; cerebrum, hippocampus, and cerebellum. The segmentation was realized using the 3D image analysis algorithm implemented in Mimics[®] (Materialise, Inc., Leuven, Belgium). The segmented brain model was then imported into HyperMesh[®] (Altair Engineering, Inc., MI, USA) and meshed as a triangular surface mesh (S3R). A volume mesh with 4-noded tetrahedral elements (C3D4) was generated from this surface mesh. The rat skull was created by offsetting a layer of wedge elements (C3D6) above the

outer surface of the brain by 0.16 mm [155]. A mesh convergence test was conducted and the minimum mesh size of 0.4 mm was chosen. At this resolution, the rat head model consisted of a total of 1,107,183 tetrahedral elements and 14,898 prism elements for the brain and skull, respectively.

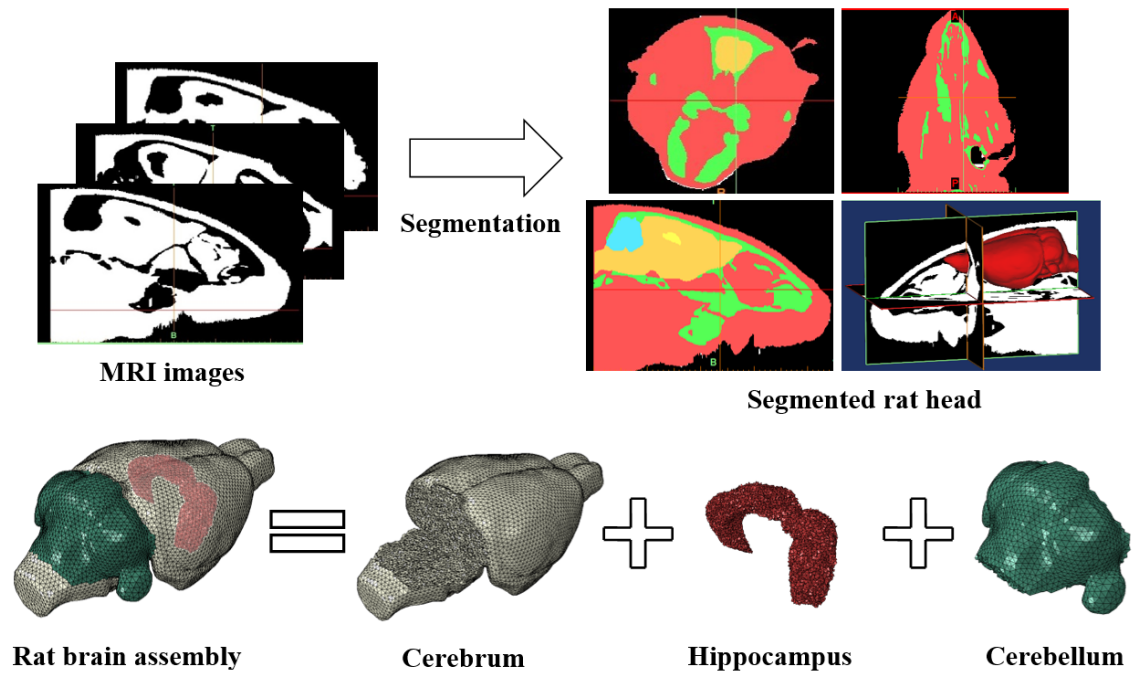


Figure 6.1: Finite element discretization of the adult male Sprague-Dawley rat head.

The rat brain was assumed to be a linear viscoelastic material with a decay constant of 20 ms [156]. For the cerebrum, a short-term shear modulus of 1.72 kPa and a long-term shear modulus of 0.51 kPa were assumed. This assumption was based on the indentation test results obtained from the adult rat brain as reported by Gefen et al. [157]. The cerebellum had a short-term modulus of 1.2 kPa and a long-term modulus of 0.36 kPa, while the same parameters for the hippocampus were 4.06 kPa and 0.61 kPa, respectively [158]. The rat skull was modeled as a homogeneous linear elastic isotropic material and

the Young's modulus and Poisson's ratio were assumed as 6 GPa and 0.3, respectively [159]. A summarization of the material properties is described in Table 6.1.

Table 6.1: Material properties of the rat head components.

(a) Elastic material properties				
Component	Density (kg/m ³)	Young's modulus (MPa)	Poisson's ratio (/)	
Skull	1710	6000	0.3	
(b) Viscoelastic material properties				
Component	Density (kg/m ³)	Short-term shear modulus (kPa)	Long-term shear modulus (kPa)	Decay constant (ms)
Cerebrum	1040	1.72	0.51	20
Cerebellum	1040	1.20	0.36	20
Hippocampus	1040	4.06	0.61	20

To replicate the experimental CHI procedure, a cylindrical impactor, which connected to the bottom surface of a steel rod was positioned perpendicular to the dorsal surface of the rat skull (Figure 6.2). A linearly ramping displacement was enforced onto the steel rod to achieve the prescribed impact depth and velocity. Due to variations in impactor geometries, materials and positions, the prescribed conditions will result in different indentation behaviors. The interactions between the impactor and skull as well as between the brain and skull were modeled through penalty contact algorithm with tangential sliding and hard contact normal behavior. The nodes on the bottom surface of the skull were constrained in all six degrees of freedom to avoid rigid body translation. The FE model

was solved using the nonlinear transient dynamic procedure Abaqus/Explicit (Dassault Systems Simulia Corp., RI, USA).

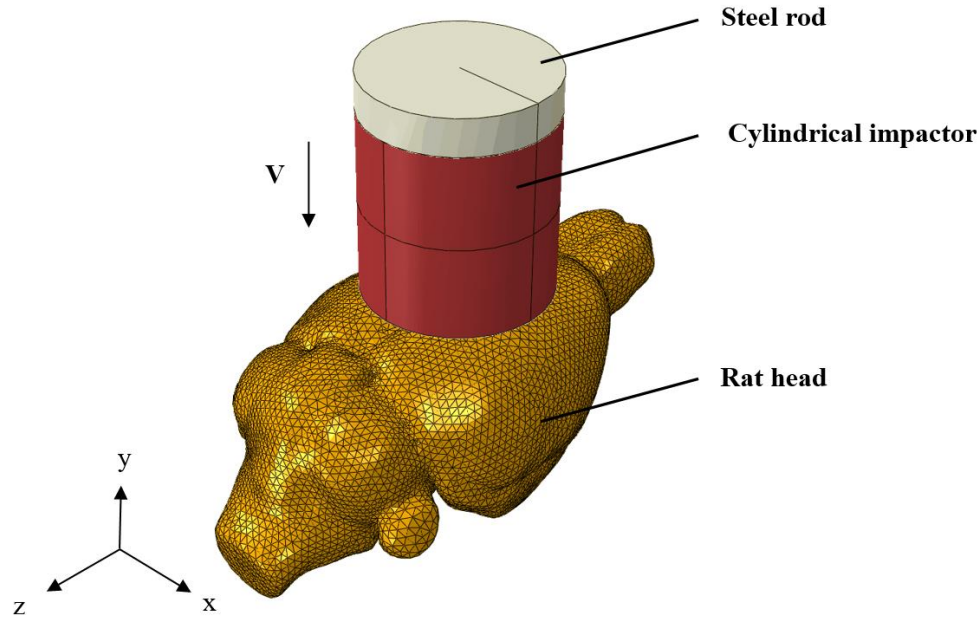


Figure 6.2: Isometric view of the closed head impact model.

6.2.2 Design of Computational Experiments

A six-factor two-level orthogonal experimental design was implemented to systematically investigate the sensitivities of intracranial responses to various impact parameters in three different brain regions; cerebrum, hippocampus, and cerebellum. The six factors studied were the prescribed impact depth (A), velocity (B), and position (C), as well as impactor diameter (D), material (E), and shape (F). The baseline level of these factors was selected from the typical CHI procedures, including an impact depth of 1 mm, velocity of 3 m/s, central position around the midline between bregma and lambda, nylon impactor with a diameter of 6 mm and a flat end. The second level of the quantitative factors, i.e., impact depth, velocity, and impactor diameter, was double over the baseline. For the qualitative

factors, the second level was selected as lateral impact position over the left parietal bone between bregma and lambda, steel impactor material, and convex end. An $L_8(2)^7$ orthogonal array from the module of Statistica (Version 10.0) was adopted to implement the multifactor combination. The assignment of six factors and their selected levels in the array was depicted in Table 6.2.

Table 6.2: Assignment of six factors and their selected levels in the orthogonal array.

Case No.	Factors					
	A	B	C	D	E	F
1	1	3	Central	6	Steel	Flat
2	1	3	Lateral	6	Nylon	Convex
3	1	6	Central	12	Steel	Convex
4	1	6	Lateral	12	Nylon	Flat
5	2	3	Central	12	Nylon	Flat
6	2	3	Lateral	12	Steel	Convex
7	2	6	Central	6	Nylon	Convex
8	2	6	Lateral	6	Steel	Flat

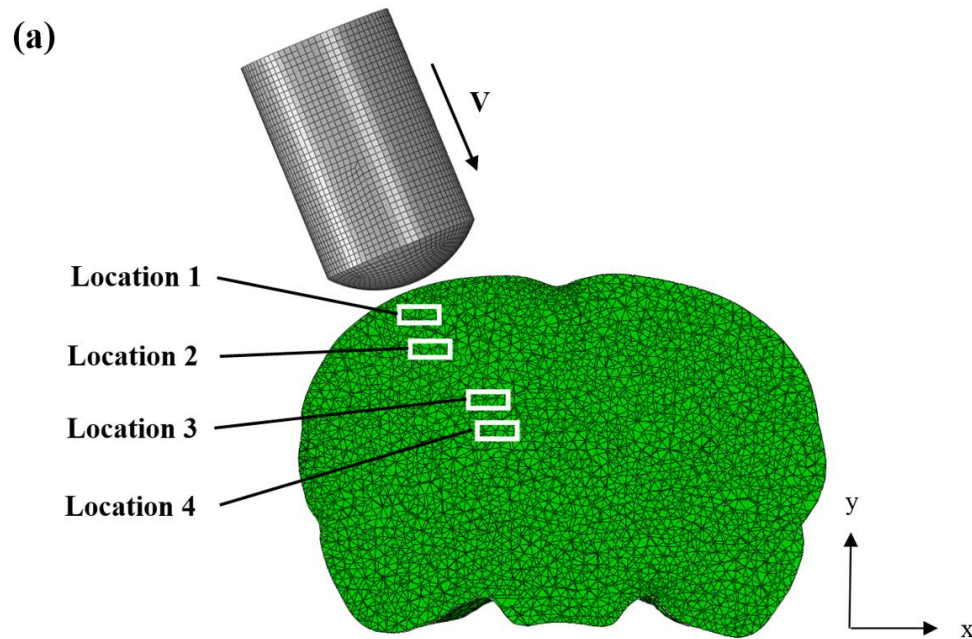
6.3 Results

6.3.1 Model Verification

The published CCI injury data [156] were used to verify the FE model. To simulate the cortical impact, a 7-mm-diameter craniotomy was created on the left skull. The impactor shape and impact direction were accurately defined according to the settings in the cited publication. The relative position between the impactor and brain is shown in Figure 6.3

(a). The impact depth and velocity were assumed to be 1.5 mm and 4 m/s, respectively. The peak maximum principal strain (MPS) was extracted at four different locations of the brain (Figure 6.3 (a), locations 1-4), corresponding to the superior cortex, deep cortex, hippocampus, and thalamus as measured in reference [156].

Comparative results are shown in Figure 6.3 (b). The peak MPS predicted by the FE model agreed well with the published data. The maximum deviation between the FE model and reference [156] was 23.8% at location 4, while the deviations at other locations were less than 9.0%. Moreover, in the FE model, location 2 experienced 13.0% higher peak MPS than location 1 although location 1 was more close to the impact site. This was consistent with the finding in reference [156], which measured a 17.4% higher peak MPS at deep cortex compared to the superior cortex.



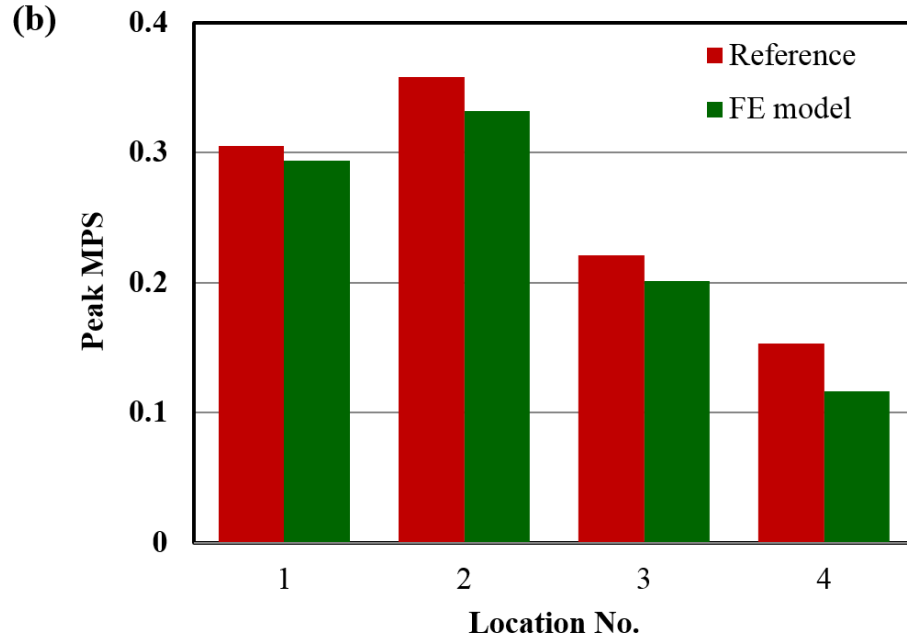


Figure 6.3: Verification of rat head model with reference [156]. (a) Coronal view of rat head subjected to controlled cortical impact, (b) peak MPS comparisons at four different locations of the brain.

6.3.2 Sensitivity Studies

The predicted MPS was used to characterize the brain responses. The peak MPS in the cerebrum, hippocampus, and cerebellum for all eight cases are listed in Table 6.3. The range analysis, which assumes that the influence of other factors on the result is balanced when analyzing the impact of a specific factor, was performed to quantify the significance levels of each factor as shown in Table 6.4. The K_i value of a factor was the average of four values of peak MPS for level i listed in Table 6.2, and the range value R for each factor was the difference between K_i values of the two levels. A larger R indicates that the corresponding factor plays a more important role in the brain responses. The Pareto chart (Figure 6.4), based on the magnitude of range value R , has shown that impact depth and

impactor shape were the two leading factors affecting biomechanical responses of the brain regardless of regions. For example, varying the impact depth from 1 mm to 2 mm produced an increase of peak MPS in the cerebrum of 0.1941, in the hippocampus of 0.1514, and in the cerebellum of 0.1595. As a flat impactor was changed to a convex one, the peak MPS decreased 0.1473, 0.1102, and 0.1386 in the cerebrum, hippocampus, and cerebellum, respectively. Moreover, the high strains induced by the flat impactor were approximately parallel to the bottom rim of the impactor, while those induced by the convex one were concentrated along the axial line (Figure 6.5, cases 1 and 7).

Table 6.3: Predicted peak maximum principal strain (MPS) in the cerebrum, hippocampus, and cerebellum.

Case No.	Predicted peak MPS		
	Cerebrum	Hippocampus	Cerebellum
1	0.1775	0.1466	0.1535
2	0.2283	0.1593	0.0326
3	0.2061	0.0912	0.0494
4	0.4080	0.2993	0.1261
5	0.6192	0.3644	0.3890
6	0.3744	0.3080	0.1238
7	0.3047	0.2204	0.1976
8	0.4982	0.4092	0.2893

Table 6.4: Range analysis for the peak maximum principal strain (MPS) in the cerebrum, hippocampus, and cerebellum.

Factors	A	B	C	D	E	F
Cerebrum						
K_1	0.2550	0.3499	0.3269	0.3022	0.3141	0.4257
K_2	0.4491	0.3543	0.3772	0.4019	0.3901	0.2784
R	0.1941	0.0044	0.0503	0.0997	0.0760	0.1473
Hippocampus						
K_1	0.1741	0.2446	0.2057	0.2339	0.2388	0.3049
K_2	0.3255	0.2550	0.2940	0.2657	0.2609	0.1947
R	0.1514	0.0104	0.0883	0.0318	0.0221	0.1102
Cerebellum						
K_1	0.0904	0.1747	0.1974	0.1683	0.1540	0.2395
K_2	0.2499	0.1656	0.1430	0.1721	0.1863	0.1009
R	0.1595	0.0091	0.0544	0.0038	0.0323	0.1386

A (impact depth), B (impact velocity), C (impact position), D (impactor diameter), E (impactor material), F (impactor shape).

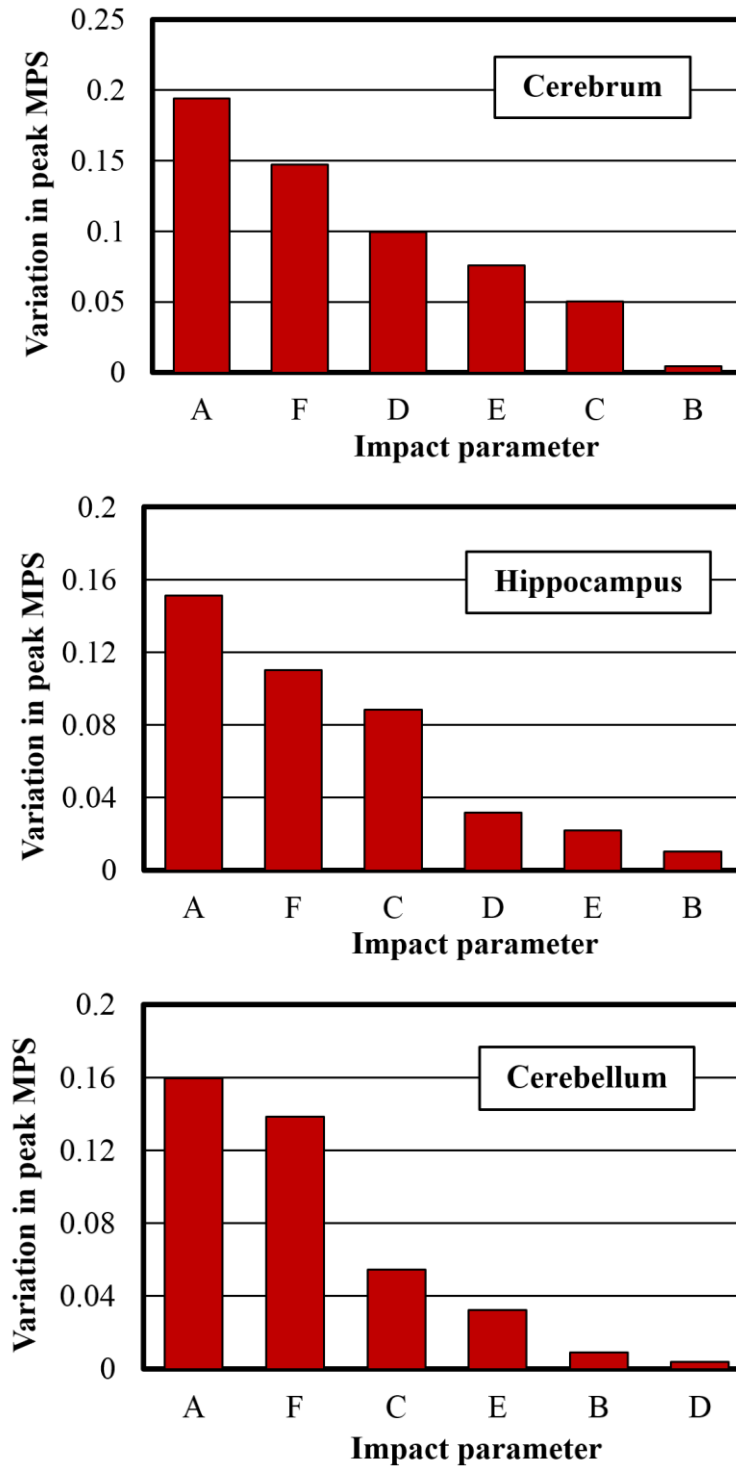


Figure 6.4: Pareto chart of region-specific biomechanical responses to external impact parameters. A: impact depth; B: impact velocity; C: impact position; D: impactor diameter; E: impactor material; F: impactor shape.

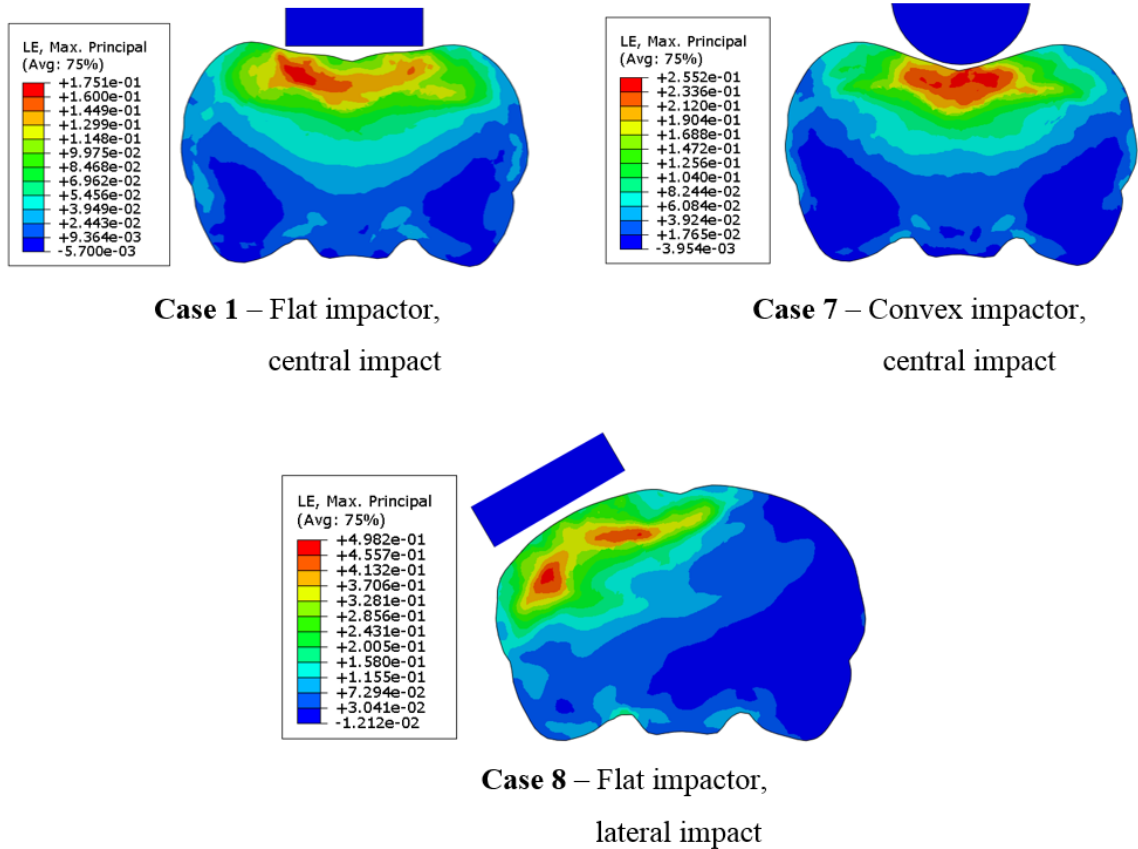


Figure 6.5: Contour plots of maximum principal strain on a coronal plane of the rat brain.

Following impact depth and impactor shape, impactor diameter ranked as the third most important factor for the calculated peak MPS in the cerebrum. However, impactor diameter had much less effect in the hippocampus and cerebellum. For example, the peak MPS in the cerebrum increased 0.0997 when impactor diameter increased from 6 mm to 12 mm, compared to a limited increase of 0.0318 and 0.0038 in the hippocampus and cerebellum, respectively.

Impact position seems to have a uniform effect on the biomechanical responses in all three brain regions. Changing the impact position from central to lateral, the peak MPS in the cerebrum, hippocampus, and cerebellum increased 0.06 ± 0.02 . A coronal view of the rat brain exhibited totally different strain patterns when the impact position was changed

(Figure 6.5, cases 1 and 8). It is observed that a lateral impact induced higher MPS to the ipsilateral side of the brain and the strain magnitude in most region of the contralateral side was almost zero. In contrast, a similar strain gradient was found on both sides of the brain for the central impact.

Only small variations were found due to variations in impact velocity and impactor material on the predicted peak MPS in all three brain regions. Since impact depth, impactor shape, impactor diameter, and impact position could affect the intracranial responses both qualitatively and quantitatively, they are most critical when designing appropriate CHI models.

6.4 Discussion

In this work, the sensitivities of intracranial responses to various impact parameters in the CHI model were systematically investigated using the 3D FE rat head model. The peak MPS was chosen as the response variable since previous investigations have demonstrated that regions with higher MPS correlated well with the brain injury severity including contusion volumes and the percentage of neuronal cell loss [160]. Our model was first verified by previously published CCI injury data [156] and good agreement has been achieved (Figure 6.3). It is observed that the peak MPS predicted by the FE model was generally lower than the published results. This could be attributed to the difference in weight and size of the rat which we used. The anatomy and geometry of the brain used in this work was taken from the rat weighing about 360 g, which was larger than that of 250 – 300 g in reference [156]. Previous study has demonstrated that increasing the size of rat brain would decrease the magnitude of predicted strain under impact loading [161].

Following model verification, an orthogonal experimental design was then used to quantify the significance levels of six impact parameters on the brain response. Our results (Figure 6.4) have shown that the prescribed impact depth is the leading factor affecting intracranial MPS responses in CHI. A larger impact depth could result in more severe axonal damage as well as increased permeability of the blood-brain barrier in the rat brain [150, 155]. This reinforced our finding that the intracranial peak MPS might serve as an index for the brain injury severity. On the contrary, the impact depth itself is not a reliable index based on observations that the impact-induced peak brain MPS could vary 103.2% in the cerebrum, 85.7% in the hippocampus, and 214.2% in the cerebellum under the same prescribed impact depth at 2 mm.

Under the same boundary constraints, the convex impactor reduced the intracranial peak MPS compared to the flat one, i.e., $K_2 < K_1$ (column F in Table 6.4). However, it induced strain concentration within the brain (Figure 6.5, cases 1 and 7), associated with the severity of TBI, and a stress concentration in the skull, leading to higher incidence of skull fracture (Figure 6.6). This is why flat impactors were commonly used in documented studies to induce the diffuse injury within the brain as well as to reduce the skull fracture [146, 148-150, 152]. In addition, the impactor diameter in the CHI tests is generally larger than 6 mm [146, 149, 150, 152], whereas it is less than 5 mm in the CCI tests [154]. An increase in impactor diameter could substantially increase tissue strains in the cerebrum, located directly beneath the impactor; however, the strains in the hippocampus and cerebellum seem to be not sensitive to this impact parameter.

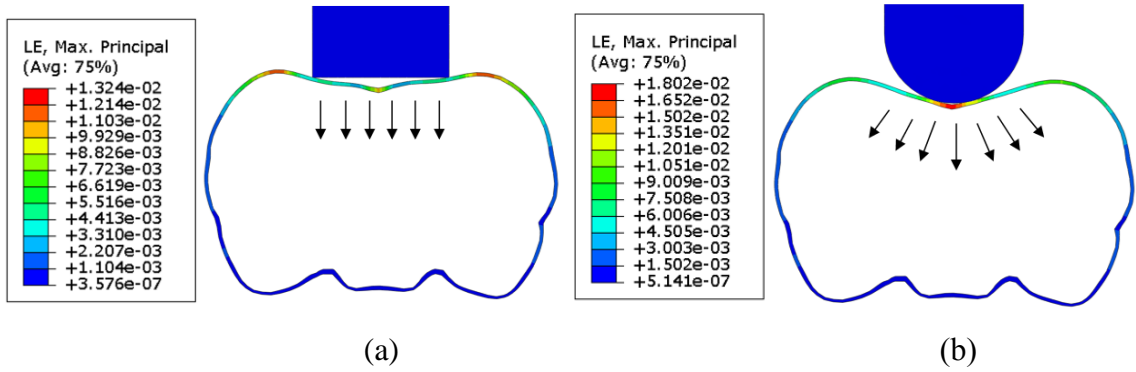


Figure 6.6: A coronal view of skull deformation for (a) flat and (b) convex impactor.

Impact position is found to be crucial in determining the extent and location of tissue injury in rat brain. Our results (Table 6.4) show that lateral impact induced higher peak MPS in all three brain regions compared to the central impact. Moreover, the high strains induced by the lateral impact were mainly focused on the ipsilateral side of the brain, while those induced by the central impact were more diffusely located on both sides (Figure 6.5, cases 1 and 8). This is consistent with the clinical observation that lateral impact inflicts primarily unilateral cortical damage, whereas central impact causes bilateral cortical alterations [146, 150]. Furthermore, the lateral impact is able to induce a larger relative movement between the brain and skull, which contributes to the subarachnoid hemorrhage (SAH), a common cerebrovascular event following CHI [148, 149]. The relative displacement at five marked locations (M1 – M5) along the brain/skull interface was compared between central and lateral impacts (Figure 6.7). The maximum relative displacement was 0.43 mm at location M1 subjected to lateral impact, and 0.20 mm at location M2 subjected to central impact. This indicates that SAH is more likely to occur on the ipsilateral side of the brain. However, the relative displacement induced by the lateral impact was minimal at location M2. This is due that this location is along the midline of the lateral impactor, which constrained the relative motion between the brain and skull. A

similar observation existed at location M3, along the midline of the central impactor, which limited the relative skull/brain displacement. This implies that a properly designed impact position is able to guide SAH to target a specific region of interest.

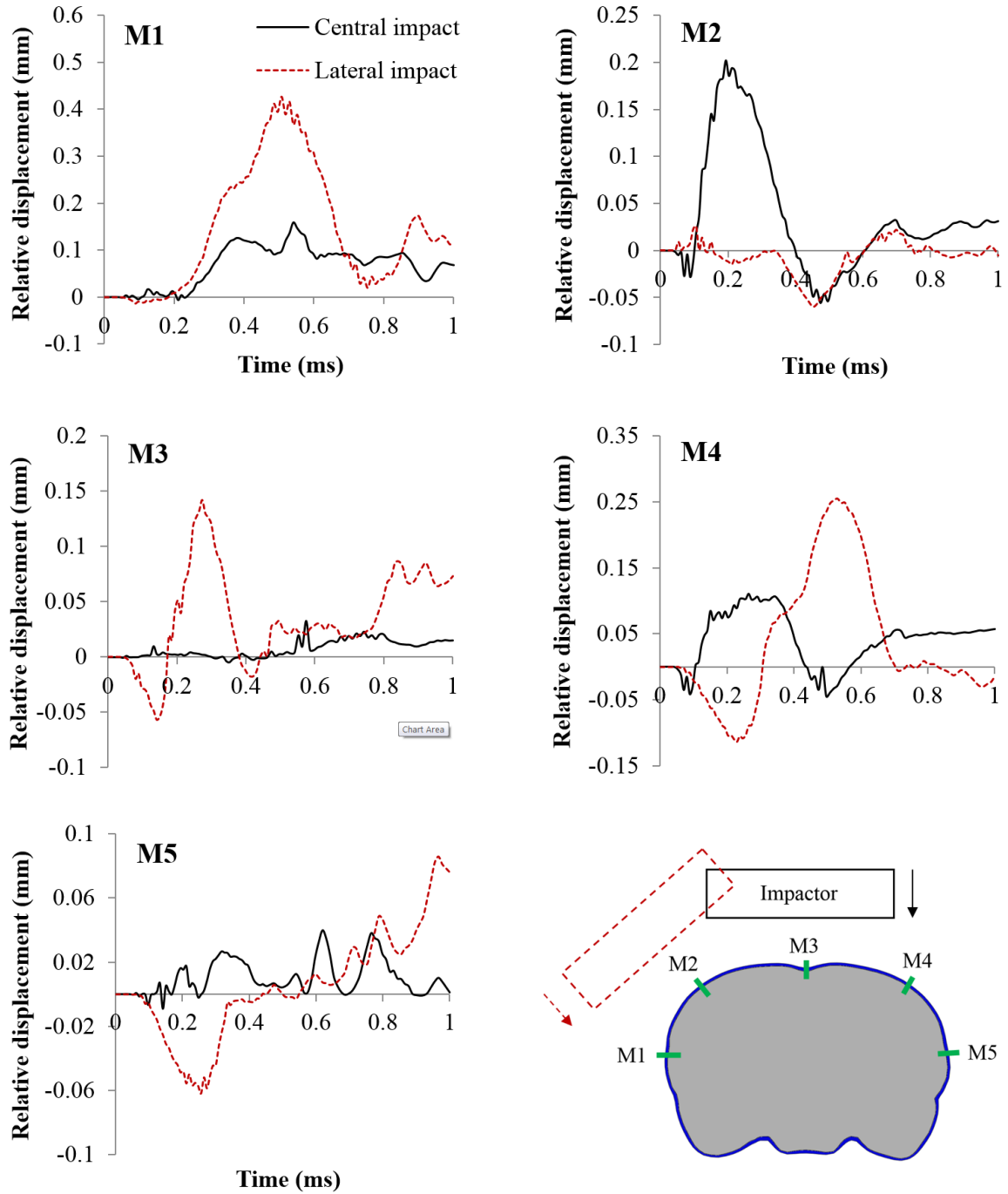


Figure 6.7: Relative displacement at five mark locations along the brain/skull interface.

The effect of impactor material on the intracranial responses is found to be very limited. This indicates that the brain injury severity might not be sensitive to the impactor materials. However, a softer impactor is commonly recommended for the CHI to avoid skull fracture [146, 152]. To examine the significance of impactor materials on skull fracture using von Mises criteria, the peak von Mises stress in the rat skull were obtained for two impactor materials (e.g., steel and nylon). It is found that the peak stress decreased only by 1.87% when the impactor material changed from steel to nylon, indicating the almost same probability of skull fracture. Careful attention should be paid when the impactor is made of an extremely soft material such as rubber [147]. One more simulation was conducted using baseline data except the impactor materials. The rubber impactor-induced peak von Mises stress was 36.1% less than the steel one. It should be noted, though, that such reduction of skull stress is caused by the insufficiency of indentation depth. We measured a 1-mm shortening of the rubber impactor at the time of maximum indentation. This indicated that the actual indentation depth was 1-mm instead of the prescribed 2-mm impact depth, leaving the rat brain to be less injured. It is suggested to calibrate the prescribed impact depth or monitor the actual indentation depth when adopting a very soft impactor in the CHI tests.

It is interesting to find that variations in impact velocity induced only small variations on peak MPS in all three brain regions. On the other hand, a wide range of impact velocities are used in different laboratories with the goal to induce desired injury levels [149, 151]. This inconsistency could be attributed to the overshoot phenomenon which widely exists in the pneumatically-driven impact devices [162]. Overshoot is referred to as the maximum transient displacement of the impactor tip that exceeds the predefined impact depth. We

have captured the trajectory of the impactor tip of a commercially available pneumatic device TBI-0310 Impactor (Precision Systems and Instrumentation) using a high-speed camera (Photron SA 1.1). It was observed that overshoot was positively correlated with the impactor velocity. For a predefined impact depth of 3 mm, the device produced a 0.4 mm (13%) overshoot at an impact velocity of 2 m/s, while the overshoot was substantially increased to 1.5 mm (50%) at 5 m/s. This overshoot phenomenon is not considered in our computational models, which might underestimate the role of impact velocity. In addition, the rat skull was modeled as a uniform thin layer, rather than geometrical details such as varied thickness.

The brain tissue was simplified as an isotropic homogeneous material, rather than a site-dependent white and gray matter combination including a dense network of blood vessels, cellular structure or differing cell types such as glial cells which are highly responsive to brain injury [163, 164]. The exclusion of these elements might alter the magnitude of brain dynamics. Moreover, the rat brain was meshed using tetrahedral elements. Although this element type makes meshing complex geometries easier, it tends to exhibit a stiffer response when compared to quadrilateral or hexahedral meshes because of shear/volumetric locking. Despite these simplifications, the present work demonstrated the significance level of six input parameters in terms of the brain MPS, which may have significant clinical implications for brain injury. This work can be used to provide a fundamental understanding of the impact of CHI designs on the brain and to better design a site- and severity-specific rodent CHI model.

Chapter 7

Conclusions and Future Work

7.1 Conclusions

Blast-induced traumatic brain injury (TBI) is the most prevalent military injury during the conflicts in Iraq and Afghanistan. However, the mechanisms by which blasts result in brain damage remains in dispute. A comprehensive knowledge of the loading mechanics of brain tissues is crucial in understanding the pathophysiology of blast-induced TBI as well as in designing effective mitigation strategies. In this work, the blast wave-head interaction was investigated, under pure primary blast loading conditions on the surrogate head and the biofidelic human head, using an integrated experimental and numerical approach. In addition, an *in vitro* injury model for primary cortical astrocytes was developed to understand the effects of the biomechanical loading conditions at the cellular level. The major conclusions of this work are:

- When the blast wave encounters the head, the flow field around the head was not uniform. The geometry of the head and its orientation with respect to the blast governed the flow dynamics around the head, which in turn determine the spatial and temporal distribution of intracranial responses.

- The intracranial pressure in the anterior part of the brain was dominated by the direct blast wave transmission, while in the posterior part it was attributed to both direct blast wave transmission and skull flexure, which took at a later time.
- Blood vessel networks significantly affected brain responses. The increased maximum principal strain (MPS) and shear strain (SS) were observed within the brain embedded with vessel networks, which did not exist in the case without blood vessel networks. Moreover, the vessel diameter and density also affected brain dynamics in both MPS and SS measures.
- Three different regions were identified in the stretch-induced dose-response curves of primary cortical astrocytes, with a very sharp decline from live to dead in a narrow range of strain (18-35%). This strain level was then identified as the injury threshold for astrocytes.
- Impact depth and impactor shape were the two leading factors affecting intracranial responses. The influence of impactor diameter was region-specific and an increase in impactor diameter could substantially increase tissue strains in the region which located directly beneath the impactor. The lateral impact could induce higher strains in the brain than the central impact. An indentation depth instead of impact depth would be appropriate to characterize the influence of a large deformed rubber impactor.

7.2 Future Work

The current work is based on a comprehensive computational framework for modeling the blast response of the brain. Although this framework includes accurate blast initialization and fluid-structure interaction algorithms, an experimentally-validated surrogate head model, and a 3D biofidelic human head model, there are a number of features that could be added to further enhance its accuracy:

First, we presented a validation effort that compared simulation results with data from blast experiments on the surrogate head. Although the comparison provided a level of validation sufficient for the purposes of this thesis, additional work is needed to further reduce discrepancies between experimental and numerical results. For example, improvements could be made by increasing the level of detail in computational models and engaging in additional efforts to quantify and reduce the uncertainty in the models and experiments.

Second, only the positive phase of the blast wave was considered. However, the negative phase is also important and need to be studied. It is hypothesized that the negative phase or the negative overpressure may be responsible for cavitation in the brain, which is an important injury mechanism that has to be studied.

Third, the intracranial pressure was only correlated with direct blast wave transmission and skull flexure. Other injury mechanisms such as cavitation, thoracic surge, and injuries due to acceleration/deceleration have to be studied to obtain comprehensive understanding of the blast.

Finally, the skull was simply assumed as linear elastic material. Considering the critical role of the skull in protecting the intracranial cavity, an enhanced constitutive model for

the skull could allow simulations to better describe the blast response of the head. This is similar to the brain tissues. More accurate mechanical characterization of the brain could be carried out by conducting *in vitro* static indentation and stress relaxation tests using atomic force microscopy.

References

1. Sweden, C., *Shell shock revisited: solving the puzzle of blast trauma*. 2008.
2. Warden, D., et al. *War neurotrauma: The defense and veterans brain injury center (DVBIC) experience at Walter Reed Army Medical Center (WRAMC)*. in *Journal of Neurotrauma*. 2005. MARY ANN LIEBERT INC 140 HUGUENOT STREET, 3RD FL, NEW ROCHELLE, NY 10801 USA.
3. Galarneau, M.R., et al., *Traumatic brain injury during Operation Iraqi Freedom: findings from the United States Navy–Marine Corps Combat Trauma Registry*. 2008.
4. Wojcik, B.E., et al., *Traumatic brain injury hospitalizations of US army soldiers deployed to Afghanistan and Iraq*. *American journal of preventive medicine*, 2010. **38**(1): p. S108-S116.
5. Okie, S., *Traumatic brain injury in the war zone*. *New England Journal of Medicine*, 2005. **352**(20): p. 2043-2047.
6. Kraus, M.F., et al., *White matter integrity and cognition in chronic traumatic brain injury: a diffusion tensor imaging study*. *Brain*, 2007. **130**(10): p. 2508-2519.
7. Rao, V. and C. Lyketsos, *Neuropsychiatric sequelae of traumatic brain injury*. *Psychosomatics*, 2000. **41**(2): p. 95-103.
8. Jaffee, M.S., J.W. Stokes, and F.O. Leal, *Posttraumatic stress disorder and posttraumatic stress disorder-like symptoms and mild traumatic brain injury*.

- Journal of rehabilitation research and development, 2007. **44**(7): p. 895.
9. Gould, K.R., et al., *Predictive and associated factors of psychiatric disorders after traumatic brain injury: a prospective study*. Journal of neurotrauma, 2011. **28**(7): p. 1155-1163.
 10. Leung, L.Y., et al., *Blast related neurotrauma: a review of cellular injury*. Mol Cell Biomech, 2008. **5**(3): p. 155-168.
 11. Warden, D., *Military TBI during the Iraq and Afghanistan wars*. Journal of Head Trauma Rehabilitation, 2006. **21**(5): p. 398-402.
 12. ROMBA, J.J. and P. MARTIN, *The propagation of air shock waves on a biophysical model*. 1961, DTIC Document.
 13. Courtney, A. and M. Courtney, *A thoracic mechanism of mild traumatic brain injury due to blast pressure waves*. Medical Hypotheses, 2009. **72**(1): p. 76-83.
 14. Kuehn, R., et al., *Rodent model of direct cranial blast injury*. Journal of neurotrauma, 2011. **28**(10): p. 2155-2169.
 15. Moss, W.C., M.J. King, and E.G. Blackman, *Skull Flexure from Blast Waves: A Mechanism for Brain Injury with Implications for Helmet Design*. Physical Review Letters, 2009. **103**(10).
 16. Bolander, R., et al., *Skull Flexure as a Contributing Factor in the Mechanism of Injury in the Rat when Exposed to a Shock Wave*. Annals of Biomedical Engineering, 2011. **39**(10): p. 2550-2559.
 17. Chafi, M.S., G. Karami, and M. Ziejewski, *Biomechanical Assessment of Brain Dynamic Responses Due to Blast Pressure Waves*. Annals of Biomedical Engineering, 2010. **38**(2): p. 490-504.

18. Taylor, P.A. and C.C. Ford, *Simulation of Blast-Induced Early-Time Intracranial Wave Physics leading to Traumatic Brain Injury*. Journal of Biomechanical Engineering-Transactions of the Asme, 2009. **131**(6).
19. Sharma, S. and L. Zhang. *Prediction of Intracranial Responses from Blast Induced Neurotrauma using a validated finite element model of human head*. in *Proceedings of Injury Biomechanics Symposium (IBS)*. 2011. Ohio State University Columbus (OH).
20. Ganpule, S., et al., *Mechanics of blast loading on the head models in the study of traumatic brain injury using experimental and computational approaches*. Biomech Model Mechanobiol, 2012. **In Press**.
21. Ellis, E., et al., *A new model for rapid stretch-induced injury of cells in culture: characterization of the model using astrocytes*. Journal of neurotrauma, 1995. **12**(3): p. 325-339.
22. Morrison III, B., D.F. Meaney, and T.K. McIntosh, *Mechanical characterization of an in vitro device designed to quantitatively injure living brain tissue*. Annals of biomedical engineering, 1998. **26**(3): p. 381-390.
23. Geddes, D.M. and R.S. Cargill, *An in vitro model of neural trauma: device characterization and calcium response to mechanical stretch*. Journal of biomechanical engineering, 2001. **123**(3): p. 247-255.
24. Lusardi, T.A., et al., *A device to study the initiation and propagation of calcium transients in cultured neurons after mechanical stretch*. Annals of biomedical engineering, 2004. **32**(11): p. 1546-1559.
25. Pfister, B.J., et al., *An in vitro uniaxial stretch model for axonal injury*. Annals of

- biomedical engineering, 2003. **31**(5): p. 589-598.
26. LaPlaca, M.C. and L.E. Thibault, *Anin vitro traumatic injury model to examine the response of neurons to a hydrodynamically-induced deformation*. Annals of biomedical engineering, 1997. **25**(4): p. 665-677.
 27. Edwards, M.E., S.S.S. Wang, and T.A. Good, *Role of Viscoelastic Properties of Differentiated SH-SY5Y Human Neuroblastoma Cells in Cyclic Shear Stress Injury*. Biotechnology progress, 2001. **17**(4): p. 760-767.
 28. Nakayama, Y., Y. Aoki, and H. Niitsu, *Studies on the mechanisms responsible for the formation of focal swellings on neuronal processes using a novel in vitro model of axonal injury*. Journal of neurotrauma, 2001. **18**(5): p. 545-554.
 29. Zhang, L., et al., *Reduction of voltage-dependent Mg²⁺ blockade of NMDA current in mechanically injured neurons*. Science, 1996. **274**(5294): p. 1921-1923.
 30. Tavalin, S.J., E.F. Ellis, and L.S. Satin, *Inhibition of the electrogenic Na pump underlies delayed depolarization of cortical neurons after mechanical injury or glutamate*. Journal of neurophysiology, 1997. **77**(2): p. 632-638.
 31. Geddes, D.M., M.C. LaPlaca, and R.S. Cargill, *Susceptibility of hippocampal neurons to mechanically induced injury*. Experimental neurology, 2003. **184**(1): p. 420-427.
 32. Lusardi, T.A., et al., *Effect of acute calcium influx after mechanical stretch injury in vitro on the viability of hippocampal neurons*. Journal of neurotrauma, 2004. **21**(1): p. 61-72.
 33. Chen, T., K.A. Willoughby, and E.F. Ellis, *Group I metabotropic receptor antagonism blocks depletion of calcium stores and reduces potentiated capacitative*

- calcium entry in strain-injured neurons and astrocytes*. Journal of neurotrauma, 2004. **21**(3): p. 271-281.
34. Arundine, M., et al., *Enhanced vulnerability to NMDA toxicity in sublethal traumatic neuronal injury in vitro*. Journal of neurotrauma, 2003. **20**(12): p. 1377-1395.
 35. Lea, P.M., et al., *Neuronal and glial mGluR5 modulation prevents stretch-induced enhancement of NMDA receptor current*. Pharmacology Biochemistry and Behavior, 2002. **73**(2): p. 287-298.
 36. Lea Iv, P.M., et al., *Modulation of stretch-induced enhancement of neuronal NMDA receptor current by mGluR1 depends upon presence of glia*. Journal of neurotrauma, 2003. **20**(11): p. 1233-1249.
 37. Myer, D.J., et al., *Essential protective roles of reactive astrocytes in traumatic brain injury*. Brain, 2006. **129**(Pt 10): p. 2761-72.
 38. Charles, A.C., et al., *Intercellular signaling in glial cells: calcium waves and oscillations in response to mechanical stimulation and glutamate*. Neuron, 1991. **6**(6): p. 983-992.
 39. Gentleman, R.C., et al., *Bioconductor: open software development for computational biology and bioinformatics*. Genome Biology, 2004. **5**(10).
 40. Rzigalinski, B.A., et al., *Effect of Ca²⁺ on in vitro astrocyte injury*. Journal of neurochemistry, 1997. **68**(1): p. 289-296.
 41. Rzigalinski, B., et al., *Intracellular Free Calcium Dynamics in Stretch-Injured Astrocytes*. Journal of neurochemistry, 1998. **70**(6): p. 2377-2385.
 42. Lamb, R.G., et al., *Alterations in Phosphatidylcholine Metabolism of Stretch-*

- Injured Cultured Rat Astrocytes*. Journal of neurochemistry, 1997. **68**(5): p. 1904-1910.
43. Ahmed, S.M., et al., *Stretch-induced injury alters mitochondrial membrane potential and cellular ATP in cultured astrocytes and neurons*. Journal of neurochemistry, 2000. **74**(5): p. 1951-1960.
 44. Hoffman, S., et al., *Astrocytes generate isoprostanes in response to trauma or oxygen radicals*. Journal of neurotrauma, 2000. **17**(5): p. 415-420.
 45. Floyd, C.L., et al., *Traumatic injury of cultured astrocytes alters inositol (1, 4, 5)-trisphosphate-mediated signaling*. Glia, 2001. **33**(1): p. 12-23.
 46. Ellis, E.F., et al., *S100B protein is released from rat neonatal neurons, astrocytes, and microglia by in vitro trauma and anti-S100 increases trauma-induced delayed neuronal injury and negates the protective effect of exogenous S100B on neurons*. Journal of neurochemistry, 2007. **101**(6): p. 1463-1470.
 47. Ender, M.G., *Invisible Wounds of War: Psychological and Cognitive Injuries, Their Consequences, and Services to Assist Recovery*. Contemporary Sociology-a Journal of Reviews, 2010. **39**(4): p. 399-402.
 48. Marshall, K.R., et al., *Mild traumatic brain injury screening, diagnosis, and treatment*. Military Medicine, 2012. **177**(8 Suppl): p. 67-75.
 49. Long, J.B., et al., *Blast Overpressure in Rats: Recreating a Battlefield Injury in the Laboratory*. Journal of Neurotrauma, 2009. **26**(6): p. 827-840.
 50. Cheng, J.M., et al., *Development of a rat model for studying blast-induced traumatic brain injury*. Journal of the Neurological Sciences, 2010. **294**(1-2): p. 23-28.

51. Risling, M., et al., *Mechanisms of blast induced brain injuries, experimental studies in rats*. Neuroimage, 2011. **54**: p. S89-S97.
52. Saljo, A., et al., *Mechanisms and pathophysiology of the low-level blast brain injury in animal models*. Neuroimage, 2011. **54**: p. S83-S88.
53. Sundaramurthy, A., et al., *Blast-induced biomechanical loading of the rat: an experimental and anatomically accurate computational blast injury model*. Journal of Neurotrauma, 2012. **29**(13): p. 2352-2364.
54. Alley, M.D., B.R. Schimizzze, and S.F. Son, *Experimental modeling of explosive blast-related traumatic brain injuries*. Neuroimage, 2011. **54**: p. S45-S54.
55. Ganpule, S., et al., *Mechanics of blast loading on the head models in the study of traumatic brain injury using experimental and computational approaches*. Biomechanics and Modeling in Mechanobiology, 2012: p. 1-21.
56. Zhu, F., et al., *Using a gel/plastic surrogate to study the biomechanical response of the head under air shock loading: a combined experimental and numerical investigation*. Biomechanics and Modeling in Mechanobiology, 2012. **11**(3): p. 341-353.
57. Kleinschmit, N.N., *A shock tube technique for blast wave simulation and studies of flow structure interactions in shock tube blast experiments*. 2011, University of Nebraska-Lincoln.
58. Liu, M.B., G.R. Liu, and K.Y. Lam, *Investigations into water mitigation using a meshless particle method*. Shock Waves, 2002. **12**(3): p. 181-195.
59. Ganpule, S., et al., *Role of helmet in the mechanics of shock wave propagation under blast loading conditions*. Computer Methods in Biomechanics and

- Biomedical Engineering, 2012. **15**(11): p. 1233-1244.
60. Chen, Y. and M. Ostoj-Starzewski, *MRI-based finite element modeling of head trauma: spherically focusing shear waves*. Acta Mechanica, 2010. **213**(1-2): p. 155-167.
 61. Bauman, R.A., et al., *An introductory characterization of a combat-casualty-care relevant swine model of closed head injury resulting from exposure to explosive blast*. Journal of Neurotrauma, 2009. **26**(6): p. 841-860.
 62. Chavko, M., et al., *Measurement of blast wave by a miniature fiber optic pressure transducer in the rat brain*. Journal of Neuroscience Methods, 2007. **159**(2): p. 277-281.
 63. Chavko, M., et al., *Relationship between orientation to a blast and pressure wave propagation inside the rat brain*. Journal of Neuroscience Methods, 2011. **195**(1): p. 61-66.
 64. Nyein, M.K., et al., *In silico investigation of intracranial blast mitigation with relevance to military traumatic brain injury*. Proceedings of the National Academy of Sciences, 2010. **107**(48): p. 20703-20708.
 65. Bhattacharjee, Y., *Neuroscience - Shell shock revisited: Solving the puzzle of blast trauma*. Science, 2008. **319**(5862): p. 406-408.
 66. Courtney, A.C. and M.W. Courtney, *A thoracic mechanism of mild traumatic brain injury due to blast pressure waves*. Medical Hypotheses, 2009. **72**(1): p. 76-83.
 67. Finkel, M.F., *The neurological consequences of explosives*. Journal of the Neurological Sciences, 2006. **249**(1): p. 63-67.
 68. Krave, U., S. Hojer, and H.A. Hansson, *Transient, powerful pressures are generated*

- in the brain by a rotational acceleration impulse to the head.* European Journal of Neuroscience, 2005. **21**(10): p. 2876-2882.
69. Zhang, L., K.H. Yang, and A.I. King, *A proposed injury threshold for mild traumatic brain injury.* TRANSACTIONS-AMERICAN SOCIETY OF MECHANICAL ENGINEERS JOURNAL OF BIOMECHANICAL ENGINEERING, 2004. **126**(2): p. 226-236.
 70. Nakagawa, A., et al., *Shock wave-induced brain injury in rat: novel traumatic brain injury animal model.* Acta Neurochirurgica Supplements, 2009: p. 421-424.
 71. Goeller, J., et al., *Investigation of Cavitation as a Possible Damage Mechanism in Blast-Induced Traumatic Brain Injury.* Journal of Neurotrauma, 2012. **29**(10): p. 1970-1981.
 72. Anderson, J.D., *Fundamentals of Aerodynamics.* 2001, New York: McGraw-Hill.
 73. Lubock, P. and W. Goldsmith, *Experimental cavitation studies in a model head-neck system.* Journal of Biomechanics, 1980. **13**(12): p. 1041-1052.
 74. Marklund, N., et al., *alpha-Phenyl-tert-N-butyl nitron (PBN) improves functional and morphological outcome after cortical contusion injury in the rat.* Acta Neurochirurgica, 2001. **143**(1): p. 73-81.
 75. Nakagawa, A., et al., *Shock wave-induced brain injury in rat: Novel traumatic brain injury animal model.* Acta Neurochirurgica Supplement, 2009. **102**: p. 421-424.
 76. Mao, H.J., et al., *Development of a Finite Element Human Head Model Partially Validated With Thirty Five Experimental Cases.* Journal of Biomechanical Engineering-Transactions of the Asme, 2013. **135**(11).

77. Willinger, R., H.-S. Kang, and B. Diaw, *Three-dimensional human head finite-element model validation against two experimental impacts*. Annals of Biomedical Engineering, 1999. **27**(3): p. 403-410.
78. DePalma, R., et al., *Blast related traumatic brain injury: pathophysiology, comorbidities, and neurobehavioral outcomes*. Understanding Traumatic Brain Injury: Current Research and Future Directions, 2014: p. 413.
79. Fischer, H., *United States Military Casualty Statistics: Operation Iraqi Freedom and Operation Enduring Freedom*. 2007, Library of Congress: Washington, DC.
80. Zhu, F., et al., *Using a gel/plastic surrogate to study the biomechanical response of the head under air shock loading: a combined experimental and numerical investigation*. Biomechanics and modeling in mechanobiology, 2012. **11**(3-4): p. 341-353.
81. Margulies, S.S., L.E. Thibault, and T.A. Gennarelli, *Physical model simulations of brain injury in the primate*. Journal of biomechanics, 1990. **23**(8): p. 823-836.
82. Taylor, P.A. and C.C. Ford, *Simulation of blast-induced early-time intracranial wave physics leading to traumatic brain injury*. Journal of biomechanical engineering, 2009. **131**(6): p. 061007.
83. Panzer, M.B., et al., *Development of a finite element model for blast brain injury and the effects of CSF cavitation*. Annals of biomedical engineering, 2012. **40**(7): p. 1530-1544.
84. Wang, C., et al., *Computational study of human head response to primary blast waves of five levels from three directions*. PLoS one, 2014. **9**(11): p. e113264.
85. Monson, K.L., et al., *Axial mechanical properties of fresh human cerebral blood*

- vessels. *Journal of biomechanical engineering*, 2003. **125**(2): p. 288-294.
86. Zhang, L., J. Bae, and W.N. Hardy, *Computational study of the contribution of the vasculature on the dynamic response of the brain*. *Stapp Car Crash Journal*, 2002. **46**: p. 145-163.
 87. Ho, J. and S. Kleiven, *Dynamic response of the brain with vasculature: A three-dimensional computational study*. *Journal of Biomechanics*, 2007. **40**(13): p. 3006-3012.
 88. Parnaik, Y., et al., *The influence of surrogate blood vessels on the impact response of a physical model of the brain*. *Stapp Car Crash Journal*, 2004. **48**: p. 259-277.
 89. Hua, Y., et al., *Experimental and numerical investigation of the mechanism of blast wave transmission through a surrogate head*. *Journal of Computational and Nonlinear Dynamics*, 2014. **9**(3): p. 031010.
 90. Zhang, L., K.H. Yang, and A.I. King, *Comparison of brain responses between frontal and lateral impacts by finite element modeling*. *Journal of neurotrauma*, 2001. **18**(1): p. 21-30.
 91. Zhao, S., L. Gu, and S.R. Froemming, *Experimental investigation of the stent–artery interaction*. *Journal of medical engineering & technology*, 2013. **37**(7): p. 463-469.
 92. Liu, M., G. Liu, and K. Lam, *Investigations into water mitigation using a meshless particle method*. *Shock waves*, 2002. **12**(3): p. 181-195.
 93. Khalil, T.B. and R.P. Hubbard, *Parametric study of head response by finite element modeling*. *Journal of Biomechanics*, 1977. **10**(2): p. 119-132.
 94. McElhaney, J.H., et al., *Mechanical properties of cranial bone*. *Journal of*

- biomechanics, 1970. **3**(5): p. 495-511.
95. Yeoh, S., E.D. Bell, and K.L. Monson, *Distribution of blood–brain barrier disruption in primary blast injury*. Annals of biomedical engineering, 2013. **41**(10): p. 2206-2214.
 96. Hue, C.D., et al., *Blood-brain barrier dysfunction after primary blast injury in vitro*. Journal of neurotrauma, 2013. **30**(19): p. 1652-1663.
 97. Capó-Aponte, J.E., et al., *Visual dysfunctions and symptoms during the subacute stage of blast-induced mild traumatic brain injury*. Military medicine, 2012. **177**(7): p. 804-813.
 98. Dougherty, A.L., et al., *Visual dysfunction following blast-related traumatic brain injury from the battlefield*. Brain injury, 2011. **25**(1): p. 8-13.
 99. Johan, I., C.V. David, and L. Per, *Influence of the anterior and middle cranial fossae on brain kinematics during sagittal plane head rotation*. Journal of Crash Prevention and Injury Control, 2001. **2**(4): p. 271-287.
 100. Brands, D.W., et al. *Comparison of the dynamic behavior of brain tissue and two model materials*. in *Stapp Car Crash Conference proceedings*. 1999.
 101. Ryu, J., et al., *The problem of axonal injury in the brains of veterans with histories of blast exposure*. Acta neuropathologica communications, 2014. **2**(1): p. 153-153.
 102. Monson, K.L., *Mechanical and failure properties of human cerebral blood vessels*, in *PhD thesis, University of California, Berkeley*. 2001.
 103. Bain, A.C. and D.F. Meaney, *Tissue-level thresholds for axonal damage in an experimental model of central nervous system white matter injury*. Journal of biomechanical engineering, 2000. **122**(6): p. 615-622.

104. Shreiber, D.I., A.C. Bain, and D.F. Meaney, *In vivo thresholds for mechanical injury to the blood-brain barrier*. 1997, SAE Technical Paper.
105. Chafi, M.S., et al., *Dynamic response of brain subjected to blast loadings: influence of frequency ranges*. International Journal of Applied Mechanics, 2011. **3**(04): p. 803-823.
106. Davenport, N.D., et al., *Diffuse and spatially variable white matter disruptions are associated with blast-related mild traumatic brain injury*. Neuroimage, 2012. **59**(3): p. 2017-2024.
107. Kleinschmit, N.N., *A shock tube technique for blast wave simulation and studies for flow structure interactions in shock tube blast experiments*. Master's thesis. 2011, University of Nebraska-Lincoln.
108. Hodgson, V.R., L.M. Thomas, and T.B. Khalil, *The role of impact location in reversible cerebral concussion*. 1983, SAE Technical Paper.
109. Gennarelli, T.A., et al., *Directional dependence of axonal brain injury due to centroidal and non-centroidal acceleration*. 1987, SAE Technical Paper.
110. Zhang, L., R. Makwana, and S. Sharma, *Brain response to primary blast wave using validated finite element models of human head and advanced combat helmet*. Frontiers in neurology, 2013. **4**.
111. Leonardi, A.D.C., et al., *Head orientation affects the intracranial pressure response resulting from shock wave loading in the rat*. Journal of biomechanics, 2012. **45**(15): p. 2595-2602.
112. Aravind, S., et al., *Blast-induced biomechanical loading of the rat: an experimental and anatomically accurate computational blast injury model*. Journal of

- Neurotrauma, 2012. **29**(13): p. 2352-2364.
113. Chafi, M.S., et al., *A finite element method parametric study of the dynamic response of the human brain with different cerebrospinal fluid constitutive properties*. Proceedings of the Institution of Mechanical Engineers Part H-Journal of Engineering in Medicine, 2009. **223**(H8): p. 1003-1019.
 114. Hua, Y., P.K. Akula, and L. Gu, *Experimental and numerical investigation of carbon fiber sandwich panels subjected to blast loading*. Composites Part B: Engineering, 2014. **56**: p. 456-463.
 115. Ruan, J., T. Khalil, and A. King, *Dynamic response of the human head to impact by three-dimensional finite element analysis*. Journal of Biomechanical Engineering, 1994. **116**(1): p. 44-50.
 116. Morrison 3rd, B., et al., *A tissue level tolerance criterion for living brain developed with an in vitro model of traumatic mechanical loading*. Stapp Car Crash Journal, 2003. **47**: p. 93.
 117. Mao, H., et al., *Strain-based regional traumatic brain injury intensity in controlled cortical impact: a systematic numerical analysis*. Journal of Neurotrauma, 2011. **28**(11): p. 2263-2276.
 118. Bayly, P.V., et al., *In vivo imaging of rapid deformation and strain in an animal model of traumatic brain injury*. Journal of biomechanics, 2006. **39**(6): p. 1086-1095.
 119. Kuijpers, A., M. Claessens, and A. Sauren, *The influence of different boundary conditions on the response of the head to impact: a two-dimensional finite element study*. Journal of Neurotrauma, 1995. **12**(4): p. 715-724.

120. Bruns, J. and W.A. Hauser, *The epidemiology of traumatic brain injury: a review*. *Epilepsia*, 2003. **44**(s10): p. 2-10.
121. Control, C.f.D. and Prevention, *Report to congress on traumatic brain injury in the United States: Epidemiology and rehabilitation*. National Center for Injury Prevention and Control, 2015.
122. De Silva, M.J., et al., *Patient outcome after traumatic brain injury in high-, middle- and low-income countries: analysis of data on 8927 patients in 46 countries*. *International journal of epidemiology*, 2009. **38**(2): p. 452-458.
123. Meaney, D.F., B. Morrison, and C.D. Bass, *The mechanics of traumatic brain injury: a review of what we know and what we need to know for reducing its societal burden*. *Journal of biomechanical engineering*, 2014. **136**(2): p. 021008.
124. Fleminger, S. and J. Ponsford, *Long term outcome after traumatic brain injury: More attention needs to be paid to neuropsychiatric functioning*. *BMJ: British Medical Journal*, 2005. **331**(7530): p. 1419.
125. Morales, D., et al., *Experimental models of traumatic brain injury: do we really need to build a better mousetrap?* *Neuroscience*, 2005. **136**(4): p. 971-989.
126. Briones, T.L., *Animal Models of Traumatic Brain Injury: Is There an Optimal Model That Parallels Human Brain Injury?* *Annual review of nursing research*, 2015. **33**(1): p. 31-73.
127. Morrison III, B., et al., *In vitro models of traumatic brain injury*. *Annual review of biomedical engineering*, 2011. **13**: p. 91-126.
128. Chen, S., J. Pickard, and N. Harris, *Time course of cellular pathology after controlled cortical impact injury*. *Experimental neurology*, 2003. **182**(1): p. 87-102.

129. Floyd, C.L. and B.G. Lyeth, *Astroglia: important mediators of traumatic brain injury*. Progress in Brain Research, 2007. **161**: p. 61-79.
130. Sofroniew, M.V. and H.V. Vinters, *Astrocytes: biology and pathology*. Acta neuropathologica, 2010. **119**(1): p. 7-35.
131. Zhao, X., et al., *Early loss of astrocytes after experimental traumatic brain injury*. Glia, 2003. **44**(2): p. 140-152.
132. Burda, J.E., A.M. Bernstein, and M.V. Sofroniew, *Astrocyte roles in traumatic brain injury*. Experimental neurology, 2016. **275**: p. 305-315.
133. Beaudoin III, G.M., et al., *Culturing pyramidal neurons from the early postnatal mouse hippocampus and cortex*. Nature protocols, 2012. **7**(9): p. 1741-1754.
134. Wilson, C.L., et al., *Mitochondrial dysfunction and loss of glutamate uptake in primary astrocytes exposed to titanium dioxide nanoparticles*. Nanoscale, 2015. **7**(44): p. 18477-18488.
135. Smith, D.H., et al., *High tolerance and delayed elastic response of cultured axons to dynamic stretch injury*. The Journal of neuroscience, 1999. **19**(11): p. 4263-4269.
136. Skotak, M., F. Wang, and N. Chandra, *An in vitro injury model for SH-SY5Y neuroblastoma cells: effect of strain and strain rate*. Journal of neuroscience methods, 2012. **205**(1): p. 159-168.
137. <http://www.azom.com/properties.aspx?ArticleID=920>.
138. Chen, Y., et al., *A modified controlled cortical impact technique to model mild traumatic brain injury mechanics in mice*. Frontiers in neurology, 2014. **5**.
139. Morrison III, B., et al., *A tissue level tolerance criterion for living brain developed with an in vitro model of traumatic mechanical loading*. Stapp Car Crash Journal,

2003. **47**: p. 93.
140. Winston, F., et al., *A system to reproduce and quantify the biomechanical environment of the cell*. Journal of Applied Physiology, 1989. **67**(1): p. 397-405.
 141. Geddes-Klein, D.M., K.B. Schiffman, and D.F. Meaney, *Mechanisms and consequences of neuronal stretch injury in vitro differ with the model of trauma*. Journal of neurotrauma, 2006. **23**(2): p. 193-204.
 142. Millet, L.J. and M.U. Gillette, *Over a century of neuron culture: from the hanging drop to microfluidic devices*. Yale J Biol Med, 2012. **85**(4): p. 501-21.
 143. Georges, P.C., et al., *Matrices with compliance comparable to that of brain tissue select neuronal over glial growth in mixed cortical cultures*. Biophysical journal, 2006. **90**(8): p. 3012-3018.
 144. de Witt, B.W., et al., *Abbreviated environmental enrichment enhances neurobehavioral recovery comparably to continuous exposure after traumatic brain injury*. Neurorehabilitation and neural repair, 2011. **25**(4): p. 343-350.
 145. Peskind, E.R., et al., *Military-and sports-related mild traumatic brain injury: clinical presentation, management, and long-term consequences*. J Clin Psychiatry, 2013. **74**: p. 180-188.
 146. Laurer, H.L., et al., *Mild head injury increasing the brain's vulnerability to a second concussive impact*. Journal of Neurosurgery, 2001. **95**(5): p. 859-870.
 147. Shitaka, Y., et al., *Repetitive closed-skull traumatic brain injury in mice causes persistent multifocal axonal injury and microglial reactivity*. Journal of neuropathology and experimental neurology, 2011. **70**(7): p. 551.
 148. Laskowitz, D.T., et al., *COG1410, a novel apolipoprotein E-based peptide,*

- improves functional recovery in a murine model of traumatic brain injury.* Journal of Neurotrauma, 2007. **24**(7): p. 1093-1107.
149. Maruichi, K., et al., *Graded model of diffuse axonal injury for studying head injury-induced cognitive dysfunction in rats.* Neuropathology, 2009. **29**(2): p. 132-139.
 150. Cernak, I., et al., *The pathobiology of moderate diffuse traumatic brain injury as identified using a new experimental model of injury in rats.* Neurobiology of Disease, 2004. **17**(1): p. 29-43.
 151. Ren, Z., et al., *'Hit & Run' model of closed-skull traumatic brain injury (TBI) reveals complex patterns of post-traumatic AQP4 dysregulation.* Journal of Cerebral Blood Flow & Metabolism, 2013. **33**(6): p. 834-845.
 152. Longhi, L., et al., *Temporal window of vulnerability to repetitive experimental concussive brain injury.* Neurosurgery, 2005. **56**(2): p. 364-373.
 153. Gurkoff, G.G., et al., *Evaluation of metric, topological, and temporal ordering memory tasks after lateral fluid percussion injury.* Journal of neurotrauma, 2013. **30**(4): p. 292-300.
 154. Atkins, C.M., et al., *Effects of early rolipram treatment on histopathological outcome after controlled cortical impact injury in mice.* Neuroscience letters, 2013. **532**: p. 1-6.
 155. Levchakov, A., et al., *Computational studies of strain exposures in neonate and mature rat brains during closed head impact.* Journal of Neurotrauma, 2006. **23**(10): p. 1570-1580.
 156. Mao, H.J., et al., *Finite Element Analysis of Controlled Cortical Impact-Induced Cell Loss.* Journal of Neurotrauma, 2010. **27**(5): p. 877-888.

157. Gefen, A., et al., *Age-dependent changes in material properties of the brain and braincase of the rat*. Journal of Neurotrauma, 2003. **20**(11): p. 1163-1177.
158. Finan, J.D., et al., *Viscoelastic Properties of the Rat Brain in the Sagittal Plane: Effects of Anatomical Structure and Age (vol 40, pg 70, 2012)*. Annals of Biomedical Engineering, 2012. **40**(4): p. 982-985.
159. Mao, H.J., et al., *Material Properties of Adult Rat Skull*. Journal of Mechanics in Medicine and Biology, 2011. **11**(5): p. 1199-1212.
160. Elliott, M.B., J.J. Jallo, and R.F. Tuma, *An investigation of cerebral edema and injury volume assessments for controlled cortical impact injury*. Journal of Neuroscience Methods, 2008. **168**(2): p. 320-324.
161. Mao, H.J., et al., *Computational neurotrauma-design, simulation, and analysis of controlled cortical impact model*. Biomechanics and Modeling in Mechanobiology, 2010. **9**(6): p. 763-772.
162. Brody, D.L., et al., *Electromagnetic controlled cortical impact device for precise, graded experimental traumatic brain injury*. Journal of Neurotrauma, 2007. **24**(4): p. 657-673.
163. Nimmerjahn, A., F. Kirchhoff, and F. Helmchen, *Resting microglial cells are highly dynamic surveillants of brain parenchyma in vivo*. Science, 2005. **308**(5726): p. 1314-1318.
164. Kelso, M.L. and H.E. Gendelman, *Bridge between neuroimmunity and traumatic brain injury*. Current pharmaceutical design, 2014. **20**(26): p. 4284.